

HIGH PRESSURE VIBRATIONAL AND EXAFS SPECTROSCOPY

A thesis presented for the degree of
Doctor of Philosophy
in the
Faculty of Science

by
PATRICK ALAN FLETCHER

University of Leicester
1987

UMI Number: U008122

All rights reserved

INFORMATION TO ALL USERS

The quality of this reproduction is dependent upon the quality of the copy submitted.

In the unlikely event that the author did not send a complete manuscript and there are missing pages, these will be noted. Also, if material had to be removed, a note will indicate the deletion.



UMI U008122

Published by ProQuest LLC 2015. Copyright in the Dissertation held by the Author.
Microform Edition © ProQuest LLC.

All rights reserved. This work is protected against
unauthorized copying under Title 17, United States Code.



ProQuest LLC
789 East Eisenhower Parkway
P.O. Box 1346
Ann Arbor, MI 48106-1346

Statement:

The work presented in this thesis is original unless acknowledged in the text or by reference, and was carried out by the author in the Department of Chemistry of the University of Leicester between October 1982 and April 1986. This work has not been, nor will be, presented for any other degree.

P. A. Fletcher

P. A. Fletcher

ACKNOWLEDGEMENTS

I should like to thank the following people, without whose assistance this work would not have been possible:

My supervisor, David Adams, for the benefit of his experience and encouragement throughout.

The Technical Staff of the Department of Chemistry, in particular Phil Acton who kept the laboratory on its feet through thick and thin, and Ann Crane for tracing or drawing most of the figures and diagrams.

I acknowledge the receipt of a maintenance grant from the Science and Engineering Research Council.

CONTENTS

	Page	
CHAPTER 1	An Introduction to Physical Investigations at High Pressures	1
CHAPTER 2	Extended X-Ray Absorption Spectroscopy - An Introduction to the Theory, Experimental Procedure and Data Analysis	12
CHAPTER 3	Preliminary EXAFS Investigations of High Pressure Phase Transitions	22
CHAPTER 4	A Raman Scattering Study of the Phase Behaviour of the Mercury (II) Halides HgX_2 , X = Cl, Br	31
CHAPTER 5	A Raman and Infrared Vibrational Study of some Pyroxene Variants I. The Alkali Metavanadates MVO_3 , M = K, Rb, Cs II. Copper Metagermanate, CuGeO_3	45
CHAPTER 6	A Study of the Phase Behaviour of $\text{K}[\text{M}(\text{CN})_2]$, M = Ag, Au, at High Pressures Investigated by Raman Scattering	59

CHAPTER 1

AN INTRODUCTION TO PHYSICAL INVESTIGATIONS AT HIGH PRESSURES

"There is no profit from the point of view of physics in trying for 'records' in the attainment of high pressures and little physical interest, unless it is possible to do something with the pressure in the way of finding the properties of matter under new conditions."

P. W. Bridgman, 1941

CHAPTER 1

AN INTRODUCTION TO PHYSICAL INVESTIGATIONS AT HIGH PRESSURES

1.1 Introduction

The study of solid state phenomena at high external pressures is, today, a most popular and extensive area of research. Apparatus has been developed for high pressure work with a wide variety of spectroscopic techniques, including the study of electronic, magnetic and other properties.

A common response of a system subjected to increasing pressure is a structural transformation or phase transition to a denser, usually less symmetric, form. It is the rationalisation of the factors influencing such a change that is the ultimate goal of the high pressure investigator. In this thesis, vibrational spectroscopy and the fast developing technique of x-ray absorption spectroscopy have been used to such a purpose.

1.2 The Diamond Anvil Cell

In the forty year period from 1910 to 1950 the field of solid state high pressure research was pioneered by the work of P. W. Bridgman, using the so-called Bridgman anvil and piston-cylinder devices.¹ It was not until the late 1950's that the diamond anvil cell (d.a.c.), in the form it is known today, was first introduced in performing high pressure x-ray and infrared absorption measurements.^{2,3} Over the subsequent twenty five year period the d.a.c. has undergone various design modifications, but all have retained the essential feature of compressing a sample between the parallel faces of two opposed diamond anvils.⁴⁻⁸

1.3 Cell Design and Use

The high pressure cells used for all work presented here are essentially of a modified Van Valkenburg design, and their development within this laboratory has been detailed previously.⁹ The Mark III cell in current use is produced in two models, the Diacell and Dynocell, the former being rated for a maximum working pressure of up to 150 kbar, the latter up to 1.0 Mbar,¹⁰ Figs. 1:1 - 1:4.

When the cell is assembled force is generated either hydraulically or by compressing Belleville spring washers by a simple screw mechanism, and is transmitted to the moving anvil holder via the lever arms and presser plate. The light ports beneath each anvil permit the passage of radiation through the diamonds and the sample, as shown in the simple ray diagram, Fig. 1:5. Diamond is remarkable in that it is highly transparent to many regions of electromagnetic radiation, however, some care must be taken in selecting the correct type of gem quality stone for the task at hand.¹¹ This is particularly relevant in infrared and light scattering studies, so in these cases those diamonds with fewest i.r. absorptions and lowest fluorescence profiles are to be preferred.

1.4 Gaskets and Pressure Media

In compressing a sample between the two working diamond faces the material experiences an approximately parabolic pressure gradient, from a maximum at the centre to near ambient at the edges. With the introduction of a gasket and pressure transmitting fluid,¹² however, it is possible to hold the sample in a hydrostatic environment, and thus make quantitative measurements without the presence of multiphase systems, other than those existing in equilibrium at a single pressure. The gasket is a piece of thin sheet metal through which a hole is either drilled or spark eroded, and for vibrational spectroscopy is typically of the following dimensions:

	Raman	Infrared
Thickness (mm)	0.2/0.15	0.075
Hole diameter (mm)	0.4/0.3	0.9 to 0.6

Figure 1:1

The Dynocell: side elevation and section of the central insert.

Parts labelled are:

1. Cell body
2. Central insert
3. Fixed anvil holder
4. Moving anvil holder
5. Presser plate
6. Lever arms
7. Piston plate
8. Hydraulic ram
9. Knurled backing screw
10. Central pivot
11. Piston screw
12. V block assembly

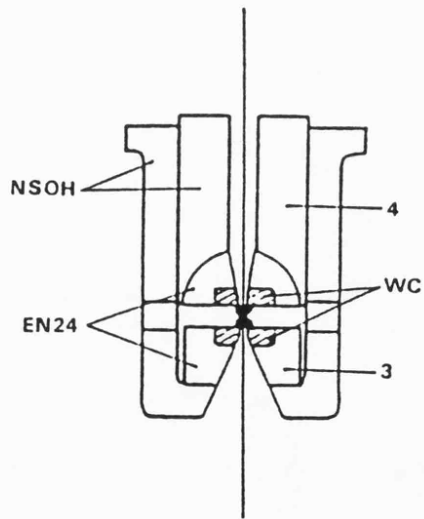
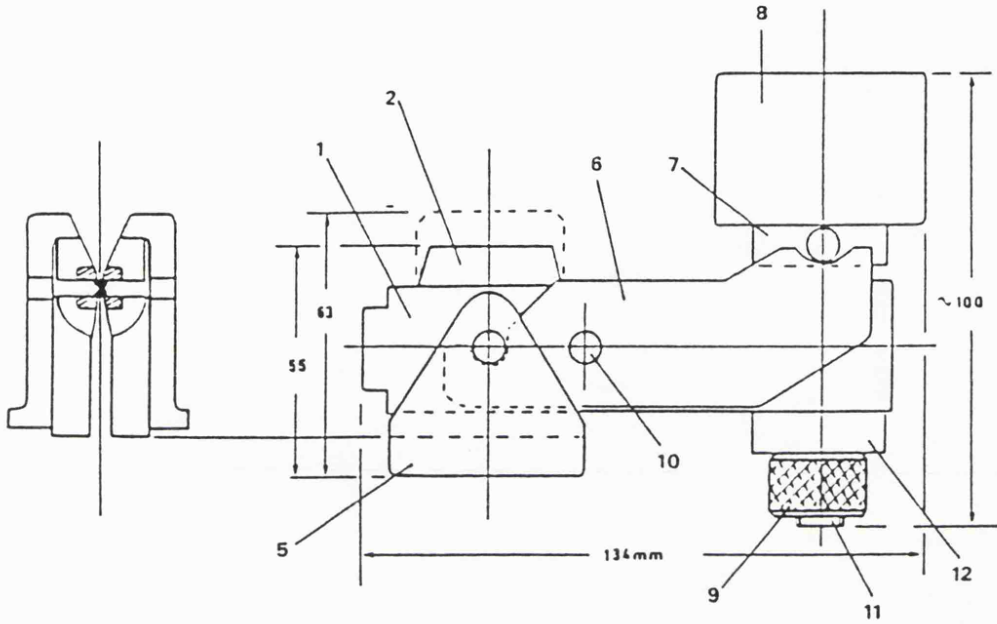


Figure 1:2

The Diacell: plan and side elevation.

Parts labelled are:

1. Cell body
2. Central insert
3. Fixed anvil holder
4. Moving anvil holder
5. Presser plate
6. Lever arms
7. Internal hydraulic ram
8. Knurled backing screw
9. Piston plate
10. Central pivot
11. Piston screw
12. Oil feed for hydraulic ram

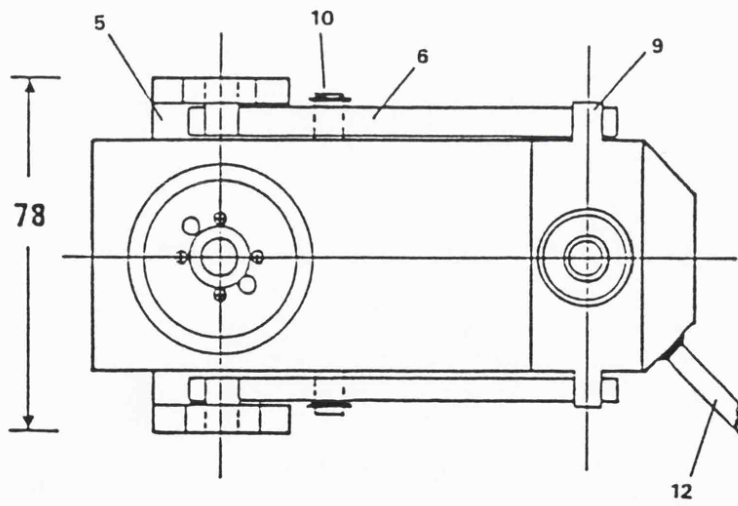
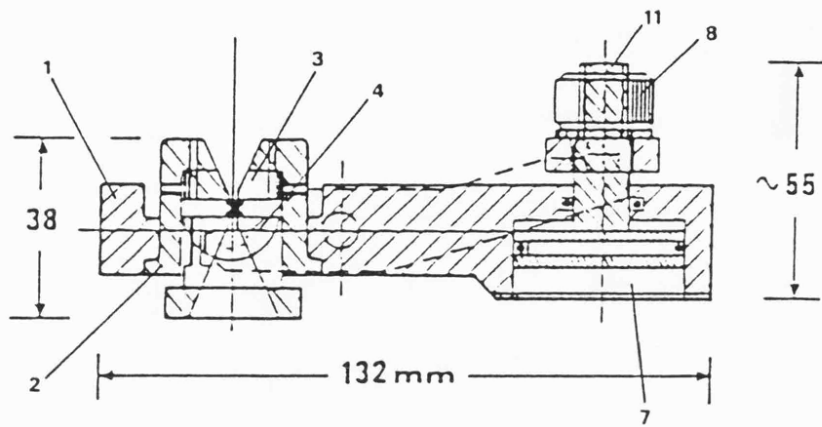


Figure 1:3

Assembled Mark III Diacell.

Figure 1:4

Assembled Mark III Dynocell.

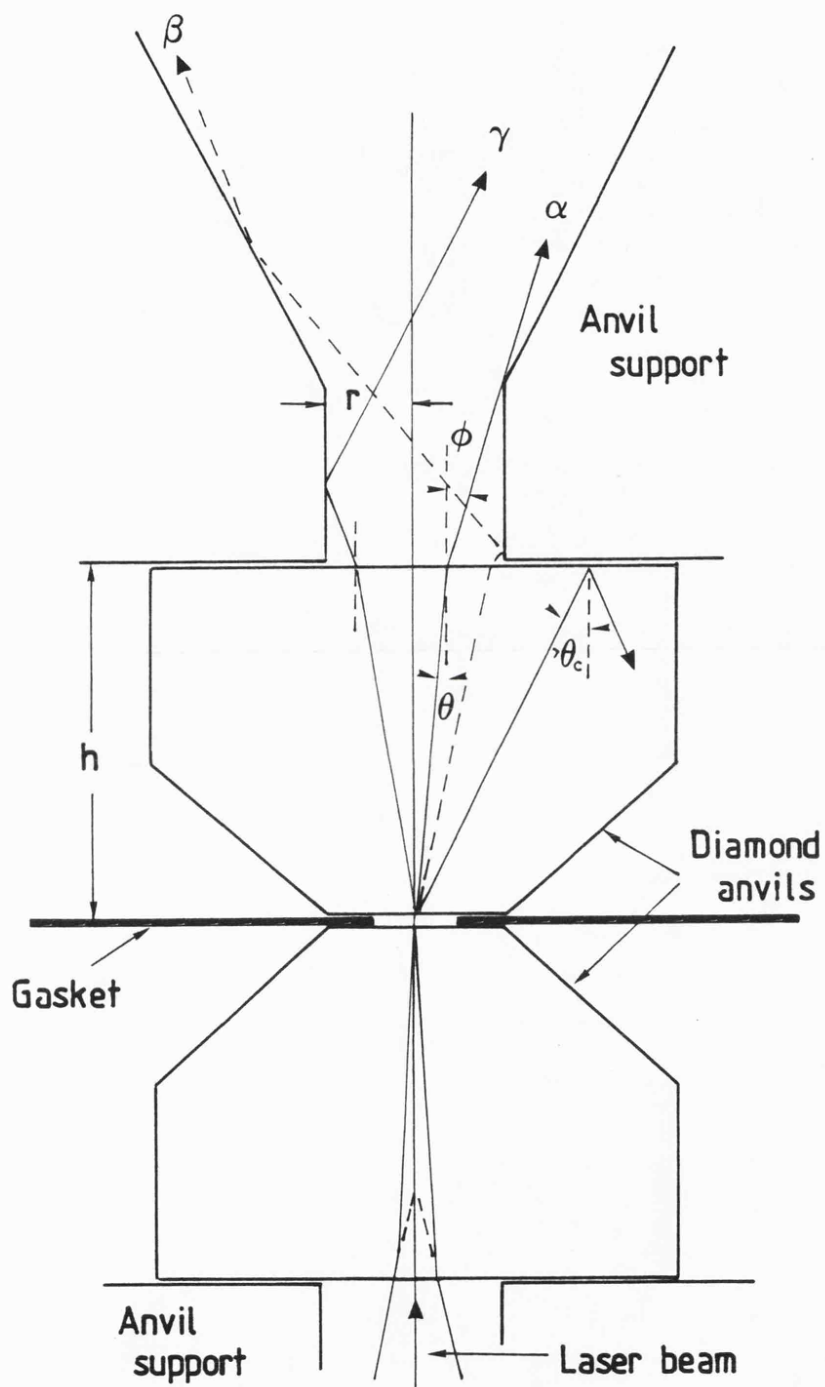


Figure 1:5

Ray paths in a diamond anvil cell used for Raman or infrared spectroscopy.

Only those rays that strike the diamond-air interface at less than the critical angle θ_C will emerge from the cell.

The numerical aperture of the transmitted beam is given by $NA_t = \eta_D \sin\theta_D$, where $\theta_D = \tan^{-1}(r/h)$. For this d.a.c. design $h = 2$ mm and $r = 0.45$ mm, corresponding to $\theta_D = 12.7^\circ$, $\phi = 32.1^\circ$, and $NA_t = 0.53$. Only rays with $\theta < 5.8^\circ$ will pass directly out of the cell (*e.g.* ray α) but others (*e.g.* rays β , γ) with $5.8 < \theta < 12.7^\circ$ will be collected after reflection from the walls of the support material.



Inconel (a Ni/Cr/Fe alloy) is the most commonly employed gasket material; stainless steel and molybdenum also being used. The latter was found to be particularly useful in the study of the mercuric halides (Chapter 4), since these compounds readily attack the other types.

Methanol plus ethanol in 4:1 ratio has become the most widely used fluid pressure medium since the discovery that the mixture is hydrostatic to above 100 kbar.¹³ More recently, cryogenically loaded liquefied "gases" such as hydrogen and helium have extended this limit of hydrostatic behaviour to in excess of 600 kbar.^{14,15} In infrared studies the sample is diluted in a ratio of *ca.* 1:9 within a suitable infrared transparent material, such as potassium bromide. In a good loading this matrix can provide a hydrostatic environment to beyond 50 kbar, Fig. 1:6.

1.5 Pressure Calibration

In the analysis of materials held at high static pressures within a d.a.c., it is essential to be able to routinely determine pressure both quickly and accurately. For many types of experiment, and particularly for vibrational work, the ruby fluorescence technique has proven the most versatile in this respect.¹⁶ It is based on monitoring the frequency shift with pressure of the R_1 and R_2 fluorescence lines of ruby, which result from the incorporation of trace amounts of Cr^{3+} into the Al_2O_3 lattice. The shift ($0.76 \text{ cm}^{-1} \text{ kbar}^{-1}$ for R_1) is nearly linear to pressures above 1 Mbar and may be measured to a precision equivalent to 0.5 kbar or better.¹⁷⁻²⁰ The scale has recently been used to quote a figure of some 4.6 Mbar; the highest pressure yet achieved in a diamond anvil device.²¹ The fluorescence is usually laser excited from a small chip of ruby incorporated with the sample when loading, and is recorded on a sensitive spectrometer such as that used for Raman work. The behaviour of R_1 and R_2 , as indicated by their half-band widths and separation, can also provide a warning on the appearance of shear effects (due to a non-hydrostatic environment), since both vary from their ambient, non-stressed values when such conditions ensue.²²

It is worth noting that in x-ray diffraction studies an alternative calibration procedure of far greater potential precision is now available. This relies on an internal x-ray standard single crystal such

Figure 1:6

A typical infrared gasket and sample after excursion to a pressure of 100 kbar.

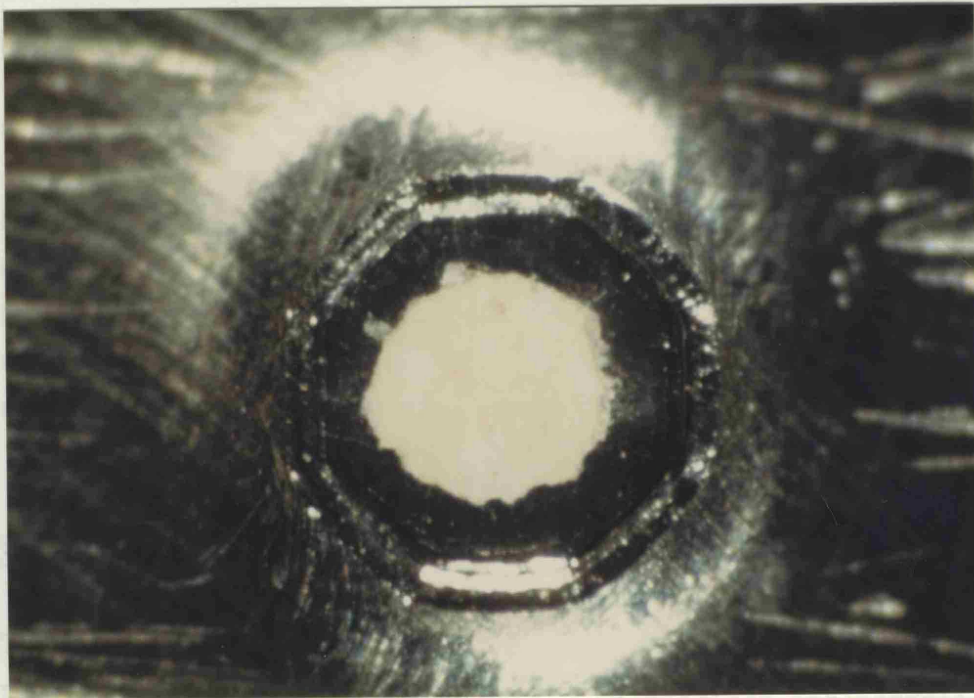
Deformation of the gasket hole is considerable but uniform, and is well within the confines of the diamond faces.

Figure 1:7

Catastrophic failure of a diamond anvil and gasket.

The remnants of both diamond and its araldite mounting can be seen surrounding the greatly deformed gasket hole.

as a crystalline rare gas, e.g. argon or neon, which can thus be used simultaneously as pressure medium and calibrant. These materials are



the former case the sample volume contained within the gasket is typically some 20-30 nanolitres with an initial cross-sectional area of less than $0.5 \mu\text{m}^2$. Thus, a two-stage reflecting beam condenser is employed to increase the energy throughput of the cell. The very nature of the laser source in a synchrotron experiment, by its high intensity and collimation, obviates the need for any special pre-cell condensing



transition is strongly first order with a ΔT value decrease all atoms retain the Wyckoff site occupancy of the parent phase. Further

as a crystalline rare gas, *e.g.* argon or neon, which can thus be used simultaneously as pressure medium and calibrant. These materials are highly compressible with unit-cell lengths that can be measured to 1 part in 10^4 . Such accuracy implies a pressure calibration sensitive to ± 5 bars at 50 kbar !

Since every excursion to high pressure is potentially catastrophic, insofar as the diamond anvils are concerned, Fig. 1:7, it is fortunate that in most cases it is failure of the gasket, the least expensive and most readily replaceable component, that is the limiting factor in terms of the maximum pressure obtainable.

1.6 Vibrational Spectroscopy at High Pressures²³

The optical requirements for effectively coupling the d.a.c. for use in the mid-infrared and Raman have been detailed previously.^{24,25} In the former case the sample volume contained within the gasket is typically some 20-50 nanolitres with an initial cross-sectional area of less than 0.64 mm^2 . Thus, a two element refracting beam condenser is employed to increase the energy throughput of the cell. The very nature of the laser source in a Raman experiment, *i.e.* its high intensity and collimation, obviates the need for any special pre-cell condensing optics, however, an off-axis ellipsoidal mirror greatly improves the efficiency of the standard collecting lens in both 0° and 180° scattering geometries.

It is important to stress that any conclusions drawn from the spectroscopic evidence alone, regarding the structural properties of a high pressure phase, can rarely provide an unequivocal characterisation in terms of assigning a unique space group. On the few occasions when this is possible, it is more likely to be a result of a fortuitous supergroup-subgroup relationship in a second order transition which provides for a single answer, than apodictic spectral evidence.

As an example, a recent energy-dispersive x-ray diffraction study (using synchrotron radiation) of the II \rightarrow IV transition in KNO_3 , has shown both phases to adopt the space group $Pnma \equiv D_{2h}^{16}$.²⁶ Although the transition is strongly first order with a 11.5 % volume decrease all atoms retain the Wyckoff site occupancy of the parent phase. Earlier

vibrational studies concluded that the two space groups could not be the same since the phase II and IV spectra were very different.^{27,28} The x-ray data show that this apparent anomaly is due to the packing in phase II which is very close to the symmetry of $\bar{P}3m1 \equiv D_{3d}^3$, and it is this which plays a dominant role in determining the vibrational selection rules.

1.7 The Concept of First and Second Order Transformations

In referring to the nature of a phase transition the terms first and second order are often encountered, and are used extensively throughout this thesis. Whilst it is not the purpose of this introduction to expound on the thermodynamic and symmetry properties of structural phase transformations (several such treatments are available),²⁹⁻³¹ a brief clarification of this terminology is necessary in order to understand many of the arguments presented herein.

A solid undergoes a phase transition when a particular phase of that solid becomes unstable under a given set of thermodynamic conditions. Ehrenfest classified transitions on the relation between the thermodynamic quantity undergoing discontinuity and the Gibbs free energy function, such that a transition is said to be of the same order as the partial derivative of the Gibbs free energy which shows a discontinuous change at the transition.³² Thus, from the relation

$$\begin{aligned} dG &= dE + PdV + VdP - TdS - SdT \\ &= VdP - SdT \quad (\text{since } dE = TdS - PdV) \end{aligned}$$

the first and second partial derivatives of the free energy may be written as

first order:

$$\left(\frac{\partial G}{\partial P}\right)_T = V \quad \left(\frac{\partial G}{\partial T}\right)_P = -S$$

second order:

$$\left(\frac{\partial^2 G}{\partial P^2}\right)_T = \left(\frac{\partial V}{\partial P}\right)_T = -V\beta \quad \left(\frac{\partial^2 G}{\partial P \partial T}\right) = \left(\frac{\partial V}{\partial T}\right)_P = V\alpha$$

$$\left(\frac{\partial^2 G}{\partial T^2}\right)_P = \left(-\frac{\partial S}{\partial T}\right)_P = -\frac{C_P}{T}$$

where C_p , α and β are the heat capacity, volume thermal expansivity and isothermal compressibility respectively.

Transitions of the first order are characterised by discontinuities in volume (if pressure induced) and latent heat (if temperature induced). A symmetry relationship between the crystal structures of the two phases involved in such a transition is not immediately apparent, since, in general, the two are structurally very different. However, by using several stages of both ascent and descent in symmetry a relationship may be constructed and a correlation between the various space groups achieved.³³ This process does, of course, require knowledge of both parent and daughter crystal structures; unfortunately, however, all too frequently the latter is unknown.

Spectroscopically, a first order transition is often seen as a marked change in the Raman or infrared spectra, a feature that reflects the major structural changes occurring. Hysteresis is also common and manifests itself as a difference in the transformation pressure/temperature in the forward and reverse directions.^{34,35} The volume discontinuity inherent in a first order transition can also be observed optically as a change in refractive index between phases.

In a second order change entropy and volume remain continuous, whilst heat capacity, thermal expansivity and compressibility undergo discontinuous change. It is almost always associated with some kind of disordering process in which the symmetry of the two phases is related: the symmetry of one phase is higher than that of the other and there is a direct supergroup-subgroup correlation between the two.³⁶ In most cases the more symmetric phase corresponds to lower pressure (higher temperature) and the less symmetric one to higher pressure (lower temperature), however, exceptions can and do occur. The changes observed in the spectra of such phases are often quite subtle, *e.g.* the I/IV transition in HgCl_2 (Chapter 4), and are clearly a reflection of the direct symmetry correlation. The lack of any volume discontinuity accompanying the transition results in there being no optically observable boundary between phases.

Although it is convenient to classify phase transitions on the above basis, many real transformations are truly of mixed order and as such exhibit features characteristic of both types. The first and second order descriptions are, nonetheless, useful first approximations in those cases where little information of the exact changes occurring is known.

1.8 Spectral Deconvolution

The absorption coefficient of an absorption or emission line, *i.e.* the real part of the frequency-dependent intensity, undergoing some sort of relaxation processes (line broadening), gives rise to a line shape known as a *Lorentzian*.³⁷ This is itself a specific type of Cauchy function, Fig. 1:8 A, and is characteristic of any system, *e.g.* a Raman transition, with an exponentially decaying dipole correlation function (the average magnetic dipole moment of the system).³⁸

In recording this profile the band shape becomes distorted by convolution with various instrumental effects, both optical and electronic in origin,³⁹ plus, under non-standard conditions, temperature and pressure effects. Whilst correction for band profiles subject to such perturbations is necessary in order to extract absolute intensities, quantitative band integrals and half band widths; for the purpose of obtaining accurate positional data, when confronted with complex band envelopes, they need not be considered, other than in their overall contribution to the band profile. These take the form of approximately *Gaussian* functions, resulting in curves of mixed Gauss and Cauchy character. Such a convolution can be effectively dealt with by a *Voigt* function, Fig. 1:8 B.⁴⁰ To this purpose, a fairly simple interactive computer programme (in terms of analysis) has been employed to find what can be considered as relatively accurate band positions,⁴¹ which in turn assist in the construction of mode pressure dependencies.

The programme initially requires an experimental band profile in digital form, either as collected by the data acquisition software or by digitising part of a 'hard copy' spectrum. Each band contributing to the envelope is then entered in terms of peak height, position, half band width and percentage Gaussian character. This last parameter determines

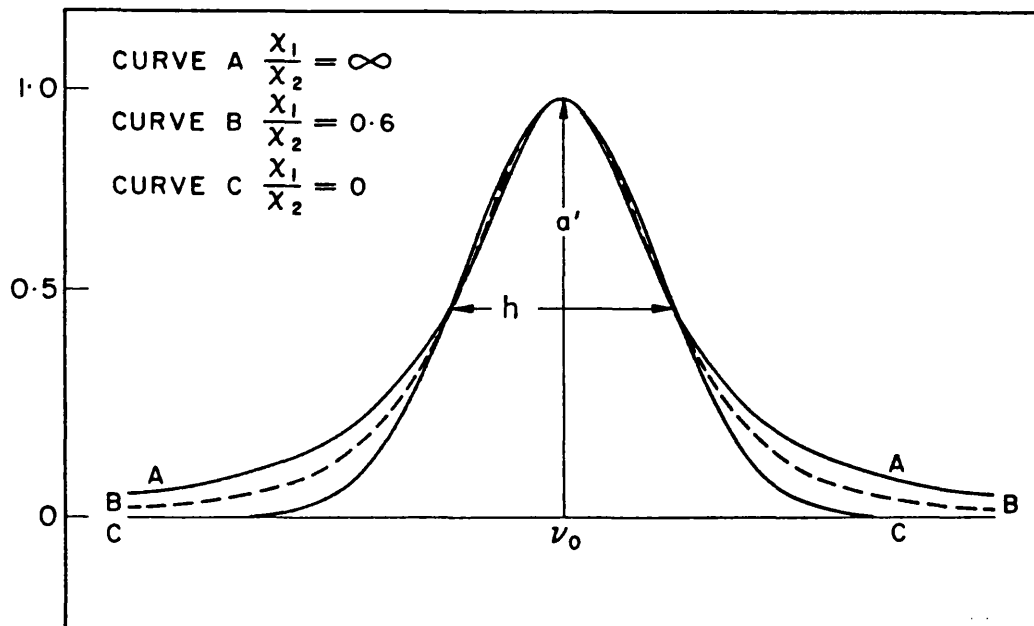
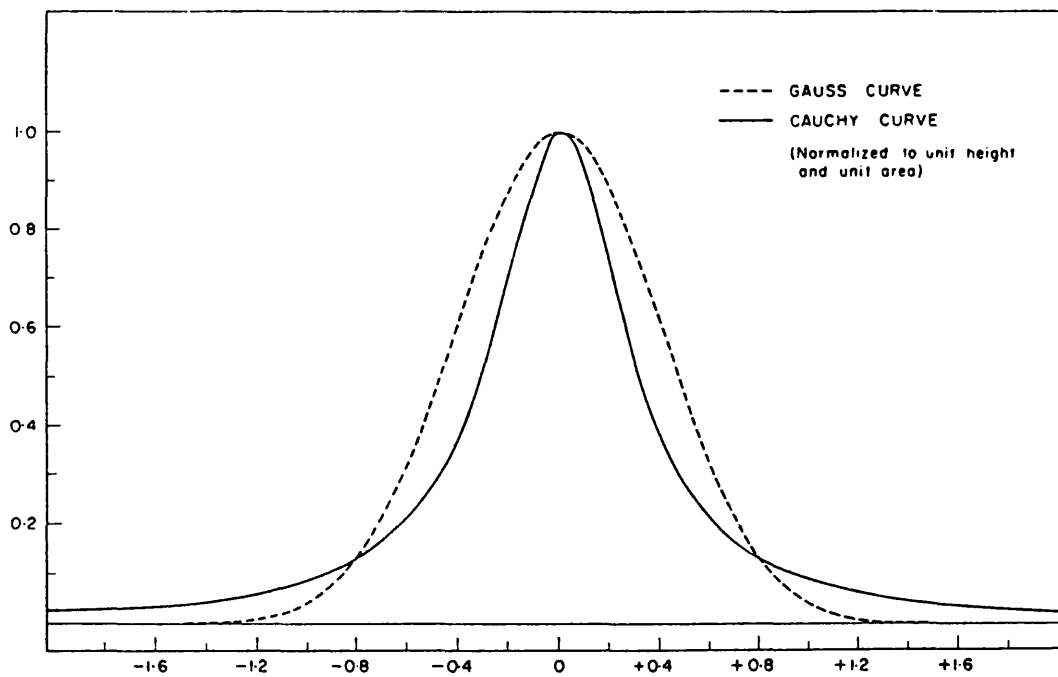
Figure 1:8

A.

Comparison of the profiles of Gauss and Cauchy curves of the same peak height and total area.

B.

Comparison of the Voigt function profile for $\chi_1/\chi_2 = 0.6$ (Curve B), with the profiles for the limiting cases corresponding to the Cauchy function (Curve A) and the Gauss function (Curve C).



the proportionality between the Cauchy and Gauss characteristics of the profile, *i.e.* the ratio of the constants χ_1/χ_2 in Fig. 1:8 B, such that if $\chi_1/\chi_2 = 0$ or $\chi_1/\chi_2 = \infty$ the Voigt function reduces to a pure Gauss or a pure Cauchy curve respectively. The programme then superimposes the individual bands together with their sum on the experimental profile, and by varying the individual band properties a best fit of observed to calculated profiles is obtained. It must be stressed that this process is not controlled by an iterative least squares fitting routine, although such would undoubtedly benefit the procedure, but is simply done by eye.

An important criterion for the use of this deconvolution technique is that the number of bands contributing to the experimental profile should be known. This is often quite easy to determine by inspection or from low temperature data, however, if many bands of similar intensities overlap closely to produce a broad feature with little structure, difficulties may occur. In such a case, the very process of attempting to fit what is subsequently found to be an incorrect number of bands, may alert the user to this fact.

The techniques of diamond selection and mounting, gasket preparation and sample loading have been explained elsewhere.^{42,43} All details of specific experimental procedures pertinent to a given study are set out at the beginning of each chapter.

1.9 References

1. P. W. Bridgman, *Proc. Amer. Acad.* **76**, 9, (1945).
2. C. E. Weir, E. R. Lipincott, A. V. Valkenburg and E. N. Bunting, *J. Res. Natl. Bur. Stand. (U.S.)* **63A**, 55, (1959).
3. J. C. Jamieson, A. W. Lawson and N. D. Nachtrieb, *Rev. Sci. Instrum.* **30**, 1016, (1959).
4. G. J. Piermarini and S. Block, *Rev. Sci. Instrum.* **46**, 973, (1975).
5. W. A. Bassett, T. Takahashi and P. W. Stook, *Rev. Sci. Instrum.* **38**, 37, (1967).

6. H. K. Mao and P. M. Bell, *Carnegie Inst. Washington Year Book* 77, 904, (1978).
7. G. Huber, K. Syassen and W. B. Holzapfel, *Phys. Rev. B* 15, 5123, (1977).
8. L. Merrill and W. A. Bassett, *Rev. Sci. Instrum.* 45, 290, (1974).
9. R. Appleby, Ph.D. Thesis, Leicester University, 1977.
10. Diacell Products Limited, 54 Ashtree Road, Oadby, Leicester.
11. D. M. Adams and S. K. Sharma, *J. Phys.* 10, 10, (1977).
12. A. Van Valkenburg, *Ind. Diamond Rev.* 24, Special Suppl., 17, (1964).
13. G. J. Piermarini, S. Block and J. D. Barnett, *J. Appl. Phys.* 44, 5377, (1973).
14. H. K. Mao and P. M. Bell, *Science* 203, 1004, (1979).
15. P. M. Bell and H. K. Mao, *Annu. Rep. Geophys. Lab., Washington D.C.* 80, 404, (1980-1981).
16. R. A. Forman, G. J. Piermarini, J. D. Barnett and S. Block, *Science* 176, 284, (1972).
17. P. M. Bell and H. K. Mao, *Carnegie Inst. Washington Year Book* 78, 665, (1979).
18. J. D. Barnett, S. Block and G. J. Piermarini, *Rev. Sci. Instrum.* 44, 1, (1973).
19. P. M. Bell and H. K. Mao, *Carnegie Inst. Washington Year Book* 74, 399, (1975).
20. H. E. King and C. T. Prewitt, *Rev. Sci. Instrum.* 51, 1037, (1980).

21. K. A. Goettel, W. C. Moss, R. Reichlin and S. Martin, European High Pressure Research Group, 24th Annual Meeting, University of Surrey, England, 1986.
22. D. M. Adams, R. Appleby and S. K. Sharma, *J. Phys. E* **9**, 1140, (1976).
23. J. R. Ferraro, "Vibrational Spectroscopy at High External Pressures - The Diamond Anvil Cell", Academic Press, London, 1984.
24. D. M. Adams and S. K. Sharma, *J. Phys. E* **10**, 838, (1977).
25. D. M. Adams and S. K. Sharma and R. Appleby, *Applied Optics*, **16**, 2572, (1977).
26. D. M. Adams, P. D. Hatton, A. Heath and D. R. Russell, *J. Phys. C*, in press.
27. Z. Iqbal, C. W. Christoe and F. J. Owens, *Ferroelectrics* **16**, 229, (1977).
28. J. A. Medina, Ph.D. Thesis, University of London, 1981.
29. "Vibrational Spectroscopy of Phase Transitions", Eds. Z. Iqbal and F. J. Owens, Academic Press, London, 1984.
30. C. N. R. Rao and K. J. Rao, "Phase Transitions In Solids - An Approach to the Study of the Chemistry and Physics of Solids", McGraw-Hill, New York, 1968.
31. J. Kochinski, "Theory of Symmetry Changes at Continuous Phase Transitions", Phase Transition Phenomena Volume 2, Elsevier, Amsterdam, 1983.
32. P. Ehrenfest, *Proc. Amsterdam Acad.* **36**, 153, (1933).
33. L. L. Boyle, unpublished work.
34. P. W. Bridgman, *Rec. Trav. Chem.* **51**, 627, (1932).

35. A. J. Dornell and W. A. McCollum, *High Temp. Sci.* **2**, 331, (1970).
36. C. Hermann, *Z. Kryst.* **69**, 533, (1929).
37. H. A. Lorentz, *Koninkl. Ned. Akad. Wetenschap. Proc.* **8**, 591, (1906).
38. J. I. Steinfeld, "Molecules and Radiation: An Introduction to Modern Molecular Spectroscopy", Mit Press, New York, 1978.
39. K. S. Seshadri and R. Norman Jones, *Spectrochim. Acta* **19**, 1013, (1963).
40. W. Voigt, *Münch. Ber.*, 603, (1912).
41. N. G. M. Pay, Leicester University, 1980.
42. A. D. Williams, Ph.D. Thesis, Leicester University, 1980.
43. D. M. Adams and S. J. Payne, *J. Chem. Soc., Farad. Trans. II* **70**, 1959, (1974).

CHAPTER 2

EXTENDED X-RAY ABSORPTION SPECTROSCOPY

An Introduction to the Theory, Experimental Procedure and Data Analysis

CHAPTER 2

EXAFS SPECTROSCOPY

2.1 Introduction

The availability of intense sources of continuous x-radiation, particularly in the form of dedicated storage rings, has stimulated the development of a technique for structure determination, which is particularly suited to studies of short-range changes in interatomic environment as induced by high pressure experiments. Extended x-ray Absorption Fine Structure, or EXAFS, spectroscopy has been known for over 60 years, but it is only in the last two decades that advances in the physical theory of EXAFS and in data analysis have changed the technique from a scientific curiosity to a quantitative tool for structure determination.

The first published observations of fine structure above an x-ray absorption edge occurred in 1920,¹ seven years after de Broglie first announced a measured absorption spectrum.² The initial theory provided by Kronig in 1931³ led to the development of what came to be known as long-range order (LRO) and short-range order (SRO) theories. The SRO theory derives from an assumption that only the near neighbours contribute to the EXAFS. This was indeed shown to be the case as the basic SRO model was improved upon, and in its modern form a single-scattering, SRO expression has been shown to be adequate in explaining the observed fine structure in most circumstances.

The x-ray absorption coefficient produced by the process of photoexcitation of an electron from a core state to a continuum state exhibits oscillations as a function of energy. These oscillations are the EXAFS. This final-state electron effect arises from the interference between the wavefunction of the outgoing electron with that part of itself which has been backscattered from surrounding atoms. The interference pattern reflects directly the net phaseshift of the backscattered electron wave. This largely comprises the product of the electron wavevector and the distance travelled, but which also includes contributions from the scattering process and from the passage of the

photoelectron out and back through the potential of the emitting atom. The amplitude of the oscillations depends on the number and electron scattering power of the scattering atoms. Consequently, analysis of the EXAFS can yield not only the distance but also the type and number of the nearest neighbours of the excited atom.

Fig. 2:1 shows the form of a typical absorption spectrum, which can be considered as a transition between two different regions.

(i) The threshold region. This includes features due to both pre-edge and edge regions, extending generally to energies up to 50 eV above threshold. This defines the limit of the x-ray absorption near edge structure, or XANES.⁴

(ii) The EXAFS region; spanning the region 50-1000 eV above the absorption edge.

The two ranges join smoothly, but are distinguished by an important theoretical criterion: in EXAFS the electron scattering is weak, modulations of the absorption cross-section are about 5% and a single-scattering theory suffices to interpret data; in XANES electron scattering is much stronger, modulations can be large and the interaction of the electron with the solid is no longer weak. It is the limited range of the final state photoelectrons in the energy region of interest (50-1000 eV) that permits a short range order description of EXAFS even in crystalline materials. Interpretation of the high pressure data presented here will be confined to the EXAFS alone.

2.2 Theory

The oscillatory part of the absorption coefficient, χ , the EXAFS, for the photoexcitation of an electron from an s-like initial state (K or L₁ edge) of an atom can be written as

$$\chi(E) = \frac{\mu(E) - \mu_0(E)}{\mu_0(E)} \quad (1)$$

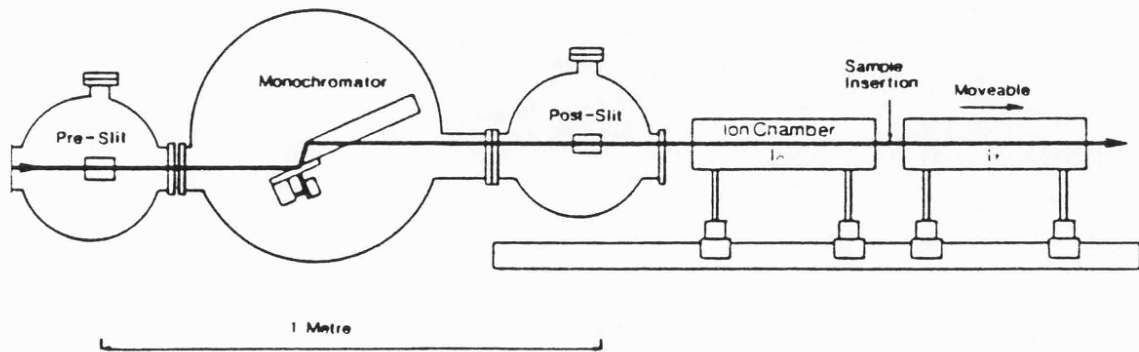
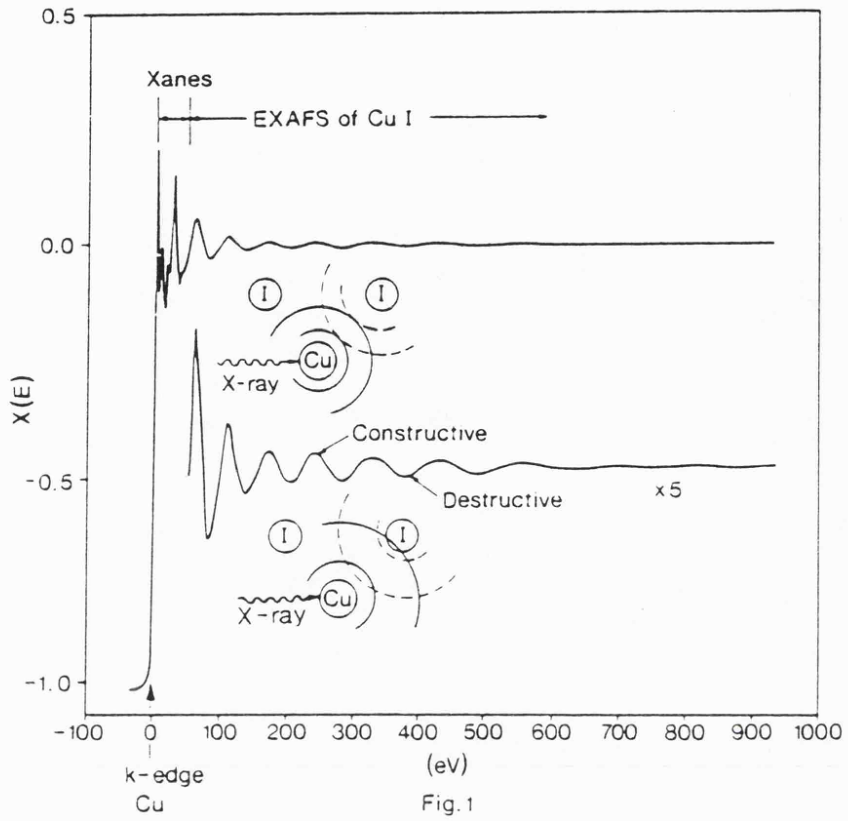
where μ and μ_0 are the observed and free atom absorption coefficients respectively. In order to relate $\chi(E)$ to structural parameters, it is necessary to convert the energy E into the photoelectron wavevector k ,

Figure 2:1

X-ray absorption spectrum of CuI showing the characteristic appearance of, and smooth transition between, XANES and EXAFS regions.

Figure 2:2

Experimental configuration of EXAFS station 7.1.



using the relationship

$$k = [(2m/\hbar^2)(E - E_0)]^{1/2} \quad (2)$$

where E is the incident photon energy and E_0 is the threshold energy for the liberation of a photoelectron wave at a given absorption edge. When the energy of the photoelectron is sufficiently high for the outgoing wavefunction to be approximated as a plane wave and, since except at energies close to the absorption edge only single-scattering need be considered, the EXAFS function χ in k space is given by⁵⁻⁷

$$\begin{aligned} \chi(k) = & \sum_j \frac{N_j}{kR_j^2} f_j(k, \pi) \exp(-2\sigma_j^2 k^2) \exp(-2R_j/\lambda) \\ & \times \sin(2kR_j + 2\delta'(k) + \Psi_j(k)) \end{aligned} \quad (3)$$

where k is the momentum of the photoelectron, N_j is the number of atoms at a distance R_j each with a backscattering amplitude $f_j(k, \pi)$,

$$\begin{aligned} f_j(k, \pi) = & |f_j(k, \pi)| \exp(j\Psi(k)) \\ = & \frac{1}{2jk} \sum_l (2l + 1) (\exp(2j\delta_l) - 1) (-1)^l \end{aligned} \quad (4)$$

where δ_l are the scattering phaseshifts, $l=1$ for K and L_1 edges and $l=2$ or 0 for $L_{2,3}$ edges. This latter term for a particular neighbour depends strongly on its atomic number and is, in general, only significant for low- Z atoms at small values of k ($< 10 \text{ \AA}^{-1}$). λ is the elastic mean free path of the photoelectron (only elastically scattered electrons can interfere, since those that have suffered inelastic losses will not have the right wavevector to contribute to the interference process). It is this factor which restricts the range of contributions to χ . The remaining exponential term is a Debye-Waller factor in which σ_j^2 is the mean square variation in interatomic distance between emitting and scattering atoms. This accounts for both thermal motion and static disorder, however, σ_j^2 is not simply the sum of the mean square thermal vibration amplitudes of the two atoms, since these motions are to some extent correlated.^{8,9} The Debye-Waller contribution is obtained under the assumption that the distribution of interatomic distances is Gaussian; a valid first approximation for the thermal motions and weak

static disorder found in crystalline solids. The term δ' is the phaseshift produced by the passage of the photoelectron through the emitting atom potential (the prime denotes that the central atom is photoexcited and is in general different from the neighbour), and Ψ_j is the phase of the backscattering amplitude. It is clear that the electron will be phase shifted by $2kR_j$ by the time it makes the return trip to the neighbour. To this must be added both $\Psi_j(k)$ and also twice the central atom phaseshift δ' .

The expression for χ is more complicated for absorption at $L_{2,3}$ edges, since the initial state of p symmetry can, by optical (dipole) selection rules, give a mixture of s and d outgoing photoelectron waves. Although the amplitude of the s wave is normally much smaller than that of the d wave, and can thus be ignored, the interference term between the s and d waves can yield significant differences for N_j , the effective coordination number.¹⁰

The great advantage of EXAFS in structural studies is that, in principle, it is possible to measure the EXAFS on the absorption edges of all atom types in the sample, thus obtaining the local environment (generally out to *ca.* 6 Å corresponding to 1-3 coordination shells) of each species separately. Equally important is the fact that the absorption measurement is entirely independent of the physical form of the sample and can be applied with about the same degree of accuracy (0.01 ~ 0.03 Å) to gases, liquids, solutions, solids or amorphous materials, and is hence potentially an extremely powerful technique.

The foregoing discussion represents only a simplistic view of the EXAFS process. The derivation of the equations requires that several assumptions be made regarding the importance of various physical phenomena. These include many-body effects, multiple-atom scattering, overlap of atomic potentials and inelastic processes. However, it is beyond the scope of this treatment to elaborate further on these topics. Details can be readily found in the extensive literature on x-ray absorption spectroscopy.¹¹⁻²⁰

2.3 Experimental Techniques

2.3.1 Synchrotron Radiation Sources

Today by far the majority of EXAFS work is done using synchrotron radiation. This intense source of x-radiation is produced when relativistic charged particles, such as electrons, travel in curved orbits in magnetic fields.

The characteristic properties of such radiation are well documented.^{17,18} Certain aspects make it a particularly valuable tool for x-ray absorption spectroscopy.

(i) Broad spectral bandwidth - the spectral distribution provides a smooth featureless continuum tunable over a wide energy range.

(ii) High intensity - several orders of magnitude more flux than is obtainable from bremsstrahlung output from the best conventional x-ray sources. This results in a greatly improved signal-to-noise ratio over such sources.

(iii) High Collimation - the radiation is strongly collimated in the vertical direction, allowing for high resolution measurements.

2.3.2 Transmission Experiments

The basic quantity to be determined in absorption spectroscopy is normally the absorption coefficient μ as a function of photon energy E . The more direct approaches to this involve measuring the normal incidence transmittance, the simplest and most commonly used method.

The experimental configuration for a transmission experiment, as is to be found at station 7.1 of the SRS, is shown in Fig. 3:1. The apparatus consists of five essential components: the x-ray source, the monochromator, the detectors, the sample, and the data acquisition system.

The x-ray source must and does provide a continuous spectrum of radiation. The x-ray monochromator is a Si single crystal which selects a particular photon energy or wavelength from that spectrum through diffraction according to Bragg's law:²¹

$$n\lambda_x = 2d \sin\theta \quad (5)$$

where n is the order of the reflection, λ_x is the x-ray wavelength, d is the spacing of the planes that diffract the radiation, and θ is the angle that the incident and reflected beams make with these planes. This equation can be rewritten in terms of photon energy $\hbar\omega$ as

$$\begin{aligned} \hbar\omega &= 2\pi\hbar cn/2d \sin\theta \\ &= (6199.3\text{eV})n/d \sin\theta \end{aligned} \quad (6)$$

where c is the speed of light and d is in angstroms.

After monochromatisation, the x-radiation passes through a detector (ionisation chamber) which monitors the total incident photon flux in the beam, I_0 . The beam then passes through a sample and the transmitted flux I_t is measured in a second ion chamber. The absorption of an x-ray photon of energy E by a sample of thickness x is given simply by

$$I_t(E) = I_0(E) \exp(-\mu_{\text{total}}(E)x) \quad (7)$$

where $\mu_{\text{total}}(E)$ is the total absorption coefficient of the sample.

The apparatus is typically controlled by a computer data acquisition system. The computer steps θ , and thus photon energy, through the region of interest, positions the sample to remain in the monochromatised x-ray beam, and acquires the digitised I_0 and I_t readings.

2.4 Data Analysis

In order for EXAFS to provide accurate structural and chemical information, three assumptions must be made.

(i) EXAFS is a simple sum of waves due to various types of neighbouring atoms (this implies that multiple-atom scattering is relatively unimportant).

(ii) The amplitude function is transferable for each type of backscatterer.

(iii) The phase function is transferable for each pair of atoms, *ie.* absorber and backscatterer.

Transferability implies that these functions are relatively insensitive to chemical bonding for energies 50-1000 eV above the absorption edge, such that once determined for a known system they can be applied to unknown systems which contain the same elements. Of these three assumptions, the phase transferability has proven to be the best approximation. The chemical effects on the phaseshift functions have been shown to have a decreasing influence for increasing energy, and can often to a large extent be compensated for by varying the threshold energy E_0 .

The single-scattering approximation works well except in cases where one atom is shadowed by another, that is when neighbouring atoms are arranged in a linear or nearly colinear array. In these cases the contributions from a few, strong, multiple-scattering paths (generally double and triple) must be included, since the outgoing photoelectron is strongly forward-scattered by the intervening atom. When equation (3) is used at low photoelectron energies errors are introduced into the calculated phase of $\chi(k)$, and hence erroneous determinations of interatomic distances. It is this low-energy (XANES) region of the spectrum which contains the majority of the structural information, thus it is obvious that in using an approximate expression much is lost. Use of the exact curved-wave theory developed to include these effects is both mathematically complex and computationally time-consuming.⁶ Fortunately, recent work has simplified this approach, enabling rapid, curved-wave EXAFS analysis for both single- and multiple-scattering contributions.^{22,23}

Finally, the amplitude transferability has been shown to be the weakest approximation due to the fact that it is highly sensitive to many variables including many-body effects, inelastic losses, and disorders.

These considerations need to be taken into account for normal EXAFS experiments. However, it has been shown that changes in the phaseshifts and backscattering amplitudes are independent (or at most very small) of pressure.²⁴ Thus, at least to the current upper pressure limits of such work (*ca.* 75 kbar), complete chemical transferability can be applied for

each new phase. This greatly simplifies the data analysis.

2.4.2 Background Subtraction and Normalisation

It is convenient to regard the total experimental absorption cross-section as the sum of two distinct contributions: the absorption cross-section μ , which contains the EXAFS information, and a slowly varying background absorption μ_{bg} . This background absorption reflects a contribution from both an instrument function (arising from the particular experimental setup), and a residual absorption by other elements and other edges of the same element. The removal of these effects is achieved using a least-squares fit to a set of different low-order polynomials over different k ranges of the absorption spectrum. The net effect of first subtracting μ_{bg} and then dividing by μ_0 is to normalise the EXAFS, the residual modulations oscillating evenly about zero. Finally, the conversion from μ vs E to $\chi(k)$ vs k is completed using the relationship in Eq.(2). This requires the identification of a value for E_0 , the start of the inner-shell \rightarrow continuum transition region, for which $k = 0$ for the final-state electrons. In general this is very difficult to accomplish; several different approaches having been taken to its determination. Quite often this problem is treated by keeping E_0 as an adjustable parameter to be varied in the EXAFS fitting procedure, an approach used in all analyses presented here.

2.4.3 Determination of Structural Parameters

The ultimate extraction of structural parameters from $\chi(k)$ can be achieved either in k space, r (distance) space, or using a combination of the two. The general form of the EXAFS function represents a series of damped, phase-modulated sinusoidal oscillations, so a natural way to approach its analysis is to take the numerical Fourier transform of the measured data over the EXAFS k range.²⁵ This results in a function similar to a radial distribution in r space. In the case of materials with sharply defined absorber-scatterer distances, this exhibits a number of peaks corresponding to the different shells of scatterers.

An alternative approach is the use of standard nonlinear curve

fitting routines. These attempt to fit the spectra in k space with some phenomenological models based on Eq. (3). More details of both techniques are available.^{17,20} Each of these methods has its respective problems and advantages, and it is common to employ a combination of the two in the final analysis.

The foregoing introduction to EXAFS; its physical origin, theoretical explanation, acquisition and analysis, is by no means an exhaustive treatment. It can be considered sufficient to indicate the capabilities and limitations of this spectroscopy, and to provide a basis for understanding the experimental results presented in Chapter 3.

2.5 References

1. H. Fricke, *Phys. Rev.* **16**, 202, (1920).
2. M. de Broglie, *Compt. Rendu.* **157**, 924, (1913).
3. R. de L.Kronig, *Z. Phys.* **70**, 317, (1931); **75**, 191, (1932).
4. M. Belli et al., *Solid State Comm.* **35**, 355, (1980).
5. D. E. Sayers, E. A. Stern, and F. W. Lytle, *Phys. Rev. Lett.* **27**, 1207, (1971); *Phys. Rev.* **B11**, 4836, (1975).
6. P. A. Lee and J. B. Pendry, *Phys. Rev.* **B11**, 2795, (1975).
7. C. Ashley and S. Doniach, *Phys. Rev.* **B11**, 1279, (1975).
8. S. J. Gurman and J. B. Pendry, *Solid State Comm.* **20**, 287, (1976).
9. J. B. Pendry, "Low Energy Electron Diffraction", Academic Press, London, 1974.
10. D. Norman, "X-ray Absorption (EXAFS & XANES) at Surfaces", SERC Daresbury Laboratory, Summer School, 1986.
11. E. A. Stern, *Sci. Am.* **234**, 96, (1976).

12. T. M. Hayes, *J. Non-Cryst. Solids* **31**, 57, (1978).
13. P. Eisenberger and B. M. Kincaid, *Science* **200**, 1441, (1978).
14. E. A. Stern, *Contemp. Phys.* **19**, 289, (1978).
15. D. R. Sandstrom and F. W. Lytle, *Annu. Rev. Phys. Chem.* **30**, 215, (1979).
16. G. S. Knapp and F. Y. Faradin, in "Electron and Positron Spectroscopies in Materials Science and Engineering", (O. Buck, J. Tien, and H. Marcus, eds.), p.243, Academic Press, New York, 1979.
17. H. Winick and S. Doniach, eds., "Synchrotron Radiation Research", Plenum, New York, 1980.
18. B. K. Teo and D. C. Joy, eds., "EXAFS Spectroscopy Techniques and Applications", Plenum, New York, 1981.
19. P. A. Lee, P. H. Citrin, P. Eisenberger, and B. M. Kincaid, *Rev. Mod. Phys.* **53**, 769, (1981).
20. T. M. Hayes and J. B. Boyce, *Solid State Physics* **37**, 173, (1982).
21. Eg. L. V. Azároff, "Elements of X-ray Crystallography" McGraw-Hill, New York, 1968.
22. S. J. Gurman, N. Binsted, and I. Ross, *J. Phys.* **C17**, 143, (1984).
23. S. J. Gurman, N. Binsted, and I. Ross, *J. Phys.* **C19**, 1845, (1986).
24. R. Ingalls et al., *J. Appl. Phys.* **51**, 3158, (1980).
25. D. E. Sayers, E. A. Stern, and F. W. Lytle, *Phys. Rev. Lett.* **27**, 1204, (1971).

CHAPTER 3

PRELIMINARY EXAFS INVESTIGATIONS OF HIGH PRESSURE PHASE TRANSITIONS

CHAPTER 3

PRELIMINARY EXAFS INVESTIGATIONS OF HIGH PRESSURE PHASE TRANSITIONS

3.1 Introduction

The application of EXAFS spectroscopy to the study of materials at high pressures is still very much in its infancy. To date, only some twenty to thirty papers have issued from such work, a fact that primarily reflects the requirement of a synchrotron radiation x-ray source. Since the publication of the first high pressure EXAFS study,¹ much interest has been concerned with accurately measuring bond length variations as a function of pressure, particularly when a structural phase change is involved.

The work presented here represents the initial results obtained on two systems with known high pressure phase transitions.

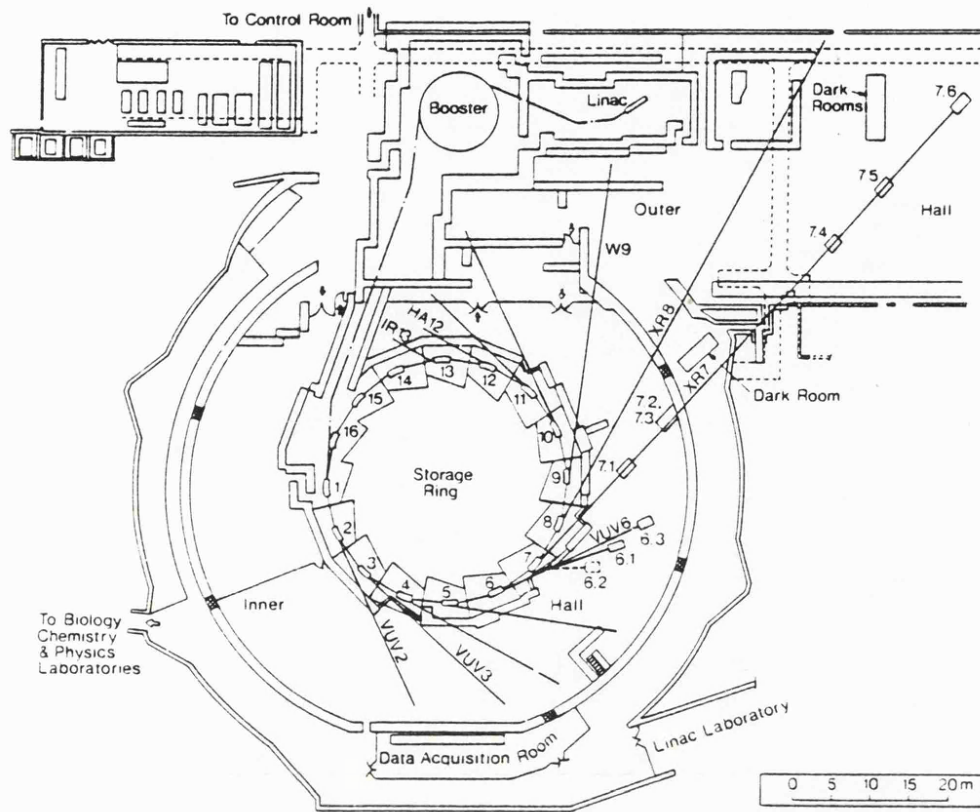
3.2 Experimental

All measurements were made at the Science and Engineering Research Council's Synchrotron Radiation Source (S.R.S.) using EXAFS station 7.1, Fig. 3:1. The transmission spectra were recorded at room temperature using the set-up shown schematically in Fig. 3:2, with the S.R.S. running at 1.8 GeV and typically 200 mA. Initial experiments using the unfocussed monochromatic beam, which has a size of *ca.* 1 mm x 12 mm at the sample, proved unsuccessful due to the low transmission of the d.a.c.. The intensity of the beam was improved by the insertion of a toroidal platinum-coated quartz mirror (58 cm long, 5 cm wide) in the beam line upstream of the experiment, although at the expense of some energy resolution. This increased the brightness by approximately sixty times and condensed the beam to a spot, at 17.3 m from the source, of size less than 0.5 mm x 6 mm. Use of the mirror does, however, restrict the range of accessible absorption edges to those falling between *ca.* 1.6-1.1 Å, Table 3:1, Fig. 3:3.

A Si(111) monochromator was used at a step increment and spectral

Figure 3:1

Plan and perspective views of the
S.E.R.C. Synchrotron Radiation
Source, Daresbury Laboratory.



SYNCHROTRON RADIATION SOURCE

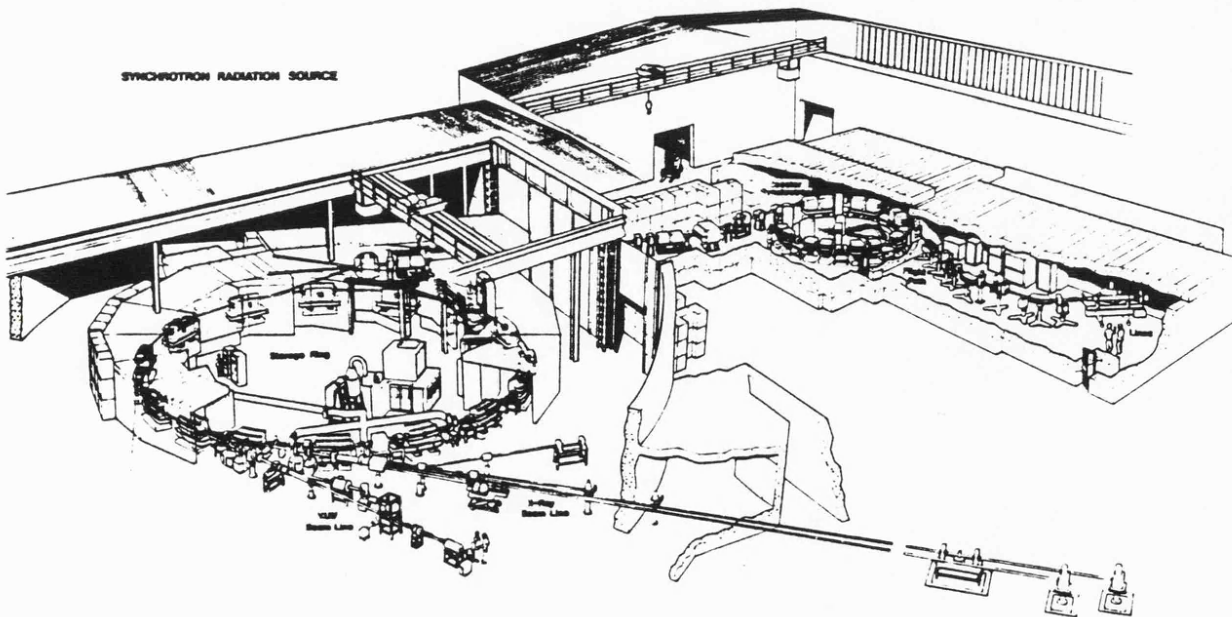
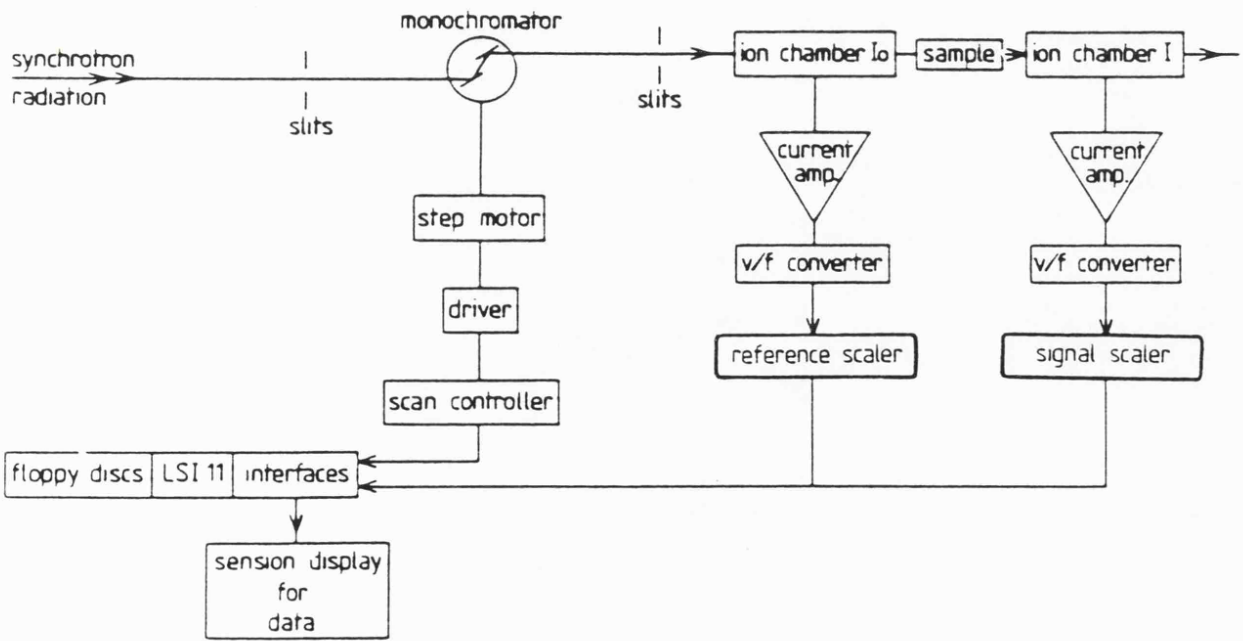
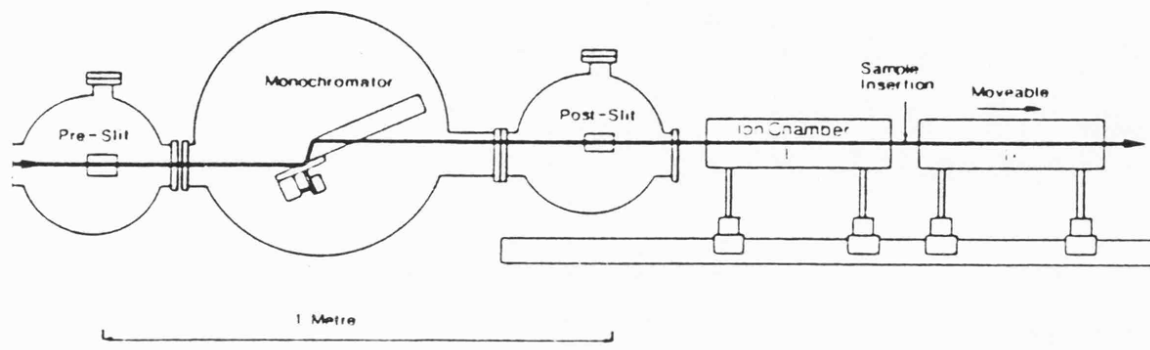


Figure 3:2

Experimental configuration for
transmission measurements at EXAFS
station 7.1.



Daresbury EXAFS system.

Figure 3:3

The operational synchrotron x-ray window for use with a d.a.c..

The region is delimited in normal use by the x-ray profiles of diamond and the S.R.S. operating at 2GeV. The extended window is only available on the Wiggler line, at EXAFS station 9.2.

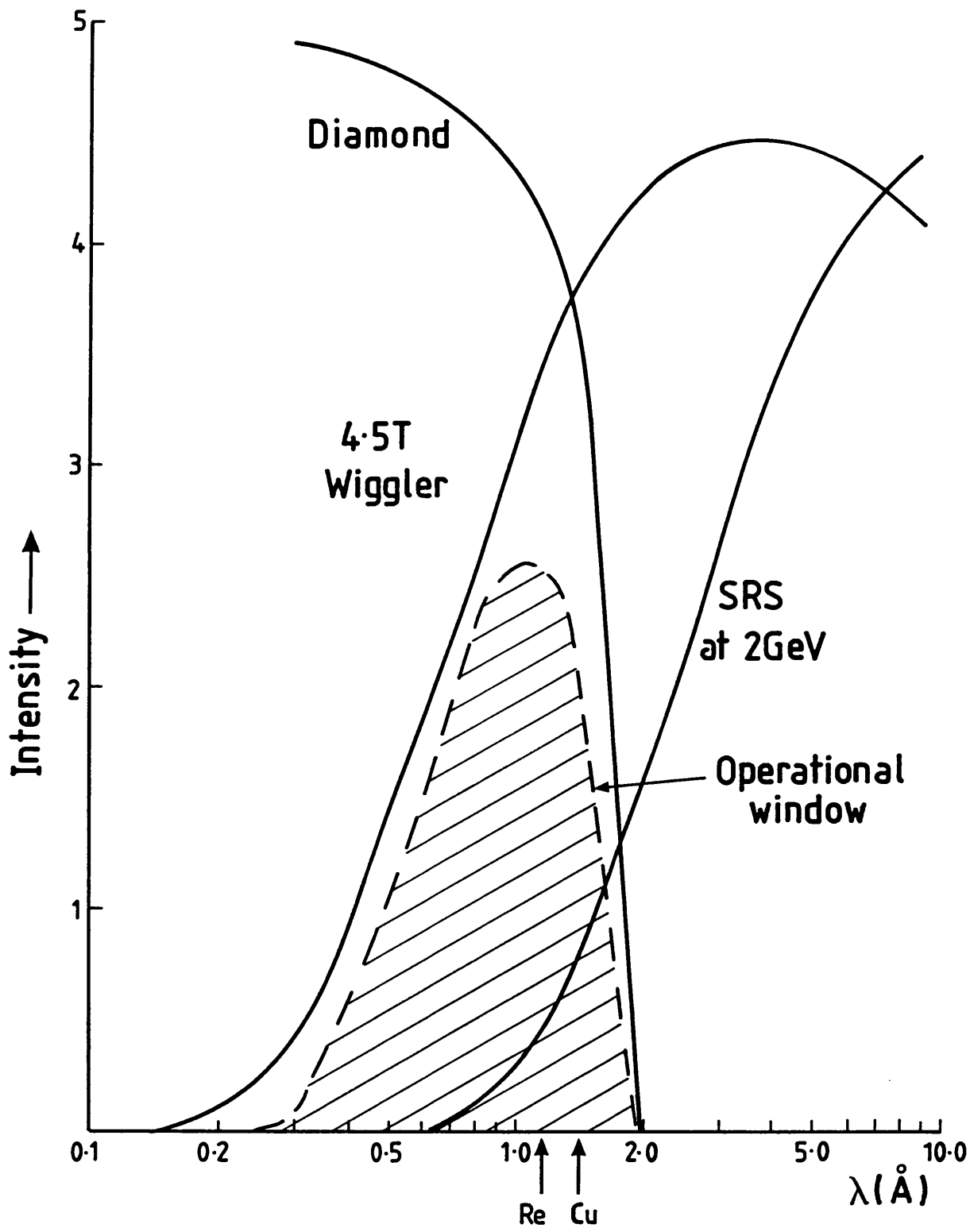


Table 3:1 Accessible K and L₁₁₁ absorption edges in Å (λ) and keV using the focussing mirror on station 7.1 of the S.R.S.

Element	K Edge		Element	L ₁₁₁ Edge	
	λ	keV		λ	keV
Co	1.60811	7.710	Dy	1.59025	7.797
Ni	1.48802	8.332	Hd	1.53529	8.076
Cu	1.38043	8.982	Er	1.48242	8.364
Zn	1.28330	9.661	Tm	1.43140	8.662
Ga	1.19567	10.369	Yb	1.38518	8.951
Ge	1.11652	11.105	Lu	1.34039	9.250
			Hf	1.29570	9.569
			Ta	1.25472	9.885
			W	1.21529	10.202
			Re	1.17720	10.532
			Os	1.14143	10.862
			Ir	1.10599	11.210

resolution of ~ 0.5 eV. Energy was calibrated by reference to the K absorption edges of copper or zinc, and the intensity of the incident and transmitted fluxes was monitored using ion chambers.

A Mk. III Diacell employing diamond anvils of 0.75 mm working face was used for both ungasketed and gasketed work. A collimator of 0.5 mm diameter, placed before the first ion chamber, matched the initial dimensions of the gasket hole. No ruby system was available at the time of these experiments; hence pressure was estimated and the transitions confirmed by optical examination.

3.3 Decacarbonyldirhenium

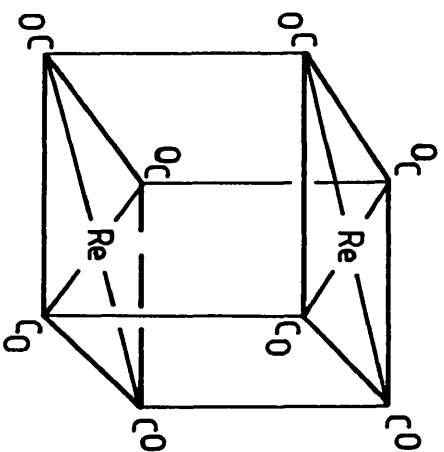
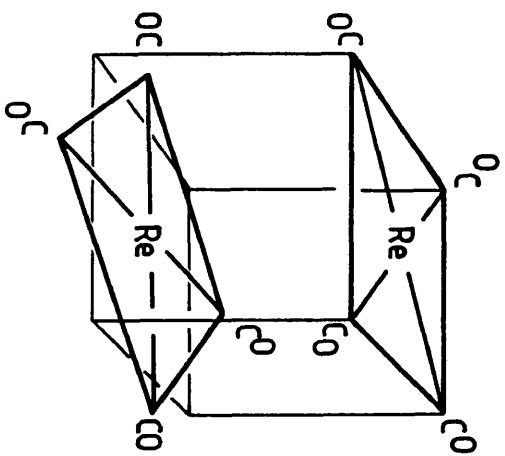
The metal-metal bonded carbonyl $\text{Re}_2(\text{CO})_{10}$ is known to undergo a first order phase transition at ~ 5 kbar, which is associated with rotation about the Re-Re bond.² This results in a change of molecular symmetry from a staggered (D_{4d}) to an eclipsed (D_{4h}) conformation, Fig. 3:4.

EXAFS spectra of both phases, recorded in an ungasketed d.a.c. at the L_{111} absorption edge of rhenium, are shown in Fig. 3:5. The sample was placed directly over the complete anvil faces and thus experienced a continuum of pressure. However, optical observations of the phase I/II Becke line indicated a large proportion to exist in the eclipsed form. Due to the nature of the transformation little change in the first and second coordination distances is to be expected, a fact born out by the similarity of the ambient and high pressure spectra. The most notable and significant feature of the data is an edge shift to higher energy of $\sim 1-2$ eV at the phase change.

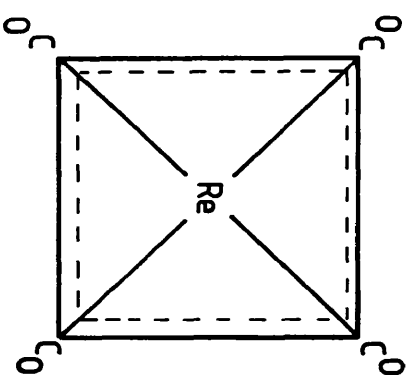
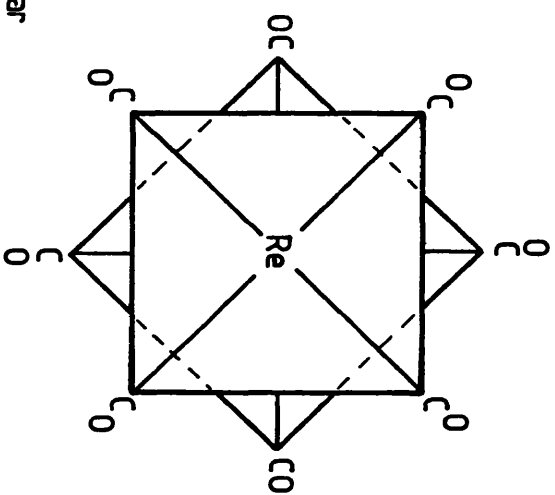
It is well known that x-ray absorption studies can yield information on the valence state of the element in question by probing the edge/near edge structure.³⁻⁵ In the mixed valence compound SmB_6 ,⁶ for example, a chemical shift of the absorption edge to ~ 8 eV higher binding energy is observed when the Sm is trivalent rather than divalent. This can be accounted for by a simple electrostatic argument, since more energy is required to remove a core electron as the positive charge on the ion is increased. On this basis the $\text{Re}_2(\text{CO})_{10}$ edge shift can be seen as a change of electron density at Re. Such a conclusion is

Figure 3:4

The staggered to eclipsed phase transition in dirheniumdecarbonyl.



5 kbar



Staggered

D_{4h}

Eclipsed

D_{4h}

indeed consistent with the earlier Raman high pressure data which indicated that further back donation of charge on to the carbonyl groups takes place at the transition.

3.4 Caesium, Isopropyl and Triethylammonium Tetrachlorocuprates

In the series $(R_nNH_{4-n})_2CuX_4$, (R = alkyl or aryl, X = Br, Cl, n = 1 to 4), several members are known to exhibit a reversible, first order thermochromic phase transition at relatively low temperatures (40-60 °C).⁷ The phenomenon is associated with a change in coordination geometry around the copper(II), from essentially square-planar in the low temperature phase to distorted tetrahedral in the high temperature form. Pressure studies have also suggested a transition to a phase in which strictly square-planar geometry prevails.^{8,9}

The thermochromic behaviour reported for these compounds, however, is not necessarily indicative of a first order phase transition involving a coordination geometry change at the copper. In the series $(RNH_3)_2CuCl_4$, R = CH₃, C₂H₅ *etc.* and in $(DMA)_2CuCl_4$ both differential thermogravimetric analysis and electronic absorption measurements have provided no evidence to support the occurrence of a structural change.¹⁰ In these cases the thermochromism has been shown to be due solely to a change in the line width of the electronic absorption band.

As a preliminary investigation, the EXAFS spectra of bis-(triethylammonium) tetrachlorocuprate(II), $[(C_2H_5)_3NH]_2CuCl_4$, have been recorded at the K absorption edge of copper, in order to probe the local geometry of the $[CuCl_4]^{2-}$ ion up to 15 kbar in a gasketed d.a.c., Fig. 3:6. Ambient spectra of both caesium and bis-(isopropylammonium) tetrachlorocuprates, Cs_2CuCl_4 and $[(CH_3)_2CHNH_3]_2CuCl_4$, were also collected to obtain accurate relative phaseshifts for the subsequent analysis of the high pressure data. (Henceforth an abbreviated form will be used to indicate the type and multiplicity of the alkyl ammonium group concerned *eg.* TEA = triethylammonium, IPA = isopropylammonium *etc.*).

3.4.1 Data Reduction and Analysis

EXAFS data reduction and analysis was carried out using three

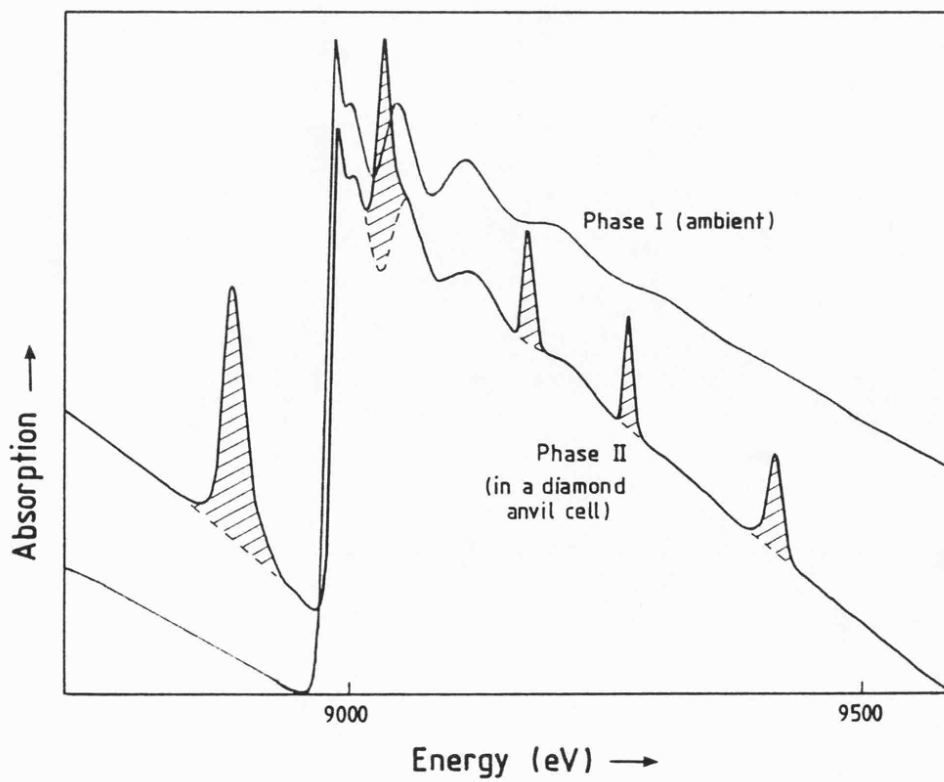
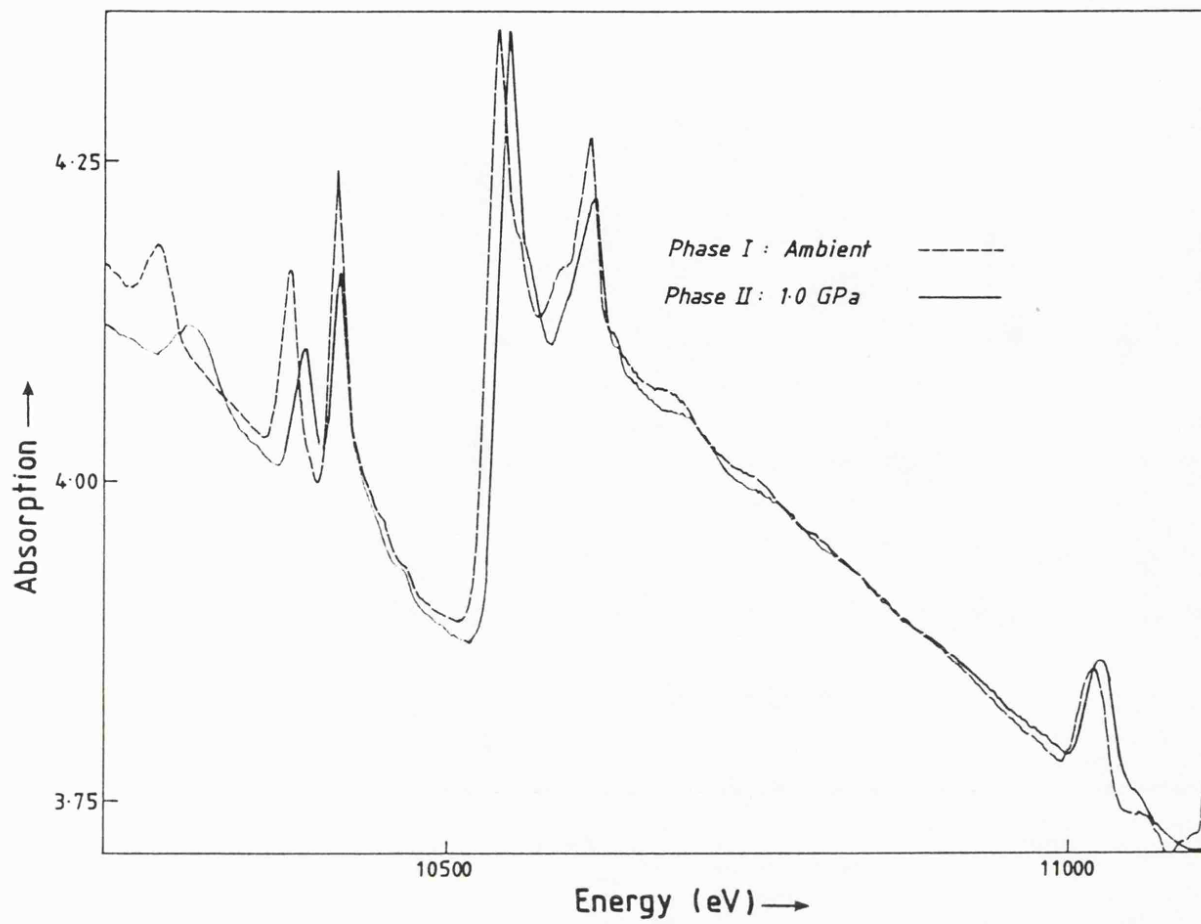
Figure 3:5

Ambient and ~ 10 kbar (1 GPa) EXAFS spectra of $\text{Re}_2(\text{CO})_{10}$, clearly showing the edge shift between phases I and II.

Figure 3:6

Ambient and ~ 15 kbar EXAFS spectra of bis-(triethylammonium) tetrachlorocuprate(II).

The dashed lines represent the phase II spectrum after removal of the Bragg diffraction peaks from the diamond anvils.



interactive computer programmes available in the SRS Programme Library.¹¹ Briefly, their function is as follows:

EXCALIB: starting from the experimental data file, this produces normalised spectra of absorption/fluorescence versus electron energy in eV and Hartrees.

EXBACK: takes absorption data from EXCALIB and produces normalised EXAFS spectra and Fourier transforms.

EXCURVE: enables curve fitting to the normalised spectrum or its Fourier transform using calculated phaseshifts and the curved wave approximation.

In measuring EXAFS using a d.a.c., a significant problem in analysis occurs when the data are convoluted with Bragg diffraction peaks from the single crystal diamond anvils. Each diamond yields a unique Bragg signature which is dependent upon both pressure and orientation of the cell with respect to the x-ray beam Fig. 3:7. It is essential that these features, which are generally several times the amplitude of the EXAFS modulations, are effectively removed since their presence prevents further data analysis. Two approaches are possible: (i) experimental manipulation of the cell; (ii) mathematical deconvolution.

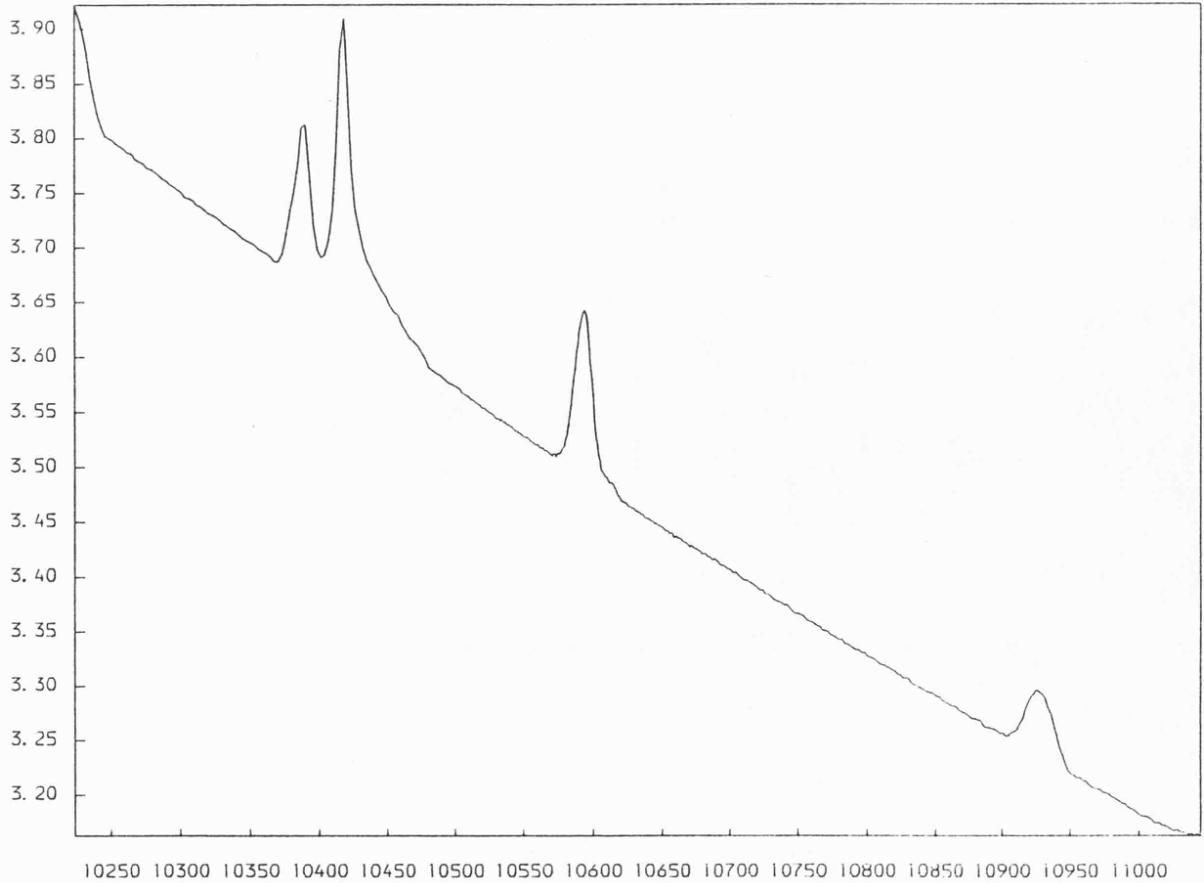
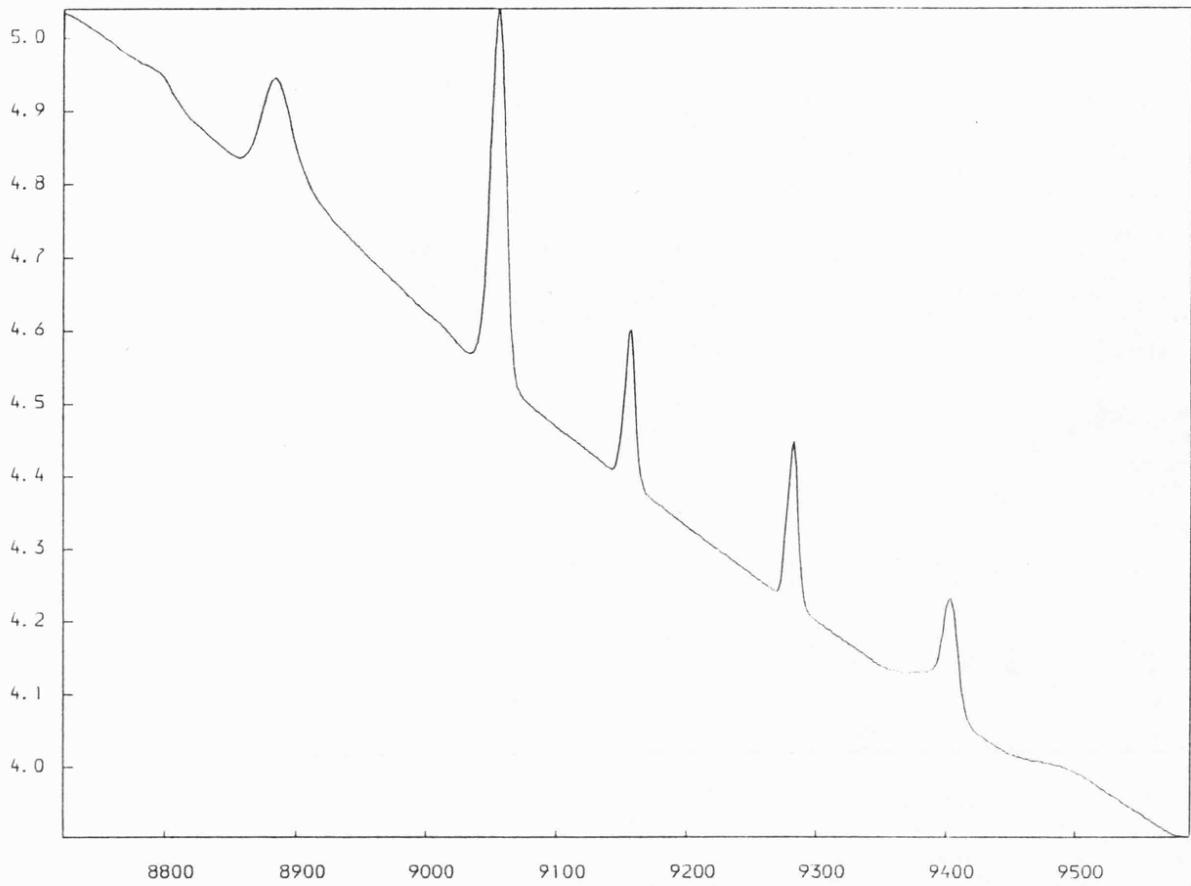
Route (i) involves rotating the d.a.c. about the beam axis, thus casting the Bragg reflections into differing energies and, after omitting the spurious peak regions, summing the data.¹² This process is obviously a somewhat hit or miss affair, and as such method (ii) is preferred, the Bragg peaks being removed by both linear and higher order polynomial interpolations.

As a result of these problems some d.a.c. studies have concentrated on the XANES region, the narrow energy range of which enables Bragg reflections to be readily avoided.^{13,14} Several high pressure investigations have been made using Bridgman anvil devices or specially designed cells, which by using boron/tungsten carbide anvils or Be plates avoid such problems.^{1,15,16} Their use does, however, preclude the use of the ruby pressure scale and limits observations to below 100 kbar, although, at present, little work at pressures higher than this has been attempted.

Figure 3:7

Typical background normalisations in the energy regions of the Cu K (A) and Re L_{111} (B) edges, showing the Bragg diffraction profiles from an empty diamond anvil cell.

Absorption →



Energy (eV) →

Initial analysis of the ambient spectra using a single scattering, spherical wave calculation gave Cu-Cl bond distances shorter than those reported by x-ray diffraction measurements, Table 3:2. The longer Cu-Cl distance and poorer fit on the right hand side of the Fourier transform obtained for the isopropyl salt do, however, reflect the difference in $[\text{CuCl}_4]^{2-}$ geometry in that compound. Thus, in $(\text{IPA})_2\text{CuCl}_4$, the copper coordination is one-third square-planar and two-thirds tetrahedrally distorted, with one or two additional chlorine atoms occupying the pseudo-octahedral positions at considerably longer distances (3.07 - 3.33 Å).¹⁸

Improved distances were obtained by fixing the Cu-Cl value at the known diffraction determined bond length in $(\text{TEA})_2\text{CuCl}_4$,¹⁹ and refining the phaseshifts. These were shown to be transferable to Cs_2CuCl_4 , improving both the distance (from 2.195 to 2.215 Å) and the fit index (from 8.48 to 2.17). This gave a very robust refinement insensitive to changes in the Fourier window and E_0 .

The refined phaseshifts were next used to analyse the high pressure data for $(\text{TEA})_2\text{CuCl}_4$. The bond lengths so obtained indicate that the Cu-Cl distance is little affected by pressure up to 15 kbar, although a slight contraction is indicated. This was found for all analyses, irrespective of background subtraction, the manner of Bragg peak removal (linear or curved), Fourier filtering and variation in E_0 . The best fits gave a Cu-Cl distance of 2.235 ± 0.002 Å which corresponds to a bond compressibility of *ca.* 4×10^{-4} Å kbar⁻¹.

3.6 Structural Conclusions

The crystal structure analyses on a large number of salts which contain discrete $[\text{CuCl}_4]^{2-}$ ions have been reported in the literature.¹⁷⁻²⁷ From these it is clear that there exists a continuum of $[\text{CuCl}_4]^{2-}$ geometries from nearly tetrahedral to square-planar. The extent of the flattening from tetrahedral symmetry can be judged from the magnitude of the average of the two *trans* Cl-Cu-Cl angles, Table 3:3. It has been shown that it is primarily the electrostatic repulsions between chlorine atoms which favour tetrahedral geometry, whilst the presence of hydrogen bonding reduces the effective charge on the chlorine atoms and allows the $[\text{CuCl}_4]^{2-}$ ion to move towards the square-

Table 3:2 Comparison of calculated average Cu-Cl bond distances with diffraction determined measurements.

Compound	Cu-Cl distance Å	Fit index ^d (k ³ weighting) ^e
(TEA) ₂ CuCl ₄	2.219 ^a	1.06
(IPA) ₂ CuCl ₄	2.239 ^b	1.26
Cs ₂ CuCl ₄	2.195 ^c	8.48

using refined phaseshifts

(TEA) ₂ CuCl ₄	2.241	0.74
Cs ₂ CuCl ₄	2.215	2.17

Crystallographic values:

a (TEA)₂CuCl₄; 2.237–2.247, average 2.241

b (IPA)₂CuCl₄; 2.233–2.290, average 2.262

c Cs₂CuCl₄; 2.220–2.244, average 2.230

d The fit index is a measure of the goodness of fit between experiment and theory; the lower the value the better the fit.

e k³ weighting represents a weighted spectrum, k³χ(k) versus k, to compensate for the diminishing amplitudes at high k values.

planar geometry favoured by the crystal field stabilisation.²⁸ Thus, the greater the potential for hydrogen bonding, the closer the $[\text{CuCl}_4]^{2-}$ ions approach square-planar coordination. A further structural characteristic which favours this latter geometry is the formation of intermolecular Cu--Cl interactions between neighbouring $[\text{CuCl}_4]^{2-}$ ions, such as are found in $(\text{EA})_2\text{CuCl}_4$ and $(\text{IPA})_2\text{CuCl}_4$.

These effects manifest themselves as an increase in the average Cu-Cl distance, on passing from near tetrahedral to square planar geometry, Table 3:3. If the pressure induced transition in $(\text{TEA})_2\text{CuCl}_4$ is indeed to a phase with planar $[\text{CuCl}_4]^{2-}$ ions, then the average Cu-Cl value should be expected to increase in the above manner. The EXAFS analyses indicate exactly to the contrary, however, this behaviour can be rationalised as the net result of several opposing effects.

A common response to increasing pressure is a shortening of bond distances, which in a vibrational study would present as a hardening of phonon frequency. Thus, it is reasonable to assume that although pressure favours intermolecular interactions which act to increase the Cu-Cl distance, by 15 kbar the direct compression of the structure plays the dominant role, and a slight contraction is observed. The exact nature of these effects and their pressure dependence it is possible only to speculate upon at this stage, without data from a spread of pressures. Suffice it to say, that shortening of the Cu-Cl bond may well be immediate upon application of pressure or, on the other hand, it is conceivable that an initial lengthening occurs, which shows a maximum before contraction begins to dominate.

Optically, insofar as a Becke line delineates the two phases, the transition appears first order. However, no colour change is seen as should be expected for a change in Cu-Cl geometry. This observation does indeed suggest that the first transition in $(\text{TEA})_2\text{CuCl}_4$ is likely to be one involving primarily the triethylammonium N-H--Cl hydrogen bonding, rather than one affecting the Cu-Cl coordination to the extent where square-planar geometry is attained. Since transitions to such a structure have been reported for Cs_2CuCl_4 and Cs_2CuBr_4 at ~ 60-80 kbar and for $(\text{IPA})_2\text{CuCl}_4$ at ~ 20 kbar,^{8,9} it seems likely that a similar transformation will also be affected in the triethyl salt. This is to be expected at a pressure between 20 and 60 kbar assuming a direct correlation between initial stereochemistry and the transition pressure,

Table 3:3 Average *trans* Cl–Cu–Cl angles and Cu–Cl distances in compounds containing discrete $[\text{CuCl}_4]^{2-}$ anions.

Geometry	<i>trans</i> Cl–Cu–Cl angle	Cu–Cl distance (Å)	Compound	
Distorted Tetrahedral	128°	2.216	$[(\text{CH}_3)_4\text{N}]_2\text{CuCl}_4$	
	129		$[\text{C}_{12}\text{H}_{15}\text{N}_2]\text{CuCl}_4$	
	129	2.230	Cs_2CuCl_4	
	132		$[(\text{C}_6\text{H}_5)_3\text{NCH}_3]_2\text{CuCl}_4$	
	135	2.241	$[(\text{C}_2\text{H}_5)_3\text{NH}]_2\text{CuCl}_4$	
	136		$[(\text{CH}_3)_2\text{NH}_2]_3\text{ClCuCl}_4$	
	143		$(\text{C}_{13}\text{H}_{19}\text{N}_2\text{OS})_2\text{CuCl}_4$	
	155	2.262	} $[(\text{CH}_3)_2\text{CHNH}_3]_2\text{CuCl}_4$	
	180	2.280		
		180	2.274	$[(\text{NH}_3\text{CH}_2\text{CH}_2)_2\text{NH}_2]\text{ClCuCl}_4$
		180	2.281	$(\text{C}_2\text{H}_5\text{NH}_3)_2\text{CuCl}_4$
	Square-Planar			

as seems to be the case for the caesium and isopropyl salts, *i.e.* the nearer the ambient $[\text{CuCl}_4]^{2-}$ geometry is to square-planar the lower the transition pressure.

3.7 Summary

Preliminary EXAFS spectra have been successfully recorded at high pressure in a d.a.c. using a synchrotron radiation x-ray source. The problem of Bragg peak removal, inherent in studies using a diamond anvil cell, has been overcome. Ungasketed work on $\text{Re}_2(\text{CO})_{10}$ has shown a significant shift in the Re L_{111} edge at the staggered to eclipsed transition at 5 kbar. This is consistent with the delocalisation of charge on to the ligands observed previously by Raman spectroscopy. Several organoammonium tetrachlorocuprates have provided accurate phaseshifts for the analysis of the high pressure data from $[(\text{C}_2\text{H}_5)_3\text{NH}]_2\text{CuCl}_4$. This indicates a slight contraction of the average Cu-Cl bond distance by 15 kbar. The nature of the first transition in this compound is discussed in terms of a geometry change at copper and intermolecular interactions.

3.8 References

1. R. Ingalls, G. A. Garcia and E. A. Stern, *Phys. Rev. Lett.* **40**, 334, (1978).
2. D. M. Adams, P. D. Hatton, A. C. Shaw and T. K. Tan, *J. C. S. Chem. Comm.*, 220, (1981).
3. H. Launois, M. Rawiso, E. Holland-Moritz, R. Pott and D. Wohlleben, *Phys. Rev. Lett.* **44**, 1271, (1980).
4. R. M. Martin, J. B. Boyce, J. W. Allen and F. Holtzberg, *Phys. Rev. Lett.* **44**, 1275, (1980).
5. G. Wortmann, K. Syassen, K. H. Frank, J. Feldhaus and G. Kaindl in "Valence Instabilities", (P. Wachter and H. Boppard eds.), 159, 1982.

6. E. E Vainshtein, S. M. Blokhin and Y. B. Paderno, *Sov. Phys. - Solid State (Engl. Transl.)* **6**, 2318, (1965).
7. A. Uehara et al., *Thermochim. Acta* **77**, 299, (1984).
8. R. D. Willett, J. R. Ferraro and M. Choca, *Inorg. Chem. B*, 2919, (1974).
9. P. J. Wang and H. G. Drickamer, *J. Chem. Phys.* **59**, 559, (1973).
10. R. D. Willett, J. A. Haugen, J. Lebsack and J. Morrey, *Inorg. Chem.* **13**, 2510, (1974).
11. G. P. Diakun, G. N. Greaves, S. S. Hasnain and P. D. Quinn, "X-Ray Absorption Spectroscopy", Technical Memorandum, Daresbury Laboratory, 1984.
12. O. Shimomura, T. Fukamachi, T. Kawamura, S. Hosoya, S. Hunter and A. Bienenstock, *Japan J. Appl. Phys.* **17**, 221, (1978).
13. R. Ingalls, J. M. Tranquada, J. E. Whitmore and E. P. Crozier, in "EXAFS and Near Edge Structures", Proceedings of the International Conference. Frascati, 1982; 154, Springer-Verlag, Berlin, 1983.
14. J. Röhlér, G. Krill, J. P. Kappler and M. F. Ravet, in "EXAFS and Near Edge Structures", Proceedings of the International Conference, Frascati, Italy, 1982; 213, Springer-Verlag, Berlin, 1983.
15. A. Werner and H. D. Hochheimer, *Rev. Sci. Instrum.* **53**, 1467, (1982).
16. R. Ingalls, E. D. Crozier, J. E. Whitmore, A. J. Seary and J. M. Tranquada, *J. Appl. Phys.* **57**, 3158, (1980).
17. J. A. McGinnety, *J. Am. Chem. Soc.* **94**, 8406, (1972).
18. D. N. Anderson and R. D. Willett, *Inorg. Chim. Acta* **8**, 167, (1974).
19. J. Lamotte-Brasseur, L. Dupont and O. Dideberg, *Acta Cryst.* **B29**, 241, (1973).

20. S. H. Simonsen and R. L. Harlow, *Am. Cryst. Assoc. Ser. 2* 5, 25, (1977).
21. J. P. Steadman and R. D. Willett, *Inorg. Chim. Acta* 4, 367, (1970).
22. B. Morrison and E. C. Lingafelter, *J. Phys. Chem.* 65, 50, (1961).
23. J. H. Russell and S. C. Wallwork, *Acta Cryst.* B25, 1691, (1969).
24. M. Bonamico, G. Dessy and A. Vaciago, *Theor. Chim. Acta* 7, 367, (1967).
25. R. D. Willett and M. L. Larsen, *Inorg. Chim. Acta* 5, 175, (1971).
26. A. C. Bonamartini, M. Nardelli, C. Palmieri and C. Pellizzi, *Acta Cryst.* B27, 1725, (1971).
27. G. L. Ferguson and B. Zaslow, *Acta Cryst.* B27, 849, (1971).
28. L. L. Lohr and W. N. Lipscomb, *Inorg. Chem.* 2, 911, (1963).

CHAPTER 4

A RAMAN SCATTERING STUDY OF THE PHASE BEHAVIOUR OF THE MERCURY (II)

HALIDES HgX_2 , $\text{X} = \text{Cl, Br}$

CHAPTER 4

A RAMAN SCATTERING STUDY OF THE PHASE BEHAVIOUR OF THE MERCURY (II) HALIDES HgX_2 , ($\text{X} = \text{Cl}, \text{Br}$)

4.1 Introduction

The behaviour of HgCl_2 and HgBr_2 under high static pressure was first outlined by Bridgman in 1937.¹ For HgCl_2 these compression measurements showed only one phase transition up to 45 kbar at ambient temperature. More recently an n.q.r. study up to 16 kbar and at temperatures in the range 246–355 K revealed a second order transition, from $\text{HgCl}_2(\text{I})$ to $\text{HgCl}_2(\text{IV})$, below this at 6.6 kbar,² Fig. 4:1.

The phase diagram for HgBr_2 is shown in Fig. 4:2.^{1,3,4} It exists in four polymorphic modifications up to 45 kbar at ambient temperature. Both materials have been previously examined using Raman and i.r. spectroscopy under conditions of, or near, hydrostatic compression up to ca. 40 kbar.⁴ However, the evidence for the I/IV transition in HgCl_2 and the I/II transition in HgBr_2 remains unclear.

In this present study Raman spectra have been obtained for HgCl_2 to 145 kbar and HgBr_2 to 100 kbar. A new first order phase change has been found in HgCl_2 at 79.0 kbar, and all phases exactly characterised by their phonon pressure dependencies.

4.2 Experimental

Reagent grade HgCl_2 and HgBr_2 were recrystallised twice from ether before use. Raman spectra were obtained using ca. 130 mW 514.5 nm Ar^+ radiation at the sample, the spectral slit width varying from 0.5 to 1.0 cm^{-1} , the latter only at pressures > 70 kbar. The mercuric halides readily attack inconel; molybdenum gaskets of initial dimensions 0.15 mm (thickness) and 0.4 mm (hole diameter), being successfully used in their place. A Dynocell was used for work above 70 kbar and the hole diameter decreased to 0.28 mm. Data were acquired from several loadings, using

Figure 4:1

The phase diagram of HgCl_2 .

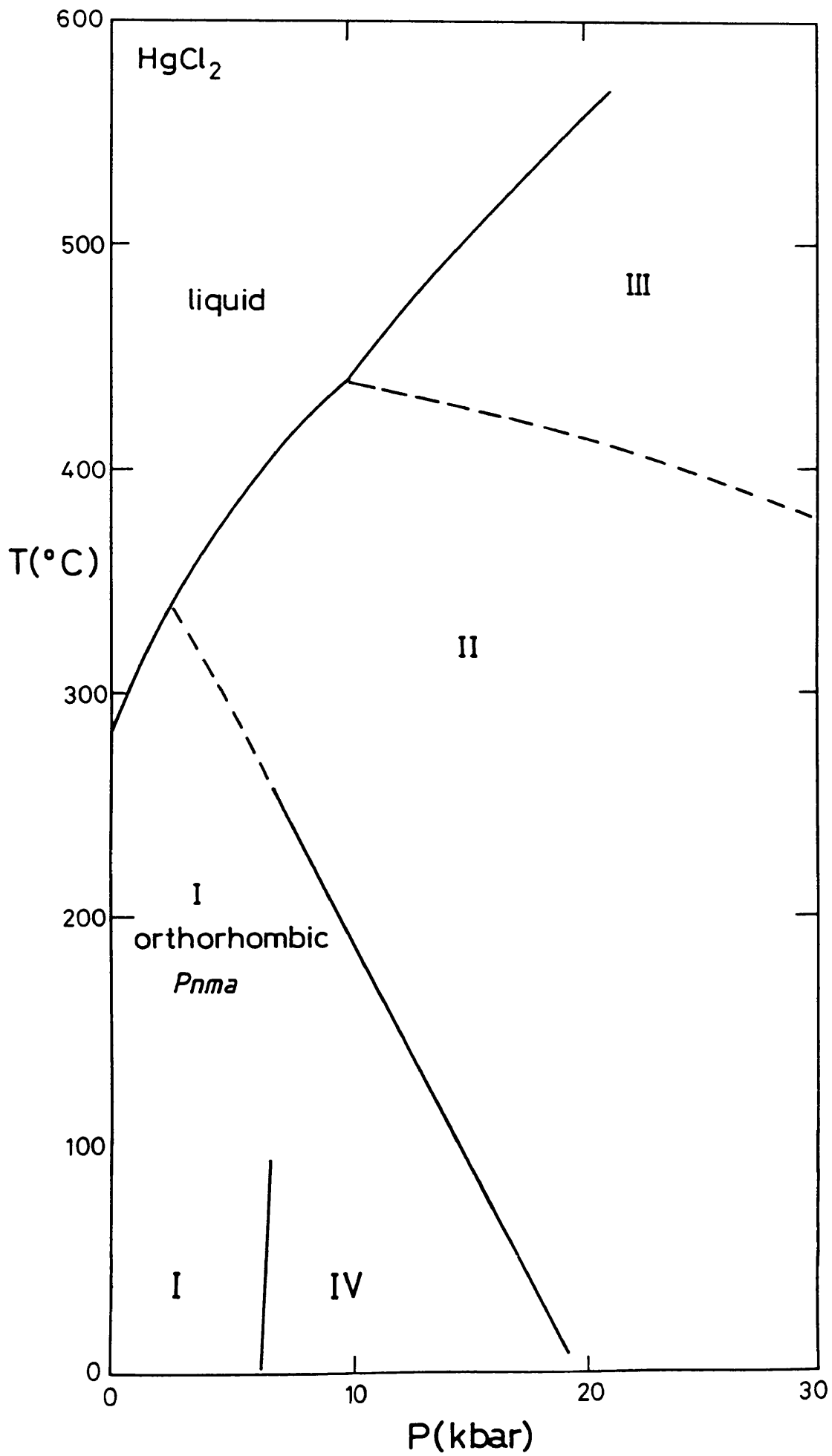
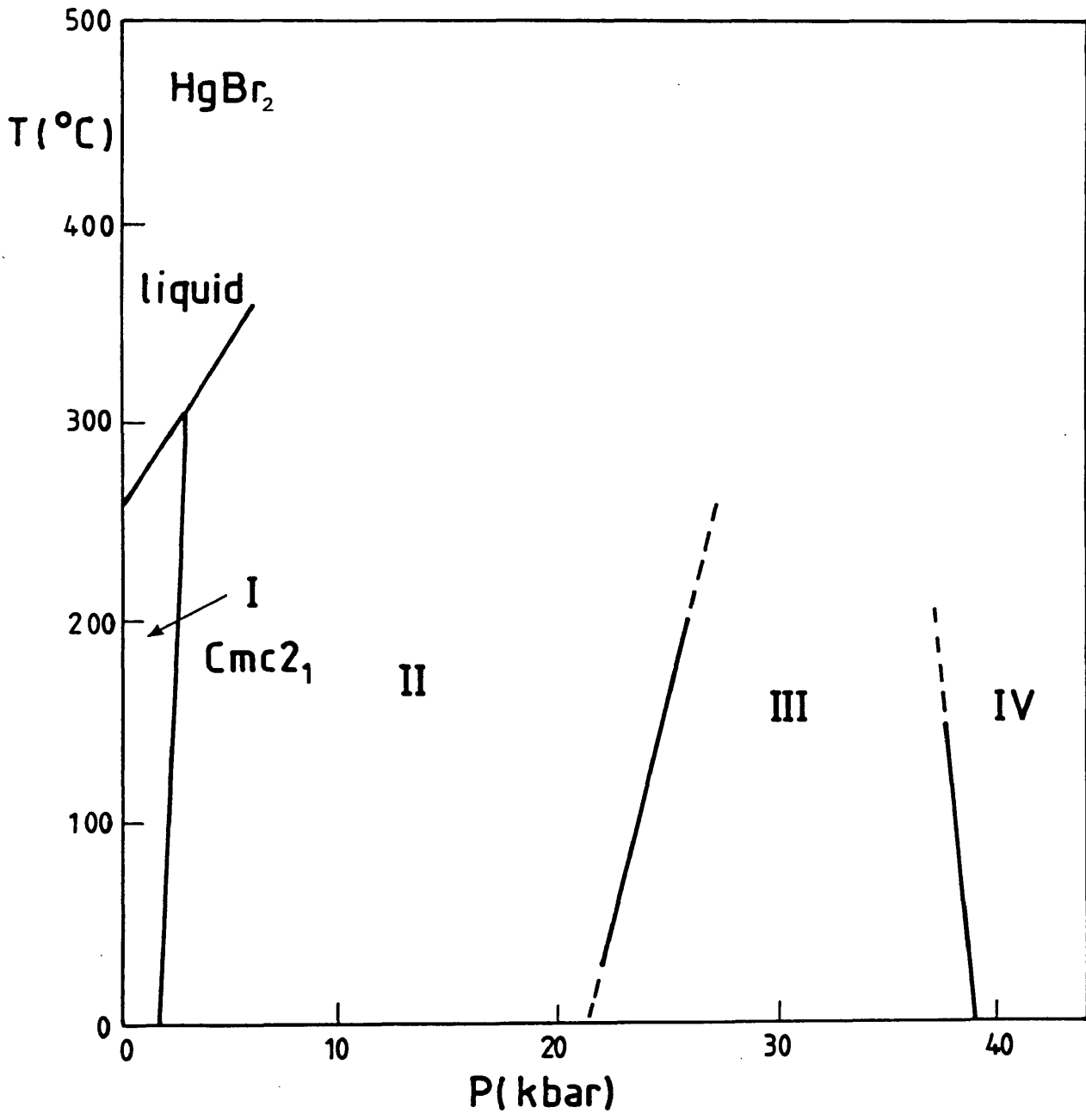


Figure 4:2

The phase diagram of HgBr_2 .



both increasing and decreasing pressures. Full details of techniques are given in Chapter 1.

4.3 Results and Discussion

4.3.1 Mercury (II) Chloride - Spectroscopic and Structural Evidence for the Phase Transitions

HgCl₂(I)

Mercury (II) chloride, under ambient conditions, crystallises in the orthorhombic group $Pnma \equiv D_{2h}^{16}$ (No. 62), with a tetramolecular primitive cell.⁵ All atoms are on $4c$ and are arranged in planar sheets stacked along b , Fig. 4:3. Electronic⁶ and vibrational⁷⁻⁹ spectra measured in the gas phase, and mass spectrometric (molecular beam) observations,¹⁰ all indicate that HgCl₂ is linear. In the most recent and accurate determination the Cl-Hg-Cl angle was found to be $178.9(5)^\circ$,¹¹ a sufficiently slight deviation from 180° for the molecule to be considered linear. There is, however, no crystallographic requirement for the two Hg-Cl distances to be equal, and indeed they are found to be nonequivalent at 2.284(12) and 2.301(14) Å.

On the basis of electrostatic arguments, this tendency of d^{10} ions, such as Hg²⁺, to form linear complexes is caused by a distortion of the spherical symmetry of the cation. Here this is due to the displacement of the nd_z^2 and $nd_z^2(n+1)s$ orbitals accompanying the transfer of two electrons from the d_z^2 to the $(1N/2)(d_z^2 - s)$ orbital. As a result a region of increased electron density is formed along the z axis.¹² However, electronic absorption and magnetic circular dichroism spectral measurements on linear dicyano complexes suggest only a slight utilisation of d orbitals with a shift towards those of the $(n+1)s$ and $(n+1)p_z$ for σ bonding.¹³

The most complete Raman data for HgCl₂ are in two single-crystal studies,^{14,15} both at ambient temperature, and shifts have been listed for a polycrystalline sample at liquid-nitrogen temperature.¹⁶ In combination with a single-crystal i.r. reflectance study¹⁷ these essentially complete the assignment of all fundamentals predicted by

Figure 4:3

Crystal structure of HgCl_2 .

Covalent radii used:

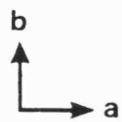
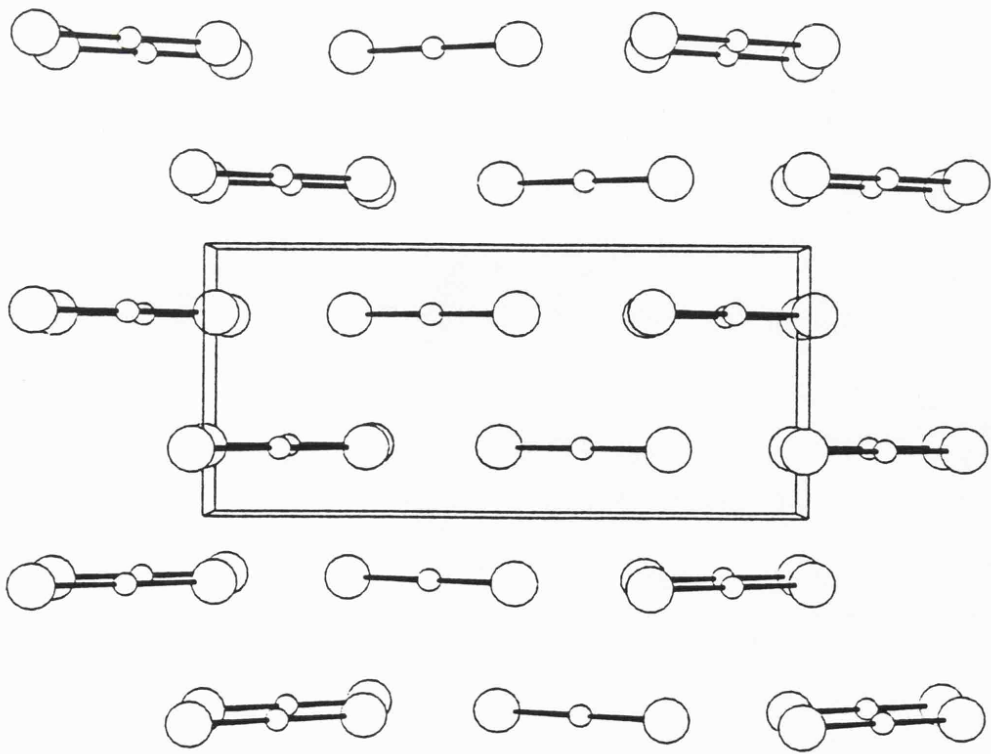
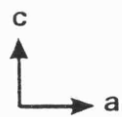
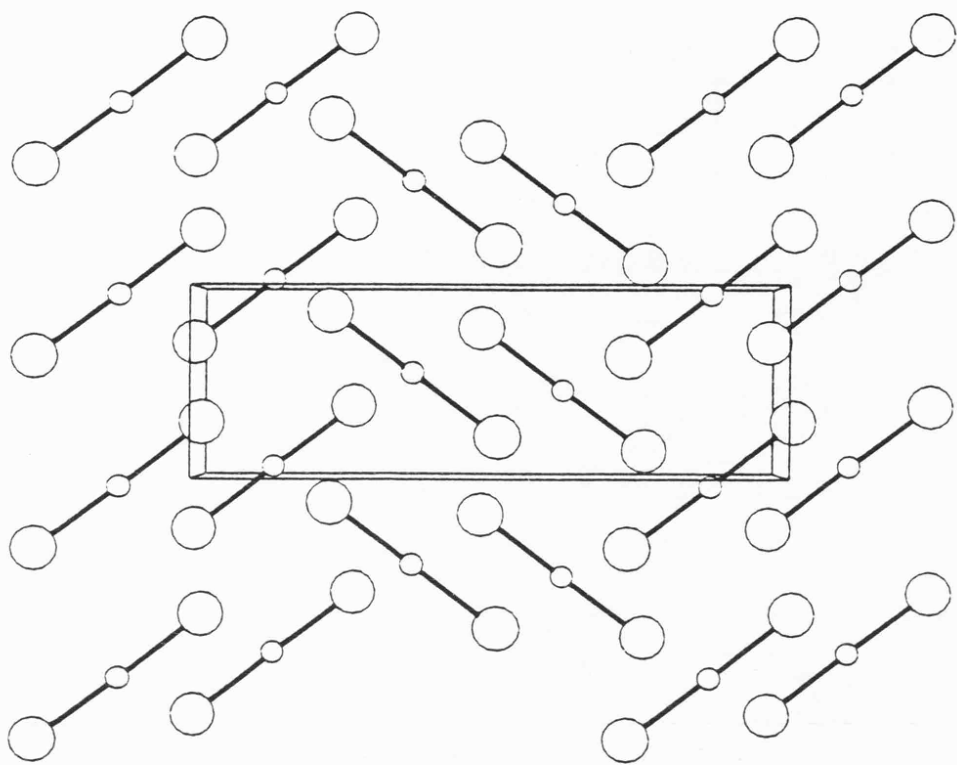
Hg (1.7)

Cl (0.99)

The atoms are shown as spheres of
relative sizes:

Hg (0.25)

Cl (0.5)



factor group analysis, Table 4:1 A.

Since the actual distortions of HgCl_2 from strict linear centrosymmetric geometry are small, a good basis for understanding the spectrum of phase I is achieved by use of the molecular point group, $D_{\infty h}$, Table 4:1 B. ν_1 , $\nu(\text{Hg-Cl})_s$, is present in the Raman spectra as an intense band at 313.6 cm^{-1} with asymmetry on the high frequency side (320.6 cm^{-1}); these are the predicted $A_g + B_{2g}$ components. In contrast, ν_3 , $\nu(\text{Hg-Cl})_{as}$, is very weak ($A_g + B_g$ components coincident) appearing at 383.1 cm^{-1} . Under $D_{\infty h}$ symmetry ν_2 , $\delta(\text{HgCl}_2)$, is i.r.-active only, and although it may attain Raman activity in the crystal by virtue of both site and correlation fields, it is expected to be intense only in the crystal i.r. spectra but weak in Raman spectra. There is no *a priori* evidence on which a distinction can be drawn between bands due to ν_2 and to libratory motion, ν_R (it is probable that they will couple strongly since the mode displacements involved are similar), however, the mode shifts with pressure do give some indication as to a possible distinction (section 4.3.5). All bands below 50 cm^{-1} are assigned to crystal translatory modes, based on the single-crystal i.r. evidence. Thus it is clear that nearly all of the bands observed in the ambient spectrum are envelopes containing two unresolved components (in parentheses):

16.2(2); 24.8(1), 26.8(1); 45.0(2);
69.8(2), 74.5(2); 120.6(2), 127.3(2) cm^{-1}

4.3.2 $\text{HgCl}_2(\text{IV})$

The I/IV transition appears to be second-order in type in that it is easily reversible, and the spectra of phase IV are very similar to those of the parent phase; certainly there is no change of cell content, Fig. 4:4. In this case $\text{HgCl}_2(\text{IV})$ must adopt a subgroup of D_{2h}^{16} . The only zellengleich subgroups of this cell are:

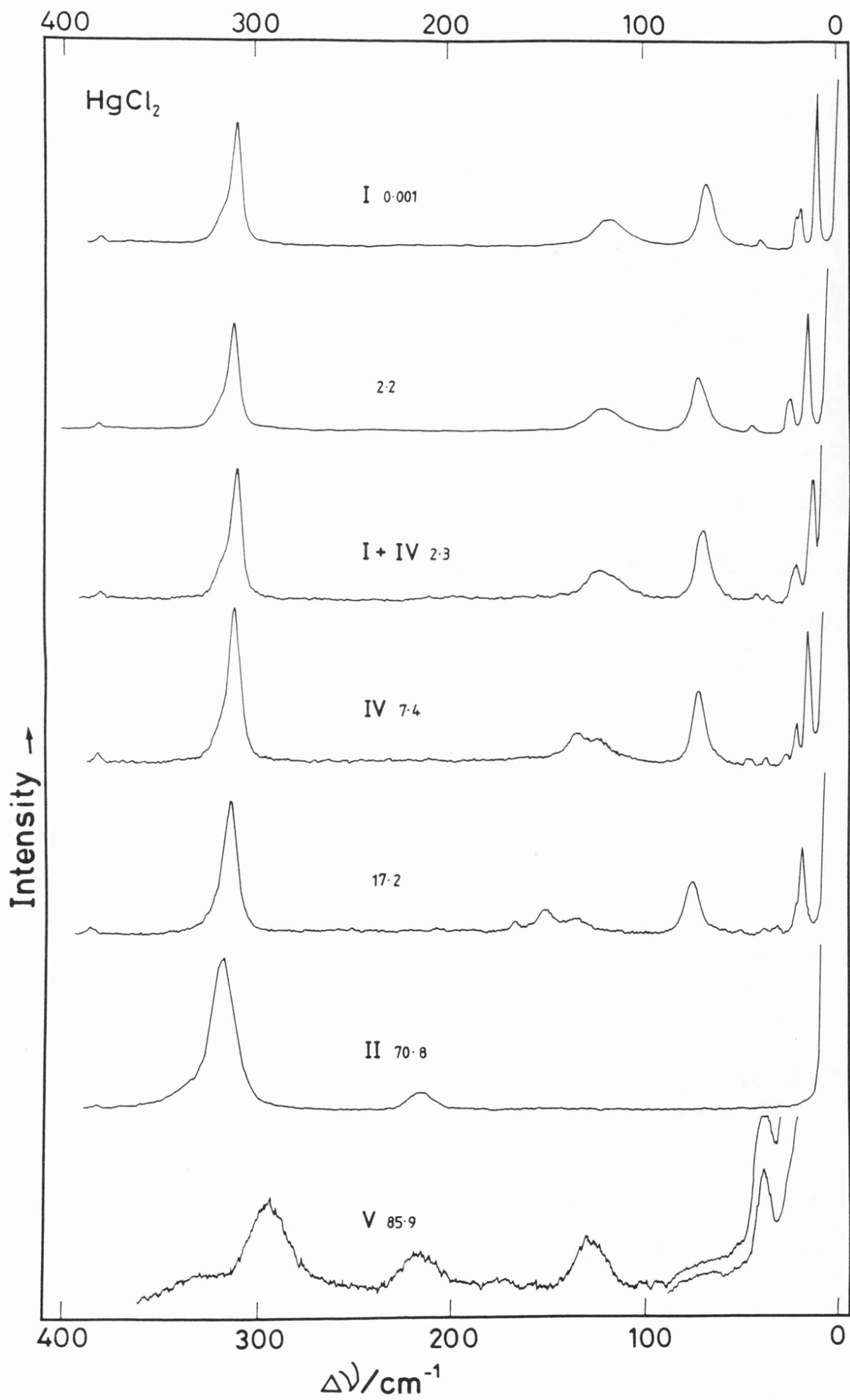
D_2^4 , C_{2h}^2 , C_{2h}^5 , C_{2v}^2 , C_{2v}^7 , and C_{2v}^9 .

Figure 4:4

Raman spectra of the internal and external modes of HgCl_2 at ambient temperature and various pressures.

Spectra were obtained using *ca.* 130 mW 514.5 nm Ar^+ radiation at the sample. Spectral slit width 0.5 cm^{-1} except at pressures > 70 kbar (1.0 cm^{-1}).

All spectra were recorded as pressure was increased in a Diacell (Dynocell for $P > 70$ kbar).



Of these D_2^4 and C_{2v}^n groups all allow Raman-i.r. breakthrough. There is no evidence for this, and neither is the Raman component of $\nu(\text{Hg-Cl})_{\text{as}}$ enhanced in intensity at the transition as would be expected in a non-centric group. It is apparent then that $\text{HgCl}_2(\text{IV})$ should adopt either the space group C_{2h}^2 or C_{2h}^5 . This is consistent with the Raman evidence in that no new bands can become Raman-active as a result of the $D_{2h} \rightarrow C_{2h}$ factor group change since the centrosymmetric property is retained. The apparent exception to this statement, the mode initially at 45.0 cm^{-1} , which shows two well-resolved components in phase IV, is accounted for by differential pressure shifting of the expected two factor group components which were unresolved in phase I. The converse behaviour is seen in the bands initially at 74.5 and 69.8 cm^{-1} , Fig. 4:5.

The Raman spectra of phase IV show few features other than the normal positive band shifts to be expected with increasing pressure. The exception to this behaviour is a slight drop in the two factor group components of ν_1 , Fig. 4:6, and in a band of translatory origin initially at 25.3 cm^{-1} . The latter shift is seen as a merging of the two lowest bands in the spectrum.

4.3.3 $\text{HgCl}_2(\text{II})$

Major changes in the Raman spectrum occur at 21.3 kbar as the transition to phase II, originally observed by Bridgman, is effected, Fig. 4:4. At room temperature the change is abrupt (only one band of translatory origin shows any residual behaviour) but becomes increasingly sluggish, showing marked hysteresis, at lower temperatures. Spectra recorded at 150 K show a biphasic equilibrium between $\text{HgCl}_2(\text{IV})$ and (II) even at 37 kbar .

In a previous Raman and i.r. high pressure study the structure of solid CO_2 ($P\alpha\beta \equiv T_h^6$) was proposed as a model which accounted for the observed spectra of $\text{HgCl}_2(\text{II})$.⁴ A factor group analysis predicts only five Raman-active species, these being associated with ν_1 , $\nu(\text{Hg-Cl})_s$, and rotatory modes. This is consistent with the great simplification of the Raman spectrum of phase II, in which ν_3 disappears and much of the lattice region is lost. The four ν_1 modes couple via S_6 site symmetry to

Figure 4:5

Plot of frequency ($\Delta\nu/\text{cm}^{-1}$) against pressure for the Raman-active modes of HgCl_2 below 80 cm^{-1} .

Solid lines were obtained by the method of least squares. Errors were estimated from the instrumental resolution and accuracy of measurement.

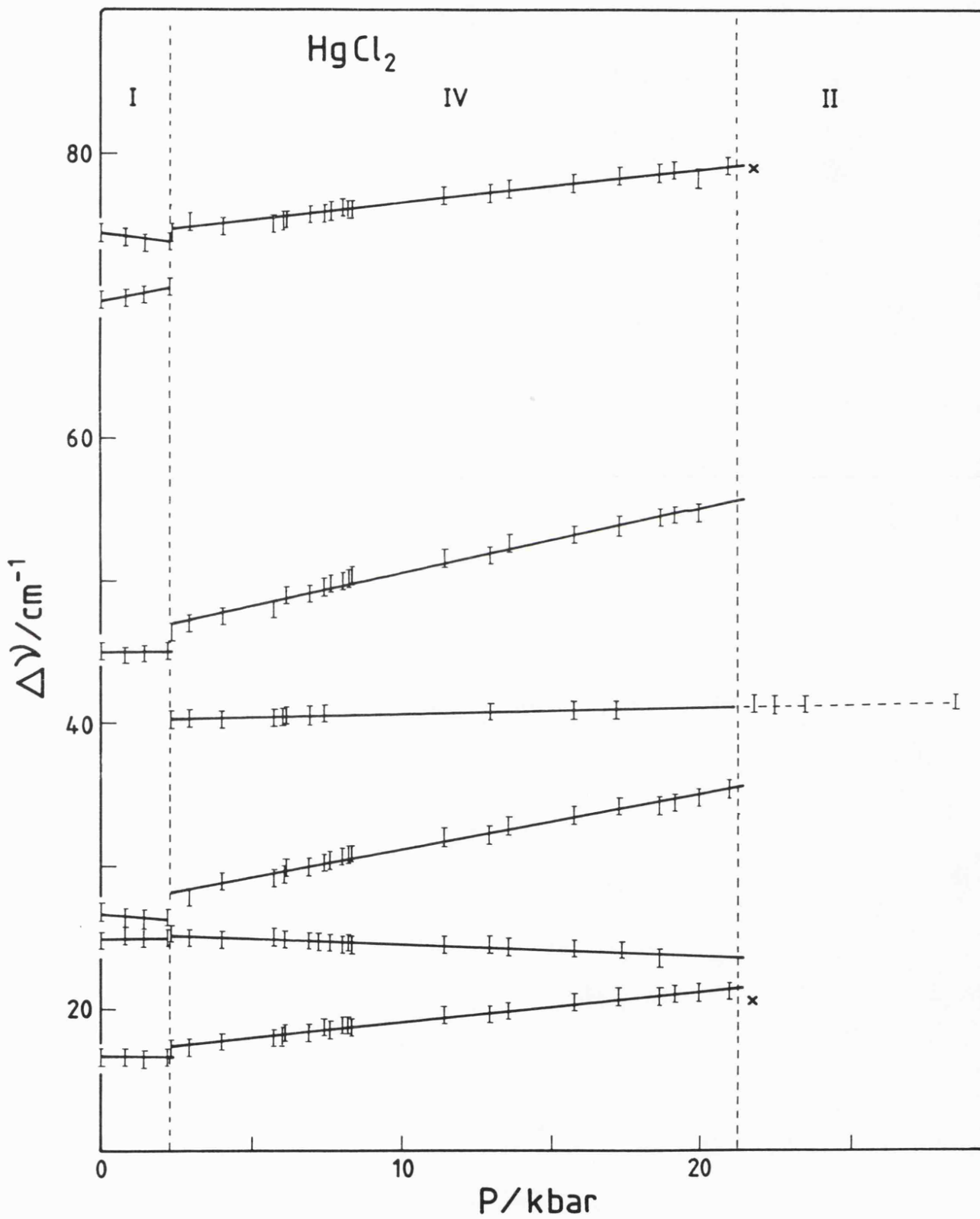
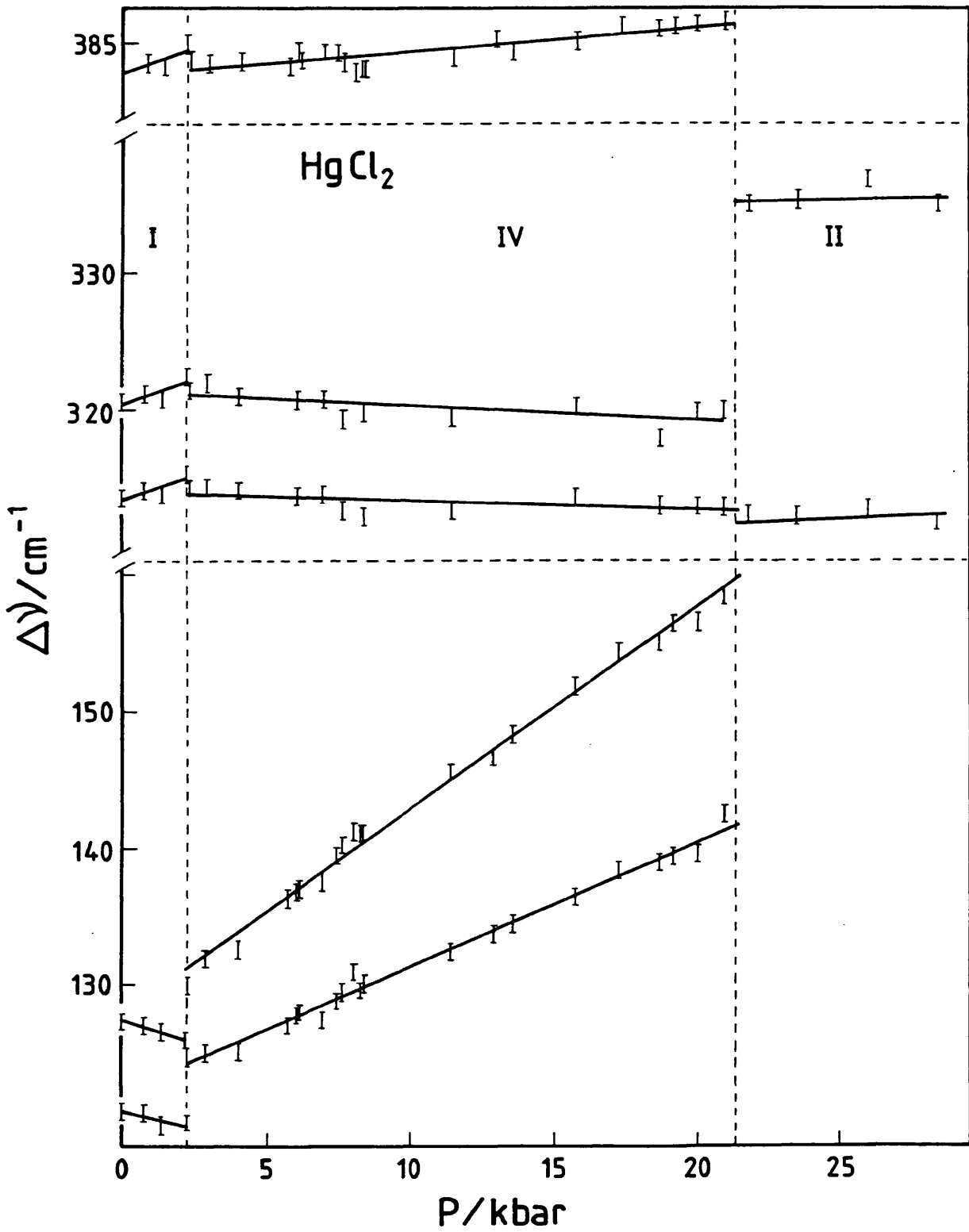


Figure 4:6

Plot of frequency ($\Delta\nu/\text{cm}^{-1}$) against pressure for the Raman-active modes of HgCl_2 above 80 cm^{-1} .

Solid lines were obtained by the method of least squares.



yield the components $A_g + T_g$ in T_h^6 . This is reflected in the intensity gain of ν_1 which is correlated with the triply degenerate T_g species, and the unresolved shoulder with A_g . It is interesting to note that the separation of the ν_1 components greatly increases from *ca.* 7 cm^{-1} in phases I and IV to *ca.* 30 cm^{-1} in phase II.

It can be shown, from methods used to calculate vibrational force fields, that the magnitudes of the experimental splittings are directly related to the intermolecular potential function (a measure of the potential energy of the unit cell).¹⁸ For each of these phases splitting of ν_1 is affected only by the site \rightarrow factor group correlation. It is clear that the large volume change accompanying the IV/II transition results in a considerably denser structure in which intermolecular interactions must inherently increase. Thus, the large separation of the ν_1 components in $\text{HgCl}_2(\text{II})$ is merely a reflection of this effect. Similarly, the almost identical splittings seen in phases I and IV underline the second order nature of that transition, in that little or no volume change is to be expected.

Whilst the spectra obtained in this study confirm previous reports, a more detailed observation of the phonon shifts has revealed a further feature of interest. On entering phase II two bands are seen at 160.9 and 170.7 cm^{-1} . With increase of pressure they shift in a manner shown in Fig. 4:7. The simplest interpretation is that the more intense lower band moves faster with change of pressure than the higher one, eventually overtaking it. Deconvolution of the spectra in the pressure range of closest approach, Fig. 4:8, does not suggest the possibility of any Fermi-resonance between them, as is indicated by lack of intensity sharing or mutual repulsion. Since only vibrational levels of the same species can perturb one another the two bands must be of different symmetry. This is compatible with the T_h^6 model for this phase in that both E_g and T_g components are expected in the region of this molecular libratory mode.

The phenomenon of Fermi-resonance is observed when two vibrational levels belonging to different vibrations (or combinations of vibrations) are, or become, accidentally degenerate. Such a resonance leads to a perturbation of the energy levels and a mixing of the eigenfunctions of the two states, with a net repulsion of the two vibrations. Most importantly this perturbation can only have a non-zero value if the

Figure 4:7

Plot of frequency ($\Delta\nu/\text{cm}^{-1}$) against pressure for the Raman-active modes in phase II of HgCl_2 .

The dashed curves represent the expected positions of the perturbed levels in the case of Fermi resonance between the two bands initially at $160\text{--}180\text{ cm}^{-1}$.

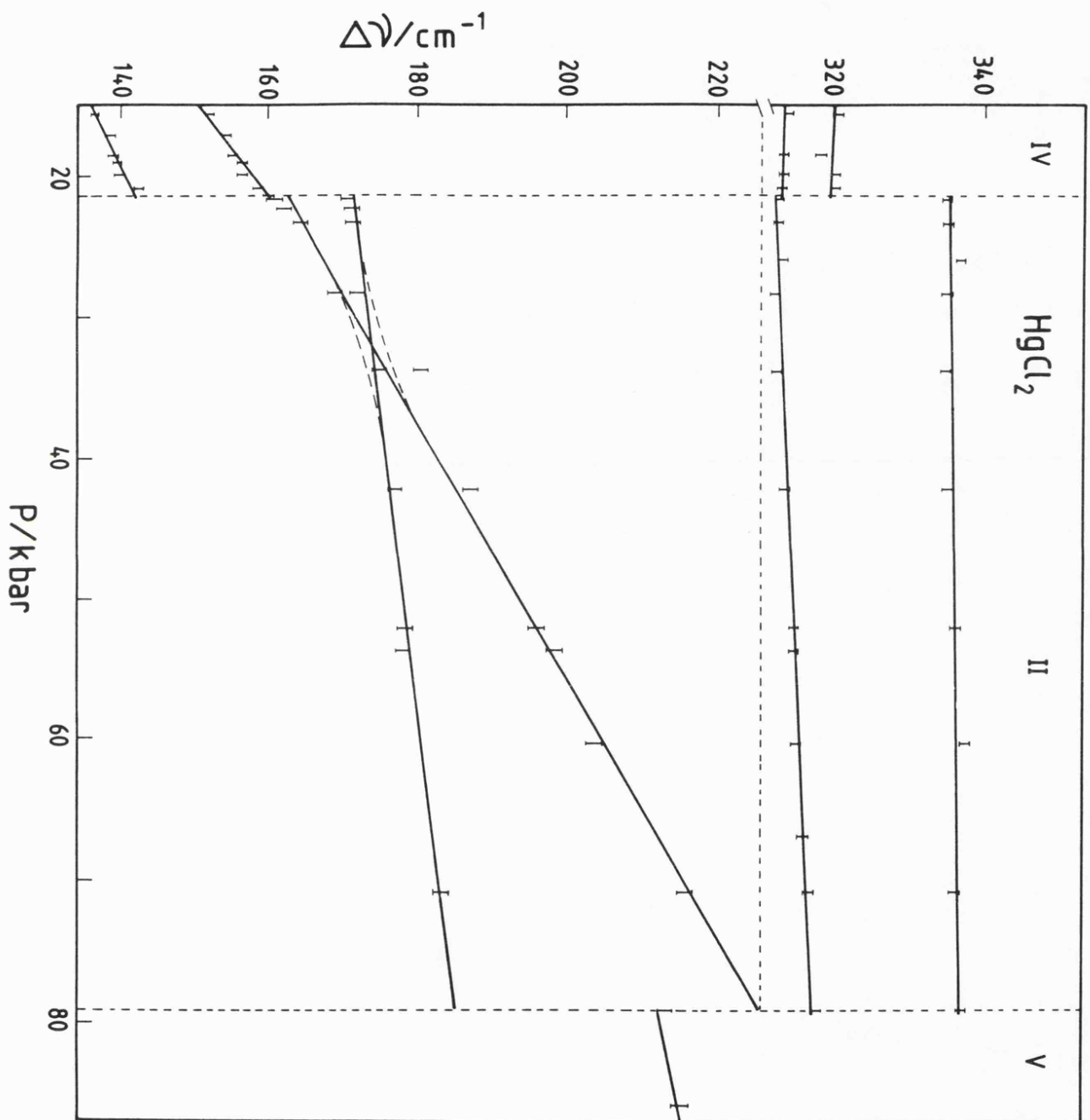
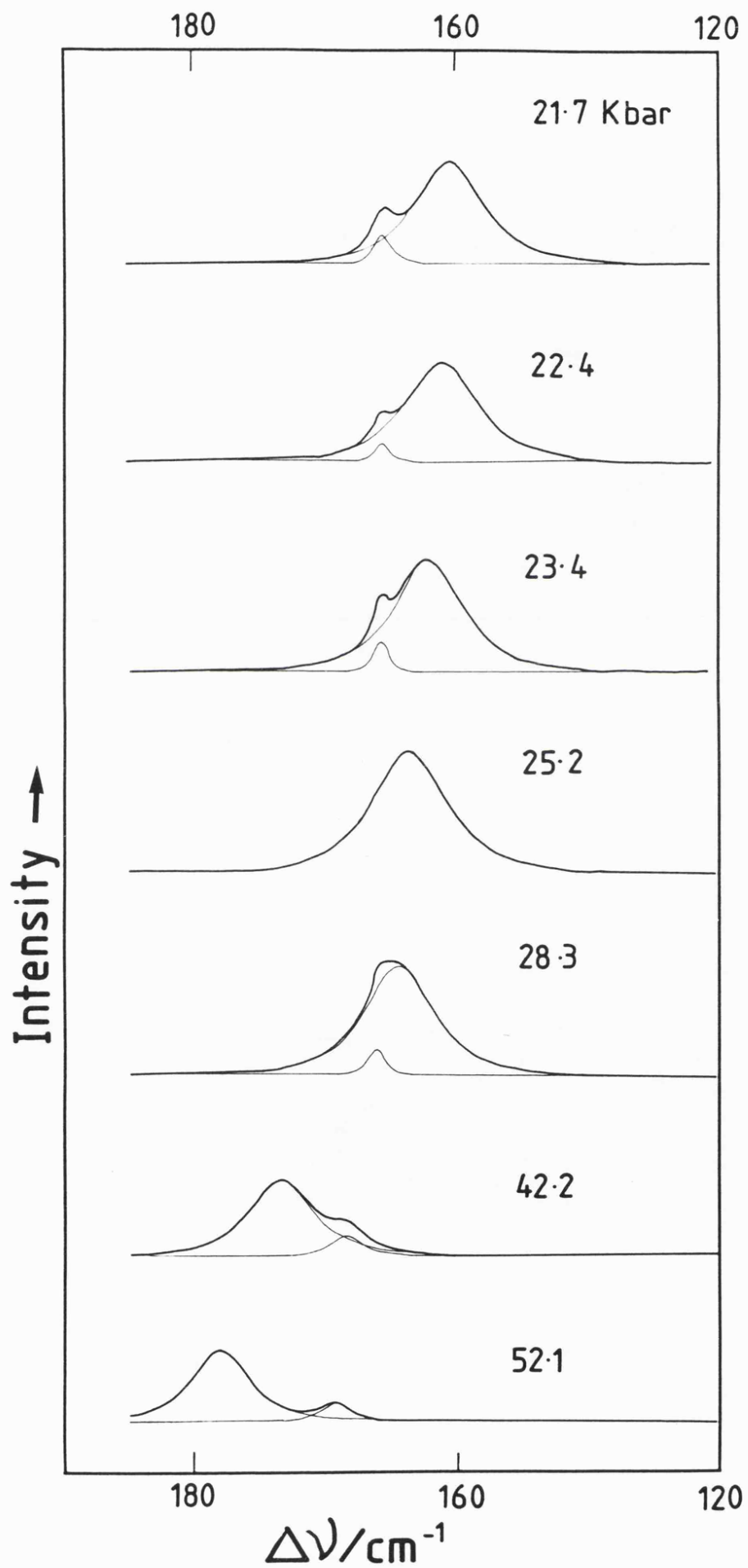


Figure 4:8

Deconvoluted Raman spectra in the region of closest approach for the libratory modes in phase II of HgCl_2 .



vibrational levels are of the same symmetry species. The observable effects, as the resonance is scanned with a variable such as temperature or pressure, are that two bands of initially unequal intensity approach closely with their intensities becoming more nearly equal, and then move apart again with their relative intensities reversed with respect to the initial condition.^{19,20}

4.3.4 HgCl₂(V)

At a pressure of 79.0 kbar there is a clear change in the Raman spectrum, indicating the transformation to a previously unobserved phase, HgCl₂(V), Figs. 4:4, 4:9. The spectra show a greater structural complexity than in HgCl₂(II), and lower symmetry, as is indicated by the reappearance of bands in the ν_2 , δ HgCl₂ and translatory regions. The symmetric stretch, ν_1 which is little affected by pressure in the preceding three phases, drops by 29 cm⁻¹ and new bands appear at *ca.* 123 and 34 cm⁻¹, the latter being particularly intense. Despite the very substantial drop in $\nu(\text{HgCl})_s$ at the phase change the spectra remain those of a molecular material.

All regions of scatter appear as relatively broad envelopes, the complexity of which it is impossible to determine meaningfully by use of deconvolution routines. Allowing for the pressure shifts throughout the series of phases, the spectra of HgCl₂(V) are reminiscent of those of phases I and IV and may well indicate readoption of a D_{2h} or C_{2h} factor group. On the Raman evidence alone it is not possible to comment further on the structural implications of this new high pressure phase.

The Raman shifts and their pressure dependencies for all phases of HgCl₂ are given in Table 4:2.

Figure 4:9

Plot of frequency ($\Delta\nu/\text{cm}^{-1}$) against pressure for the Raman-active modes in phase V of HgCl_2 .

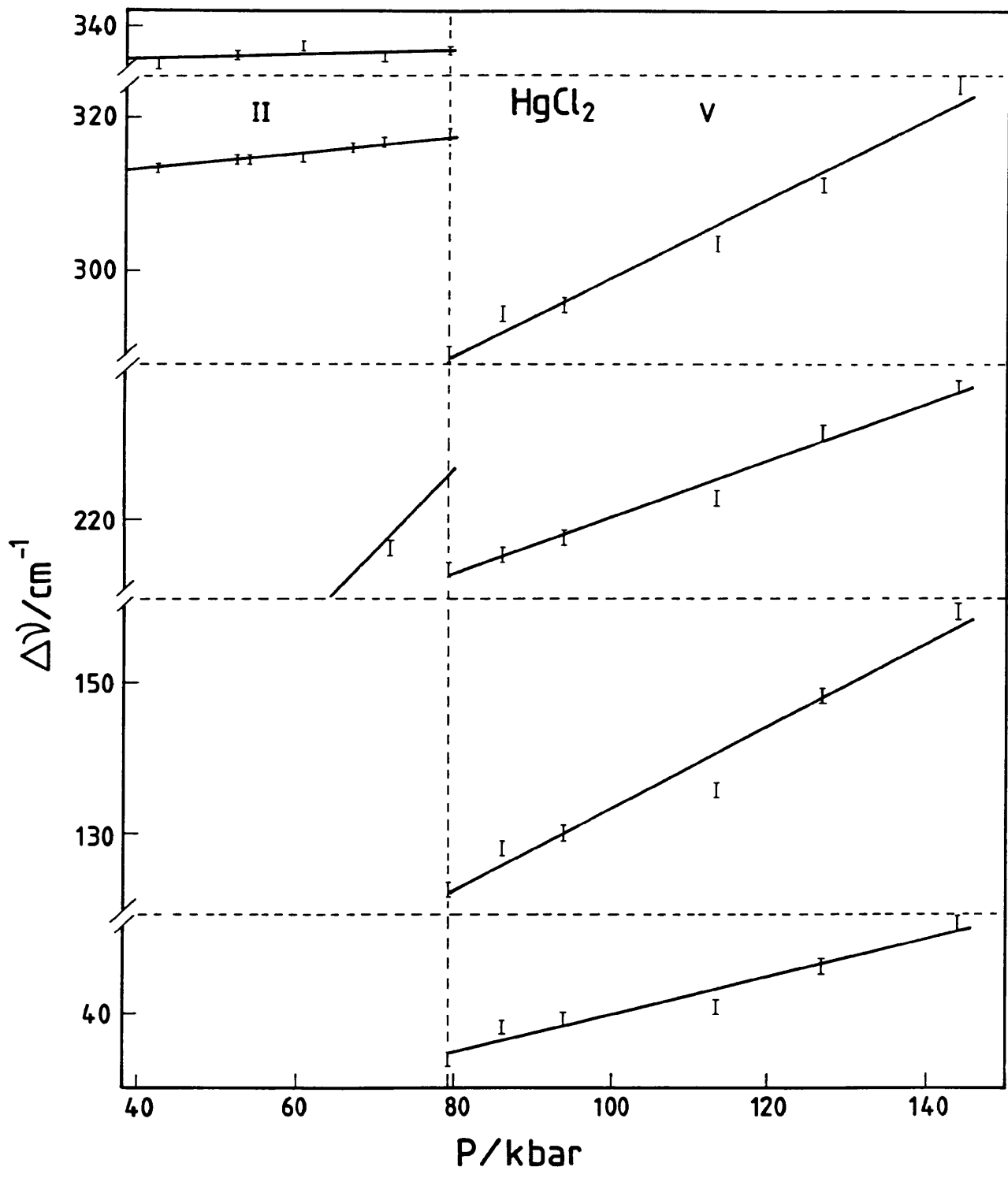


Table 4:2 Raman shifts and their pressure dependencies for HgCl₂

	$\Delta\nu$ cm ⁻¹	$\frac{d\Delta\nu}{dP}$ cm ⁻¹ kbar ⁻¹	$\Delta\nu_0$ cm ⁻¹
Phase I			
(0.8 kbar)	16.6	-0.0115	16.6
	25.2	0.0615	24.9
	26.4	-0.16	26.6
	44.7	0.0116	44.9
	70.0	0.404	69.7
	74.2	-0.3	74.4
	120.5	-0.443	120.6
	127.0	-0.65	127.4
	314.1	0.739	313.4
	321.2	0.758	320.4
	383.5	0.739	382.9
Phase IV			
(6.9 kbar)	18.3	0.219	17.4
	24.8	-0.0807	25.1
	29.9	0.38	28.4
	40.5	0.0389	40.3
	49.0	0.46	46.6
	75.7	0.231	74.7
	127.4	0.917	124.2
	137.5	1.49	131.2
	313.8	-0.0575	313.8
	320.8	-0.103	321.1
	384.4	0.175	383.0
Phase II			
(52.1 kbar)	178.4	0.245	162.1
	196.0	1.1	170.1
	314.3	0.0871	313.6
	336.0	0.0218	335.7
Phase V			
(113.4 kbar)	40.8	0.249	34.7
	135.8	0.545	122.0
	222.7	0.38	212.3
	303.0	0.52	287.8

$\Delta\nu_0$ = intercept at 1 bar or transition pressure.

4.3.5 Mechanistic Properties of the Phase Transitions

The I/IV Transition

On the basis of $\text{HgCl}_2(\text{II})$ adopting the CO_2 structure, the area of relatively weak scatter initially at *ca.* 165 cm^{-1} is solely attributable to libratory motions. This implies that the corresponding features in the spectra of phases I and IV are those seen between $100 - 160 \text{ cm}^{-1}$. Previously^{4,17} these have been designated as being primarily of ν_2 in origin (with some libratory contribution) based on gas-phase²¹ and matrix-isolation²² data which put ν_2 at *ca.* 100 cm^{-1} . This further suggested a principally rotatory character for the region at *ca.* 75 cm^{-1} , with a correspondingly minor ν_2 component. However, the present indications are that this description should be reversed. Indeed such a reversal is entirely consistent with the conclusion that $\text{HgCl}_2(\text{IV})$ adopts either of the two possible C_{2h} space groups, as discussed above.

From the mode plots for the region below 130 cm^{-1} in $\text{HgCl}_2(\text{I})$ the two bands originally at 120.6 and 127.3 cm^{-1} are clearly seen to soften up to the I/IV transition, Fig. 4:5. This indicates that these motions are becoming progressively more facile. In contrast, all bands due to translatory motions are little affected within the same range of pressure, Fig. 4:6. In $\text{HgCl}_2(\text{I})$ the sets of Wyckoff sites $4c$ (all atoms) have no geometrical restrictions on them other than that they remain in the mirror plane. Thus, the $D_{2h}^{16} \rightarrow C_{2h}^n$ ($n = 2$ or 5) transition is required to involve only rotatory and/or translatory motions about axes normal to the plane. The mode behaviour, therefore, can be interpreted as showing the transition to involve motions of a substantially rotatory nature.

4.3.6 The IV/II Transition

On entering phase IV it is again the two observable components of these libratory modes which strongly shift with pressure, in this case to higher frequencies, Fig. 4:5. The table below relates the sites $4c$ in D_{2h}^{16} (phase I) with their corresponding sites in two of the six possible subgroups of the parent space group. Thus, in the two suggested C_{2h}^n

groups ($n = 2$ and 5) $4c$ maps onto sites $2e$ and e respectively. However, the site point symmetries are no longer required to be the same *viz.*,

Space Group	Wycoff Site	Point Symmetry
D_{2h}^{16}	$4c$	m
C_{2h}^2	$2e$	m
C_{2h}^5	e	1

Since the structural change from phase I to phase II (CO_2 type) requires rotation of the molecules out of the mirror plane it would be reasonable to expect an initial degree of such movement within $HgCl_2(IV)$, thus facilitating the actual transition ($IV \rightarrow II$). For this to happen there must be no restrictions placed on these rotational motions by virtue of the site symmetry. Accordingly, only the e site of C_1 symmetry in C_{2h}^5 will allow this. Therefore, C_{2h}^5 is the most probable choice of space group for the structure of $HgCl_2(IV)$, based on the present Raman evidence.

4.3.7 Mercury (II) Bromide - Spectroscopic and Structural Evidence for the Phase Transitions.

$HgBr_2(I)$

The ambient phase of mercury (II) bromide crystallises with the symmetry of the orthorhombic space group $Cmc2_1 \equiv C_{2v}^{12}$ (No. 36), with a bimolecular primitive cell (all atoms on $2a$).⁵, Fig. 4:10. It has a layer structure (stacked along a) which is related to that of the cadmium dihalides but differs from it in that two colinear Hg-Br bonds are much shorter (2.48 Å) than the other four (3.23 Å) which complete a tetragonally distorted octahedron. The s.t.p. structure of $HgBr_2(I)$ is denser and quite different from that of $HgCl_2(I)$. Each is composed of similar layers of linear molecules but the stacking sequence is different.

Although $HgBr_2$ has been studied often using Raman and i.r. spectroscopy there are still no single-crystal Raman data

Figure 4:10

Crystal structure of HgBr_2 .

Covalent radii used:

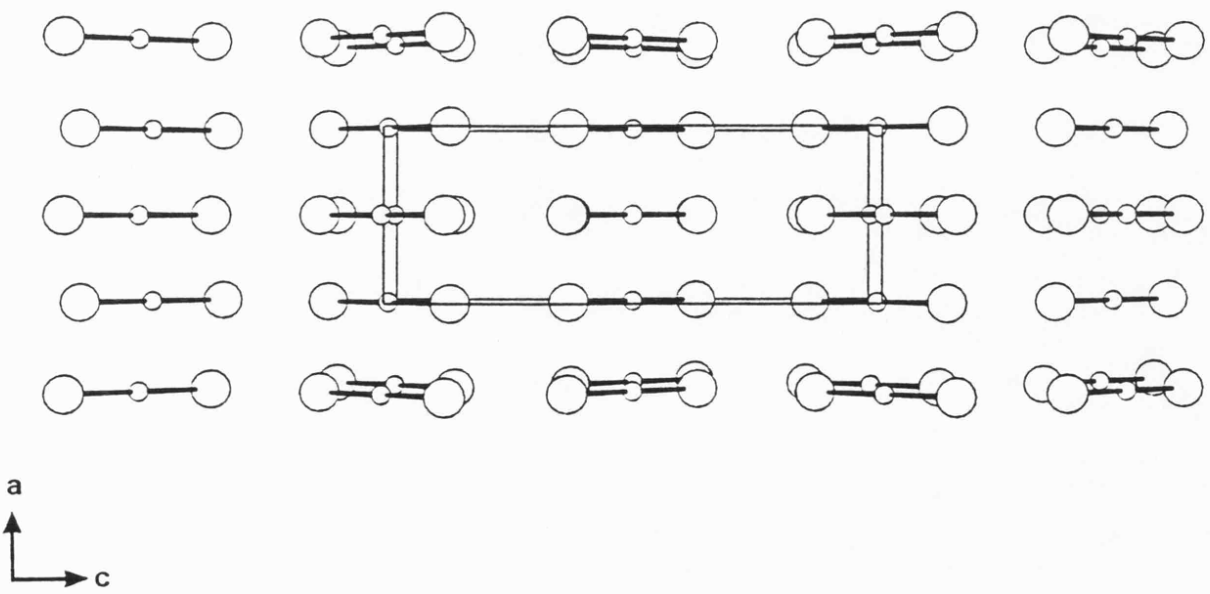
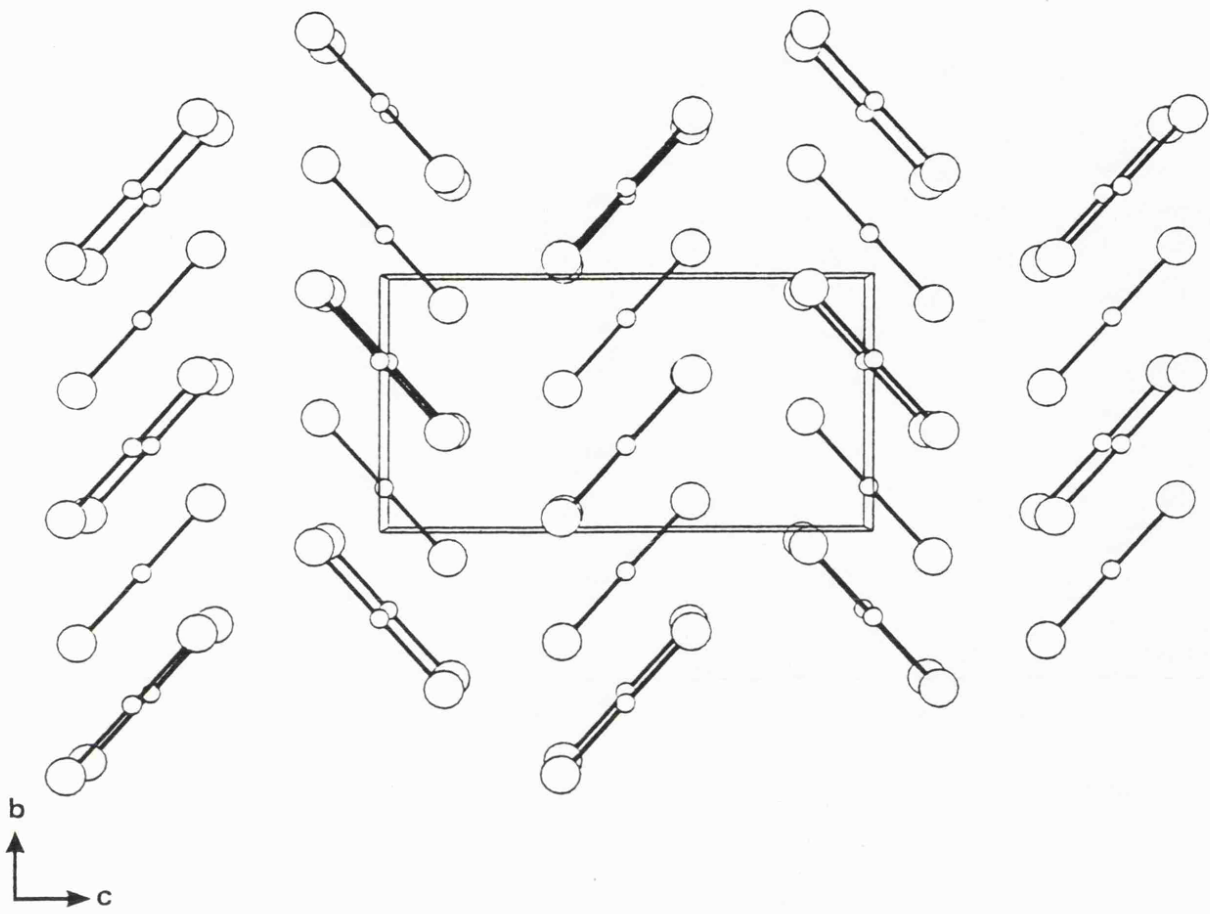
Hg (1.7)

Br (1.21)

The atoms are shown as spheres of
relative sizes:

Hg (0.25)

Br (0.5)



available.^{16,23,24} The most complete vibrational assignment is in a single-crystal i.r. reflectance study in which all fundamentals predicted by factor group analysis have been accounted for,¹⁷ Fig. 4:11, Table 4:3 A. However, the assignment of the Raman spectra of polycrystalline samples, even at low temperature, remain somewhat incomplete. Despite the crystal selection rules, which require coincident i.r. and Raman spectra (apart from the A_2 species), the Raman spectra are much simpler than is expected.

At room temperature the Raman spectrum is dominated by two intense bands at 186.5 [ν_1 , $\nu(\text{Hg-Br})_s$] and 57.1 cm^{-1} . Both split (186.2, 183.5 and 61.0, 59.5 cm^{-1}) at low temperature. The former are the two required components, $A_1 + B_2$, of ν_1 , the latter are attributed to ν_2 and libratory contributions. Of the remaining scatter only two much weaker bands at 17.2 and 14.2 cm^{-1} , of translatory origin, are clearly resolved in normal spectra. Under forcing conditions ν_3 is visible as an area of extremely weak scatter at ca. 220 (B_2) and 250 (A_1) cm^{-1} , and several external modes appear in a region between 30 and 50 cm^{-1} .

In the spectra of phase I all Raman features, excluding ν_3 , can be followed at high pressure and, with the exception of a lattice mode at 46.7 cm^{-1} , a slight softening is observed for all bands, Fig. 4:13. The two sharp translatory modes at the very low frequency end of the spectrum broaden and decrease in intensity, whilst the band at 36.6 cm^{-1} is more clearly resolved as it shifts from under the wing of the intense $\nu_2(\text{R})$.

4.3.8 HgBr₂(II)

At ca. 4.0 kbar marked variations in the Raman spectra and mode plots indicate the onset of the transition to HgBr₂(II), contrary to previous reports in which little change was observed,⁴ Figs. 4:12,13,14. The most significant changes are the appearance of three clear components of ν_1 (197.7, 189.8, 184.8 cm^{-1}) and an increased complexity in the lattice mode region. As phase II is established the overall intensities of the external modes drop relative to ν_1 , which retains an intense central component, Fig. 4:15. This and the remaining bands due to $\nu(\text{Hg-Br})_s$ soften to some extent up to the II/III transition, all

Figure 4:11

Approximate representation of the
eighteen fundamental vibrations of
 HgBr_2 .

$$\text{HgBr}_2 \quad \Gamma_{\text{total}} = 6A_1 + 3A_2 + 3B_1 + 6B_2$$

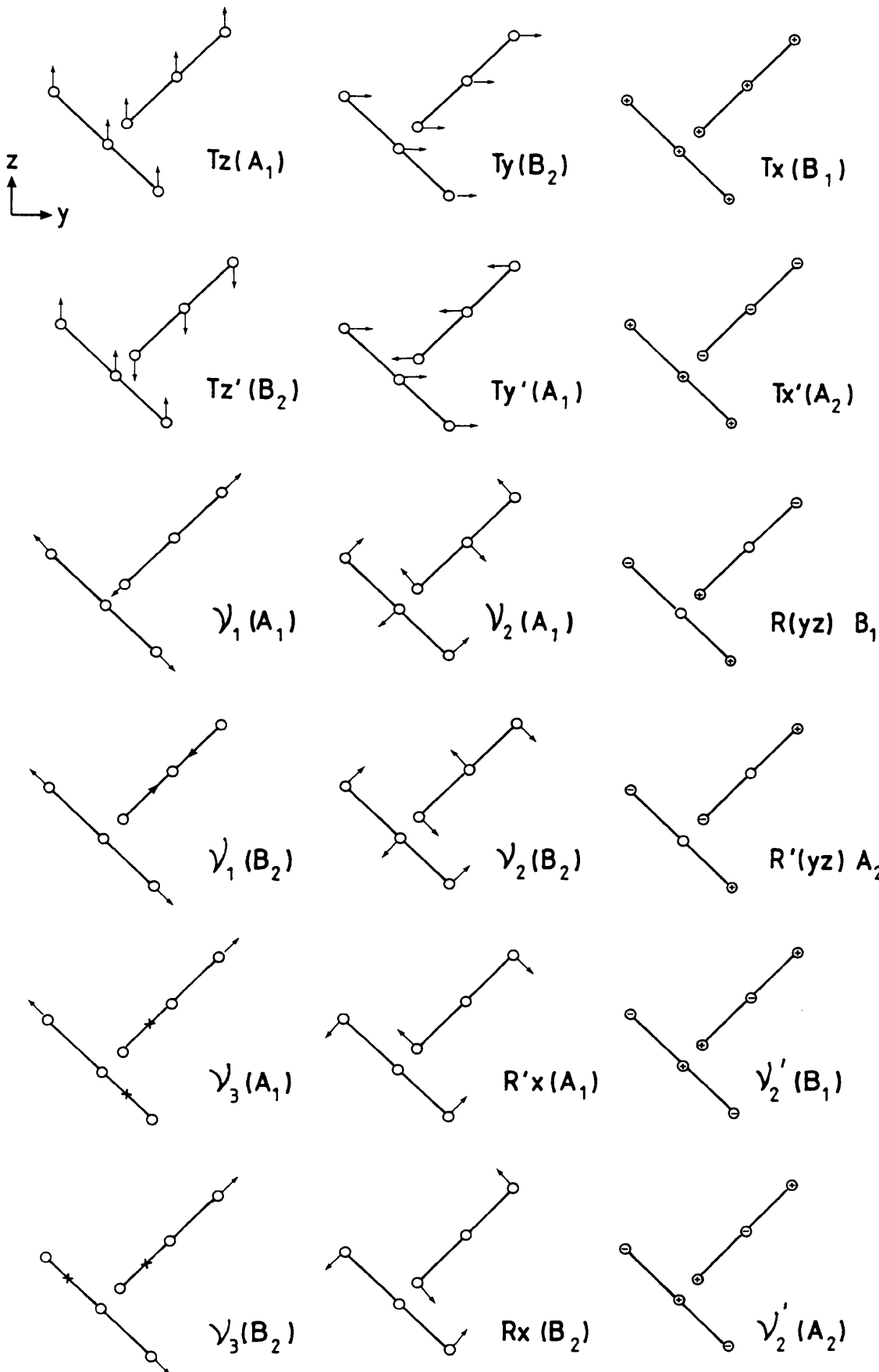
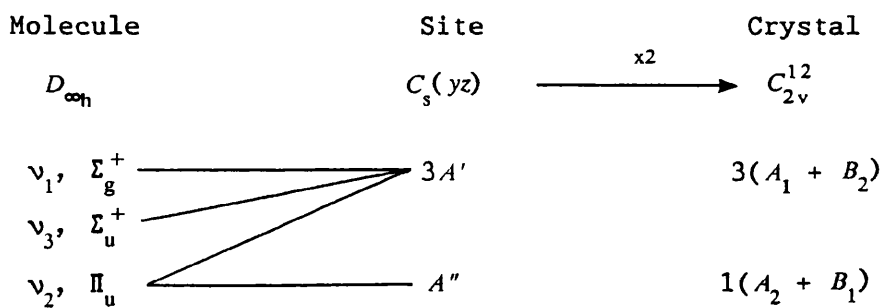


Table 4:3 A. Factor group analysis for HgBr_2

C_{2v}		A_1	A_2	B_1	B_2
Hg	$2a$	2	1	1	2
Br	$2a$	4	2	2	4
N_T^a		6	3	3	6
T_A		1		1	1
T		1	1		1
R_{yz}		1	1	1	1
Γ_{vib}		3	1	1	3
Activity ^b		Ir/R	R	Ir/R	Ir/R

B. Correlation scheme



a,b See Table 4:1

Figure 4:12

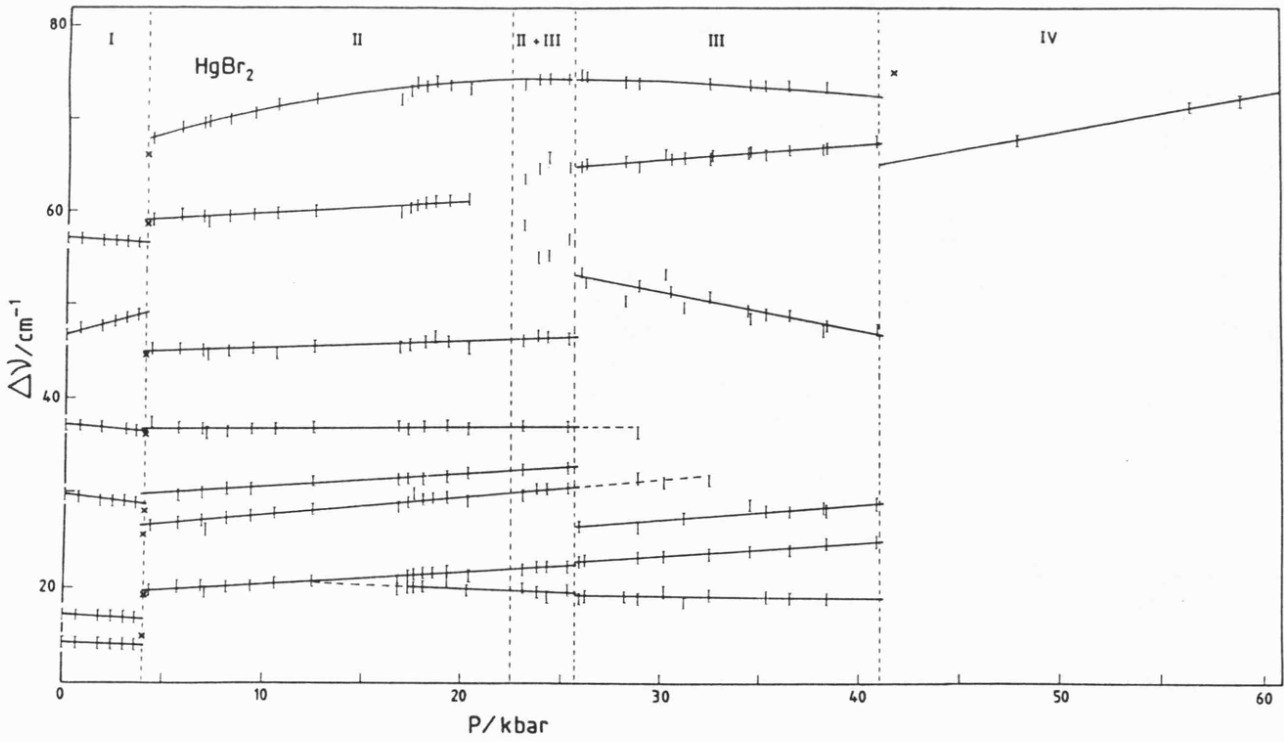
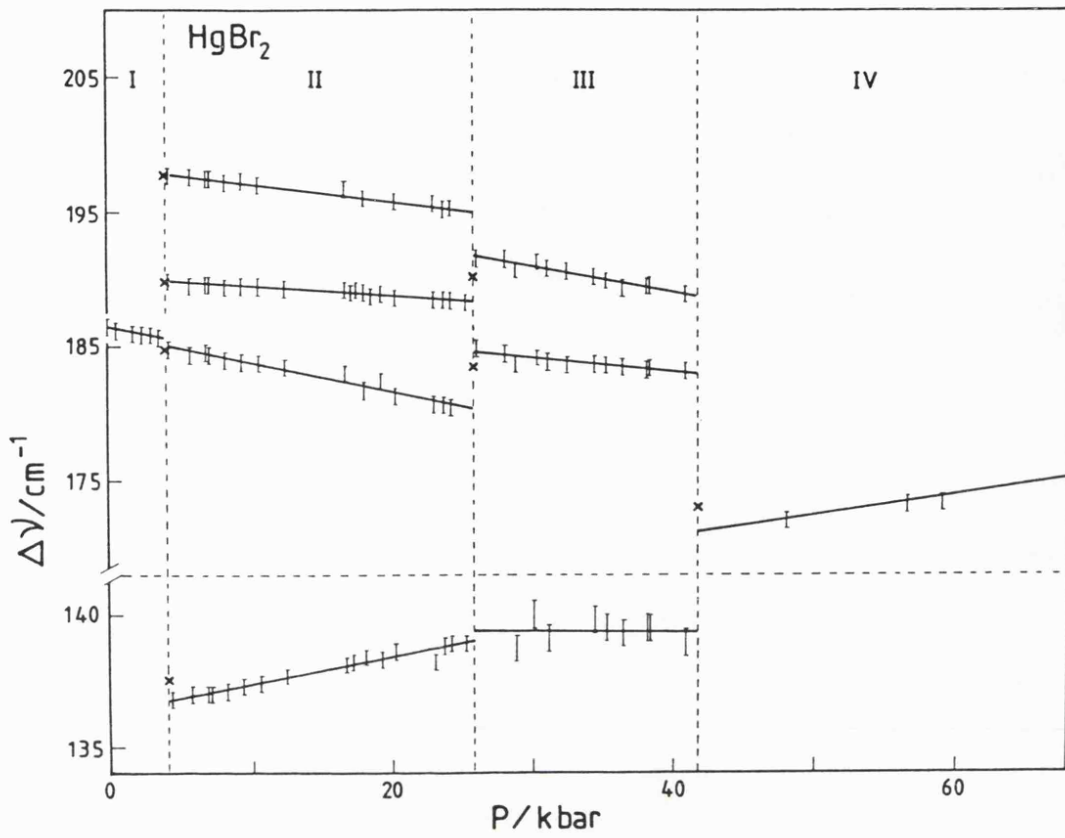
Plot of frequency ($\Delta\nu/\text{cm}^{-1}$) against pressure for the Raman-active modes of HgBr_2 above 80 cm^{-1} .

Solid lines were obtained by the method of least squares.

Figure 4:13

Plot of frequency ($\Delta\nu/\text{cm}^{-1}$) against pressure for the Raman-active modes of HgBr_2 below 80 cm^{-1} .

Solid lines were obtained by the method of least squares.



other modes showing small positive shifts with pressure. A translatory envelope initially at 19.7 cm^{-1} is resolved into two components by *ca.* 17 kbar as a result of differential shifting, however, the behaviour throughout phase II is generally unremarkable.

4.3.9 HgBr₂(III)

The transition to phase III is known to be sluggish at ambient temperature. This is seen in the lattice region of spectra over the 6 kbar range between 23.0 and 29.0 kbar, in which biphasic behaviour is particularly apparent, Fig. 4:14. In contrast the change in ν_1 at 26.0 kbar, to a doublet with a substantial intensity increase, is quite sudden. This is further reflected in the mode plots in which only the region $50 - 65 \text{ cm}^{-1}$ shows any sign of mixed behaviour in the transition region (it would be informative to obtain a greater density of data between 20 and 30 kbar), Fig. 4:13.

As in phases I and II the components of ν_1 show a negative pressure dependence. The higher frequency band at 191 cm^{-1} merges with and loses some intensity relative to that at 185 cm^{-1} , their separation remaining of a similar magnitude to that found in HgBr₂(II). The lattice spectra of phase III show some simplification compared with those of phase II. Three bands between 45 and 75 cm^{-1} , in particular one at *ca.* 50 cm^{-1} , are the most intense features, with some much weaker scatter below this ($18-30 \text{ cm}^{-1}$). On increasing pressure the most intense mode initially at 53.4 cm^{-1} shows a marked softening of some 6 cm^{-1} , accompanied by a slight intensity decrease relative to ν_1 . The remaining external modes weaken significantly within the 15 kbar stability field of this phase and by 40 kbar ν_1 appears as a broad slightly asymmetric singlet.

4.3.10 HgBr₂(IV)

At 41.0 kbar a dramatic simplification in the Raman spectrum marks the transition to a new phase, HgBr₂(IV), Fig. 4:14. ν_1 shows a substantial drop of *ca.* 15 cm^{-1} but remains broad and intense with some slight high frequency asymmetry. The remaining feature in the spectra of phase IV is a much weaker but equally broad band at *ca.* 70 cm^{-1} . Both

Figure 4:14

Raman spectra of the internal and external modes of HgBr_2 at ambient temperature and various pressures.

Spectra were obtained using *ca.* 130 mW 514.5 nm Ar^+ radiation at the sample. Spectral slit width 0.5 cm^{-1} except at pressures > 50 kbar (1.0 - 1.5 cm^{-1}).

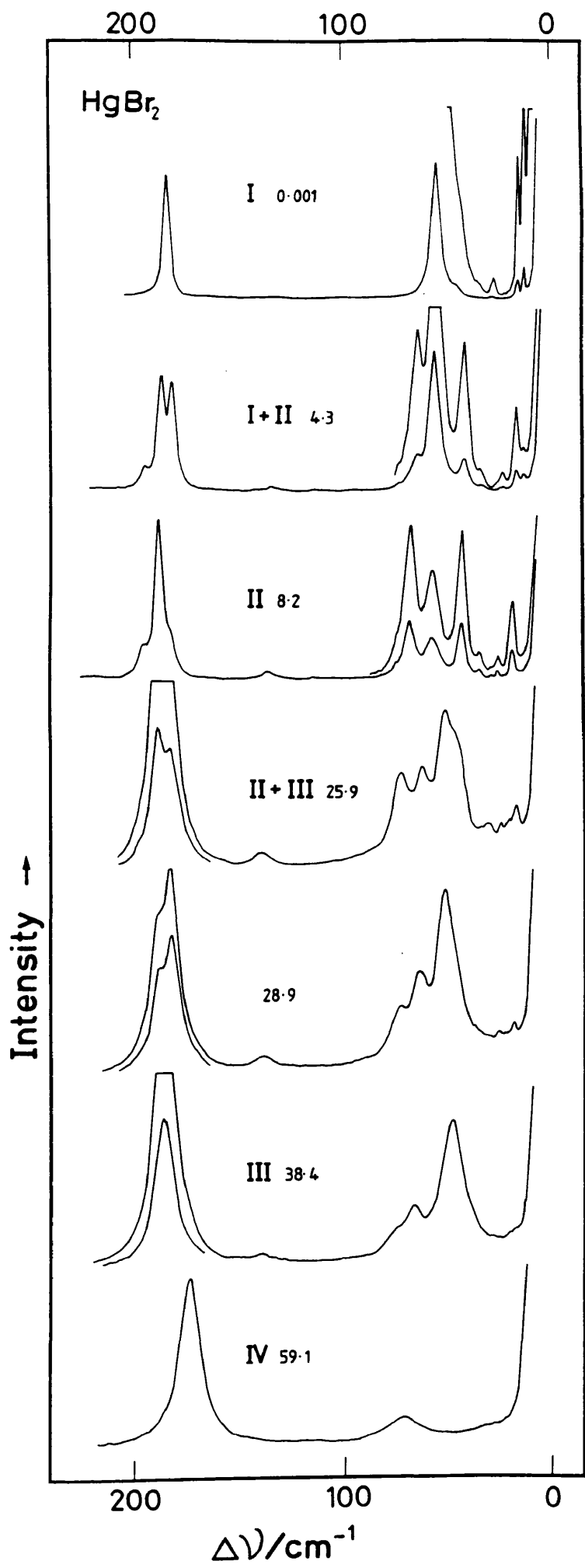
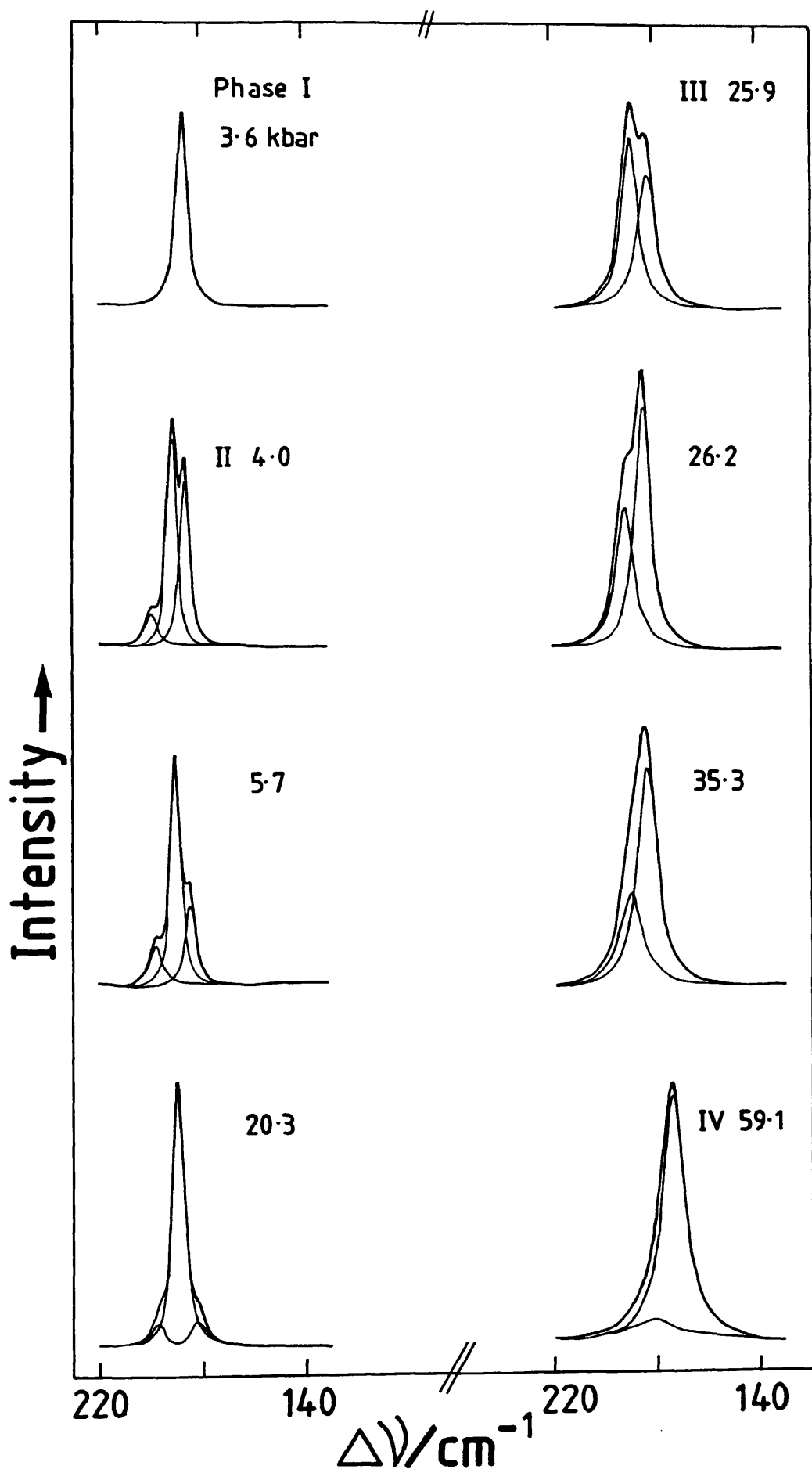


Figure 4:15

Deconvoluted Raman spectra showing the development of ν_1 , $\nu(\text{Hg-Br})_s$, in each of the four phases of HgBr_2 .



harden with pressure, ν_1 for the first time in any of the four phases. This phase remains stable up to at least 100 kbar, the limit of current observations.

The Raman shifts and their pressure dependencies for all phases of HgBr_2 are given in Table 4:4.

4.3.11 Structural Conclusions

The spectra of phases I, II and III are clearly those of a molecular system. The transition I \rightarrow II is typically first order in character which, coupled with the lack of any structural data for this phase, restricts deductions to the spectral evidence alone. Appearance of three clear components of ν_1 in $\text{HgBr}_2(\text{II})$ requires that the primitive unit cell has been doubled at the transition *i.e.* from two to four, a view supported by the increased complexity of the lattice mode spectrum. The tetramolecular cell must also be non-centric for there to be more than two Raman-active bands in this region. This is because in a centric factor group the four coupled motions of any vibrational component would result in two *gerade* and two *ungerade* modes, of which only those of *g* parity can be Raman-active (a case in point is seen in the correlation scheme for $\text{HgCl}_2(\text{I})$, Table 4:1 A).

The spectra of phase III show some simplification compared with those of phase II, but do not give the appearance of cell halving at the transition. It is suggested, therefore, that the non-centric phase II cell has become centric but without change of contents. A transition to a monoclinic cell with factor group C_{2h} is compatible with the Raman evidence, since, as was the case for HgCl_2 , the only major change possible is the removal of the mirror planes.

As $\text{HgBr}_2(\text{I})$ is reasonably regarded as a distorted variant of the CdX_2 layer structure types, it is not unlikely that at some high pressure HgBr_2 will eventually assume the CdI_2 structure ($P3m1 \equiv D_{3d}^3$, No. 164) or some polytype thereof. Indeed the spectra of $\text{HgBr}_2(\text{IV})$ are strongly reminiscent of those yielded by materials with the CdI_2 structure. The selection rules give a representation; $A_g + E_g + A_{2u} + E_u$, of which only *g* modes are Raman-active. A high symmetry environment

Table 4:4 Raman shifts and their pressure dependencies for HgBr₂

	$\Delta\nu$ cm ⁻¹	$\frac{d\Delta\nu}{dP}$ cm ⁻¹ kbar ⁻¹	$\Delta\nu_0$ cm ⁻¹
Phase I			
(1.8 kbar)	14.1	-0.0563	14.2
	17.1	-0.102	17.2
	29.1	-0.233	29.6
	47.6	0.56	46.8
	56.8	-0.134	57.1
	186.0	-0.1981	186.4
Phase II			
(18.1 kbar)	20.2	-0.0722	19.6
	21.6	0.126	21.1
	29.3	0.194	26.3
	31.4	0.145	29.6
	37.0	0.0149	36.7
	46.0	0.0743	44.8
	60.9	0.121	59.0
	73.5	0.287	68.9
	138.4	0.101	136.8
	181.7	-0.215	185.1
	189.0	-0.065	189.8
	196.0	-0.123	197.8
Phase III			
(36.5 kbar)	19.1	-0.0004	19.1
	24.1	0.144	22.8
	28.1	0.174	26.4
	49.0	-0.401	53.1
	66.5	0.164	64.7
	73.5	-0.0922	74.4
	139.3	-0.0008	139.4
	183.5	-0.097	184.6
	189.3	-0.188	191.7
Phase IV			
(56.6 kbar)	71.4	0.386	65.2
	173.3	0.159	171.0

$\Delta\nu_0$ = intercept at 1 bar or transition pressure.

is implied by the profound simplification of the Raman spectra on leaving phase III, whilst the drop in $\nu(\text{Hg-Br})_s$ is also indicative of a much greater degree of intermolecular bonding (in the CdI_2 type layer all Hg-Br bonds are required to be equal).

4.4 Structural Comparisons: HgCl_2 and HgBr_2

The phase I structures of HgCl_2 and HgBr_2 are quite dissimilar, *vide supra*. Since even the most reconstructive of phase transitions are remarkably economical in atom relative movements, it seems unlikely that there should be any structural equivalences in the series of four polymorphic phases exhibited by each of the two materials. However, there are points of common behaviour:

(i) Upon entering $\text{HgCl}_2(\text{V})$ at 79.0 kbar, and $\text{HgBr}_2(\text{IV})$ at 41.0 kbar, there is a significant drop in $\nu(\text{Hg-X})_s$, ($X = \text{Cl}$, 29.0 cm^{-1} ; $X = \text{Br}$, 15.0 cm^{-1}), implying increased intermolecular bonding although apparently stopping short of a semi-covalently bonded lattice type.

(ii) The spectra of $\text{HgCl}_2(\text{II})$ and $\text{HgBr}_2(\text{IV})$ are also compatible with their having the same structure. Nevertheless, these points are regarded as readily accommodated within the structural sequences already indicated for the individual compounds. Thus, both $\text{HgCl}_2(\text{II})$ (CO_2 type) and $\text{HgBr}_2(\text{IV})$ (CdI_2 type) are consistent with the similar spectra found for them. Moreover, if $\text{HgBr}_2(\text{IV})$ had the CO_2 type structure, by analogy with $\text{HgCl}_2(\text{II})$ it would be expected to transform again at a pressure below that of the $\text{HgCl}_2(\text{II/IV})$ change, but it does not.

4.5 Summary

The Raman spectra of mercury (II) chloride and bromide have been studied to *ca.* 150 and 100 kbar respectively. For the chloride phase transitions were found at 2.2, 21.3 and 79.0 kbar, the latter marking the first order change to a previously unobserved phase, $\text{HgCl}_2(\text{V})$. Detailed phonon pressure dependencies have been determined. The slight spectral changes on entering phase IV are accounted for by proposing the adoption of a monoclinic C_{2h}^n ($n = 2$ or 5) space group, the choice of $n = 5$ being the more likely. The mode behaviour within phase II is shown to

be consistent with the CO₂ structure type suggested earlier. The four known polymorphs of HgBr₂ are also characterised, the transition pressures being at 4.0, 26.0 and 41.0 kbar. Detailed spectra of phase II are presented for the first time. Despite any superficial similarities between the spectra of the four phases of each material, it is considered that the sequences bear no structural equivalences.

4.6 References

1. P. W. Bridgman, *Proc. Amer. Acad. Arts Sci.* **72**, 45, (1937).
2. D. B. Balashov and D. A. Ikhenov, *Fiz. Tverd. Tela.* **17**, 2693, (1975).
3. C. W. F. T. Pistorius, *Progr. Solid-State Chem.* **11**, 1, (1976).
4. D. M. Adams and R. Appleby, *J. Chem. Soc. Dalton Trans.*, 1530, (1977); *ibid.*, 1535, (1977).
5. R. W. G. Wyckoff. "Crystal Structures", 2nd edn., vol. 1, Wiley-Interscience, New York, 1964.
6. H. Sponer and E. Teller, *Rev. Mod. Phys.* **13**, 75, (1941).
7. H. Braune and G. Engelbrecht, *Z. Physik. Chem. (Leipzig)* **B19**, 303, (1932).
8. W. Klemperer and J. Lindemann, *J. Chem. Phys.* **25**, 397, (1956).
9. W. Klemperer, *J. Electrochem. Soc.* **110**, 1023, (1963).
10. A. Büchler, J. L. Stauffer, and W. Klemperer, *J. Chem. Phys.* **40**, 3471, (1964).
11. V. Subramanian and K. Seff, *Acta Cryst.* **B36**, 2182, (1980).
12. L. E. Orgel, *J. Chem. Soc.*, 4186, (1958).

13. W. Roy Mason, *J. Am. Chem. Soc.* **95**, 3573, (1973).
14. H. Poulet and J. P. Mathieu, *J. Chim. Phys. Physiochim. Biol.* **90**, 442, (1963).
15. S. Brahms and J. P. Mathieu, *Compt. Rend.* **251**, 938, (1960).
16. E. A. Décamps and A. Hadni, *J. Chim. Phys.* **65**, 1030, (1968).
17. D. M. Adams and D. J. Hills, *J. Chem. Soc. Dalton Trans.*, 776, (1978).
18. G. Turrell, "Infrared and Raman Spectra of Crystals", Academic Press, London, 1972.
19. G. Herzberg, "Molecular Spectra and Molecular Structure, II Infrared and Raman Spectra of Polyatomic Molecules", van Nostrand, New York, 1956.
20. S. Lewis and W. F. Sherman, *Spectrochim. Acta* **35A**, 613, (1979).
21. A. A. Malts'ev, G. K. Selivanov, V. I. Yampolskii, and N. F. Zavalishin, *Nature Phys. Sci.* **231**, 157, (1971).
22. A. Löwenschuß, A. Ron, and O. Schnepf, *J. Chem. Phys.* **50**, 2502, (1969).
23. Y. Mikawa, R. J. Jakobsen, and J. W. Brasch, *J. Chem. Phys.* **45**, 4528, (1966).
24. E. A. Décamps, Y. Marqueton, M. Durand, and F. Abba, *J. Mol. Struct.* **19**, 505, (1973).

CHAPTER 5

A RAMAN AND INFRARED VIBRATIONAL STUDY OF SOME PYROXENE VARIANTS

I. The Alkali Metavanadates MVO_3 , $M = K, Rb, Cs$

II. Copper Metagermanate, $CuGeO_3$

CHAPTER 5

I. AN INFRARED AND RAMAN STUDY OF THE ALKALI METAVANADATES, MVO_3 , $M =$ \underline{K}^+ , \underline{Rb}^+ , \underline{Cs}^+

5.1 Introduction

The pyroxene structure is one of extreme flexibility and a wide variety of compounds crystallise in one or more variants of this structure type. In particular, some of the large number of nonsilicate pyroxenes show extremes of structural distortion and additional structural forms that are not present in known silicate systems.

The fundamental characteristic of this and related structural families is the infinite chains of vertex-linked AB_4 anion tetrahedra. They can be readily distinguished by the number (n) of tetrahedra in the chain repeat, the value of which is usually determined by the particular structural requirements of the cation(s) in any given compound. Thus, structures exist in which nearly all values of n , from one to twelve, are to be found, Table 5:1.

The ambient phases of the metavanadate pyroxenes of the form MVO_3 ($M^+ = Li, Na, K, Rb, Cs, NH_4$) have been widely studied using single crystal x-ray diffraction, and the structures accurately refined (crystallographic data are presented in Table 5:2).¹ The series can be split into two structural types; those with a monoclinic cell ($M = Li, Na$) similar to that of the mineral diopside, $CaMg(SiO_3)_2$, and those adopting an orthorhombic phase ($M = K, Rb, Cs, NH_4$). In the structures of $LiVO_3$ ² and $NaVO_3$ ³ edge-sharing chains of M1 octahedra extend along c , and are linked by corner-sharing to infinite chains of VO_4 tetrahedra. Highly distorted M2 sites provide additional linkage between the octahedral and tetrahedral chains, producing a staggered layer motif stacked (by C-centring) along a .

The structure of the orthorhombic metavanadates is shown in Fig. 5:1. As with the monoclinic phases it is characterised by infinite anionic, corner-sharing tetrahedral chains. The alkali metal coordination increases from six to eight/ten and the octahedral chains

Table 5:1 Representative compounds with n -repeat AB_4 chain tetrahedra

n		
1	Copper metagermante	$CuGeO_3$ K_2CuCl_3
2	Potassium metavanadate Diopside	KVO_3 $CaMg(SiO_3)_2$
3	Wollastonite Bustamite	$CaSiO_3$ $(Mn, Ca, Fe)SiO_3$
4	Silver metaphosphate	$AgPO_3$
5	Rhodonite	$MnCa(SiO_3)$
6	Stokesite	$Ca_2Sn_2(SiO_3)_6 \cdot 4H_2O$
7	Pyroxmangite	$(Mg, Fe, Ca, Mn)SiO_3$
9	Ferrosilite III	$FeSiO_3$
12	Alamosite	$PbSiO_3$

Table 5:2 Crystallographic data for the orthorhombic metavanadate pyroxenes

	KVO ₃	RbVO ₃	CsVO ₃
<i>a</i> (Å)	5.176(2)	5.261(1)	5.393(1)
<i>b</i> (Å)	10.794(3)	11.425(2)	12.249(2)
<i>c</i> (Å)	5.680(2)	5.715(1)	5.786(1)
<i>v</i> (Å ³)	317.3	343.5	382.2
<i>Z</i>	4	4	4
Space group	<i>Pbcm</i>	<i>Pbcm</i>	<i>Pbcm</i>
ρ_c	2.889	3.565	4.028

Table 5:4 Mode analysis for the chains of KVO₃

$C_{2v}(x)$	N_T	$\nu(V=O)$	δVO_2	ρ_r	ρ_w	ρ_t	$\nu(V-O)$	Δ
A_1	6	2	1	1			1	1
B_1	7	2	1	1			1	2
B_2	4				1	1	1	1
A_2	3				1	1	1	

N_T = total number. ρ_r , ρ_w , ρ_t are respectively the rock, wag and torsional modes of the (VO₂) groups.

Δ = deformational modes of the [V₂O₂] chain backbone.

Figure 5:1

Crystal structure of MVO_3 , $M = K,$
Rb, Cs.

Covalent radii used:

M (1.33)

V (1.33)

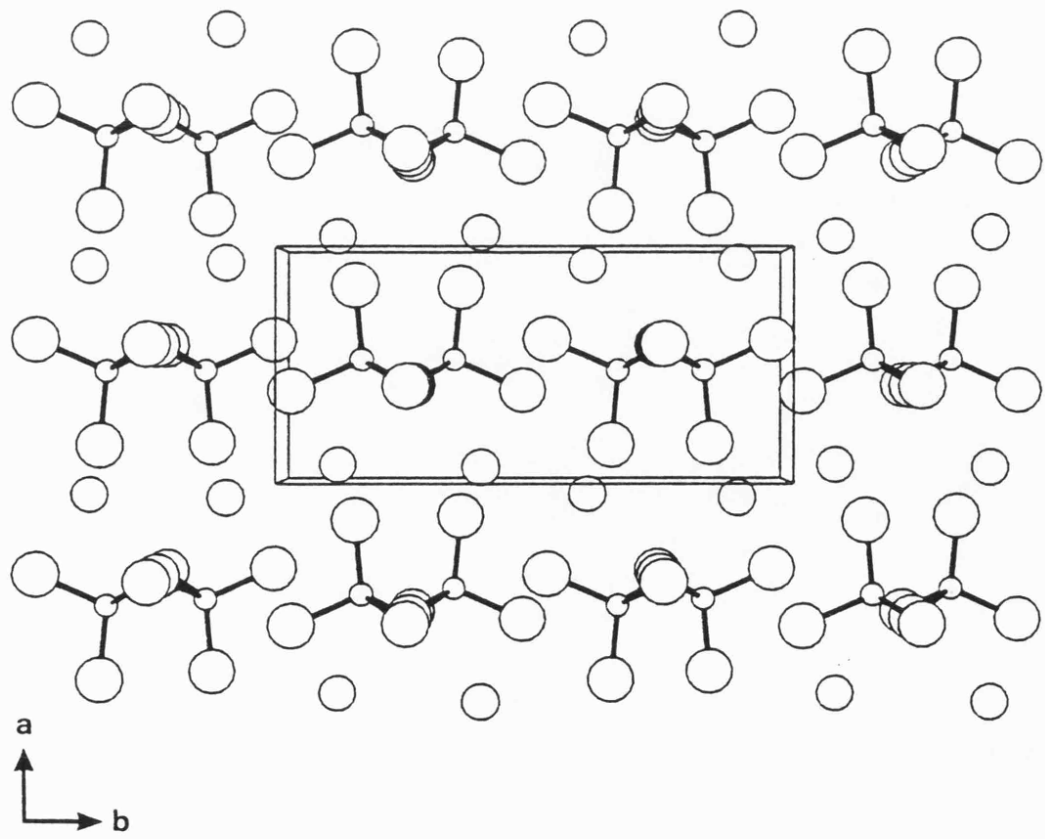
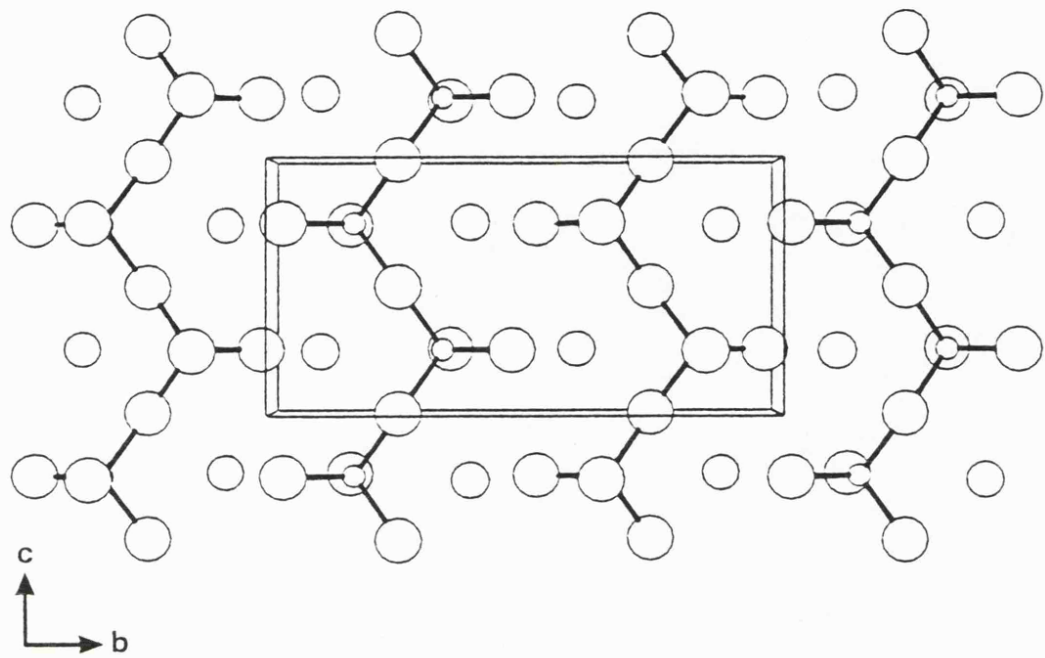
O (0.68)

The atoms are shown as spheres of
relative sizes:

M (0.4)

V (0.25)

O (0.5)



of the monoclinic structure are replaced by edge-sharing chains of irregular eight-coordinated polyhedra parallel to *c*. However, whereas the chains in the monoclinic case are separated in the *b-c* plane by a double band of M1 octahedra, the chains in the orthorhombic structure are separated by a single band of edge-sharing polyhedra. The resultant stacking sequences for the two types are thus completely different: successive layers of chains in the orthorhombic structure are repeated by a simple lattice translation, those in the monoclinic structure by a C-centring and twofold symmetry operations.

The only reports of any completeness on the vibrational spectra of the solid metavanadates are those of Botto *et al.*⁴ and Ondera and Ikegami,^{5,6} although they provide little in the way of assignment. Within the confines of a treatment without resort to a normal coordinate analysis, the much improved infrared and Raman data presented here allow for a nearly complete assignment, Figs. 5:2-5:5. Further, high pressure data in the mid-infrared have revealed a transition which is unusually insensitive to change of cation through the series.

5.2 Experimental

All the alkali-metal metavanadates were prepared by the reaction in aqueous solution of the metal carbonate with vanadium (V) oxide.⁷ They appear as white powders, but are sometimes contaminated with trace amounts of the intense yellow-orange $[V_{10}O_{23}]^{6-}$ species formed by the reaction with atmospheric carbon dioxide.

Ambient, low-temperature and high pressure mid-infrared data were collected on a Perkin-Elmer 580B dispersive instrument, the latter with the addition of a refracting beam condenser.⁸ The samples were diluted in an approximate ratio of one part sample to nine parts KBr, and loaded into gaskets 0.075 mm thick with a hole diameter from 0.6-0.9 mm (initial dimensions). Nujol was occasionally used as the pressure transmitting fluid, however, the KBr dilutant was found to remain sufficiently plastic to provide hydrostatic conditions up to all but the highest pressures.

Far-infrared and Raman spectra at 298 and 80 K were recorded on a Beckman-RIIC FS-720 fourier transform, and Coderg T800 triple-

Figure 5:2

80 K Raman capillary spectra of the internal modes of crystalline MVO_3 , $M = K, Rb, Cs$.

All spectra were recorded at a spectral slit width of 0.5 cm^{-1} and *ca.* 50 mW 514.5 nm Ar^+ radiation at the sample.

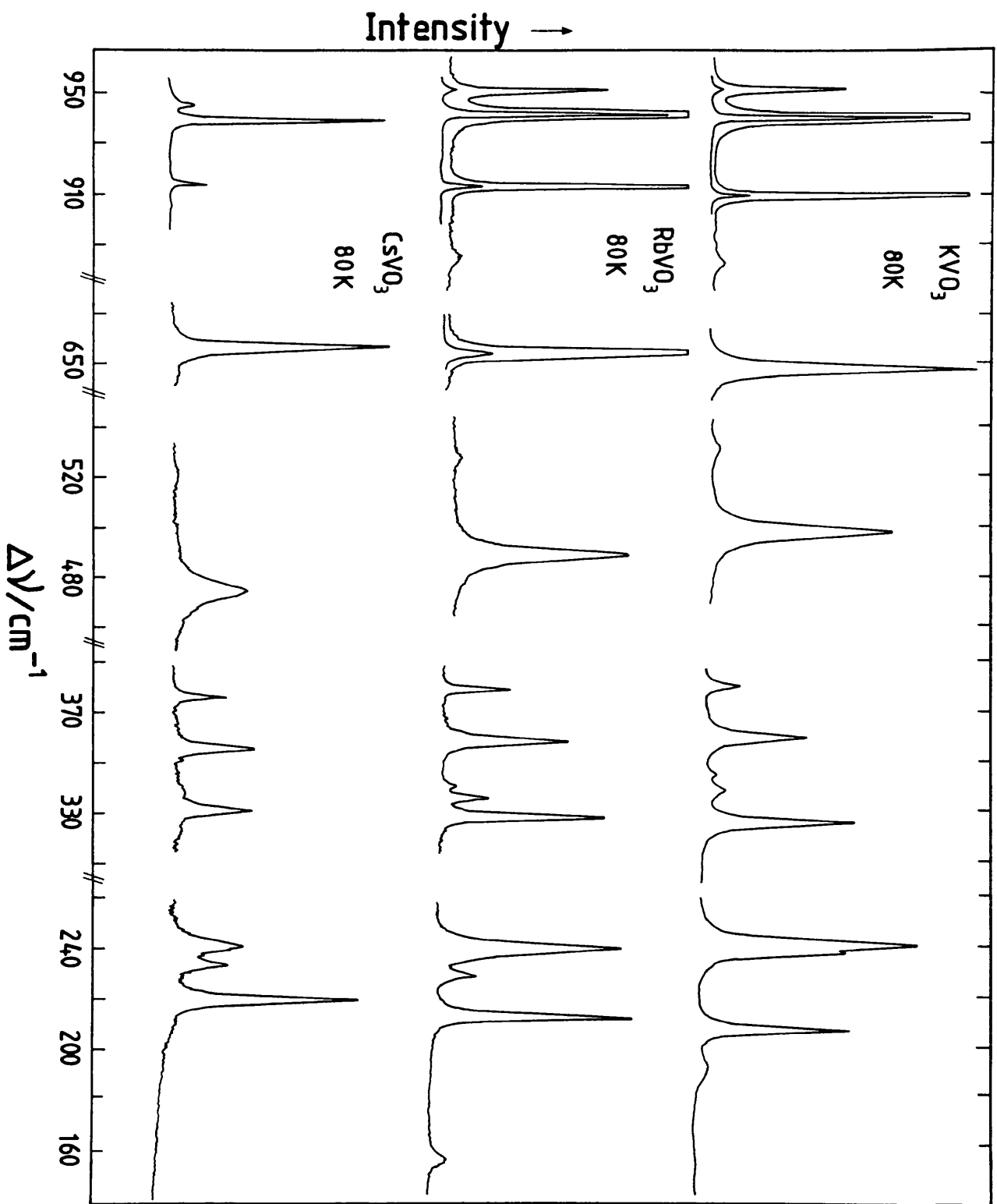


Figure 5:3

293 and 80 K Raman capillary spectra of the external modes of MVO_3 , $M = K, Rb, Cs$.

All spectra were recorded at a spectral slit width of 1.0 cm^{-1} and *ca.* 50 mW 514.5 nm Ar^+ radiation at the sample.

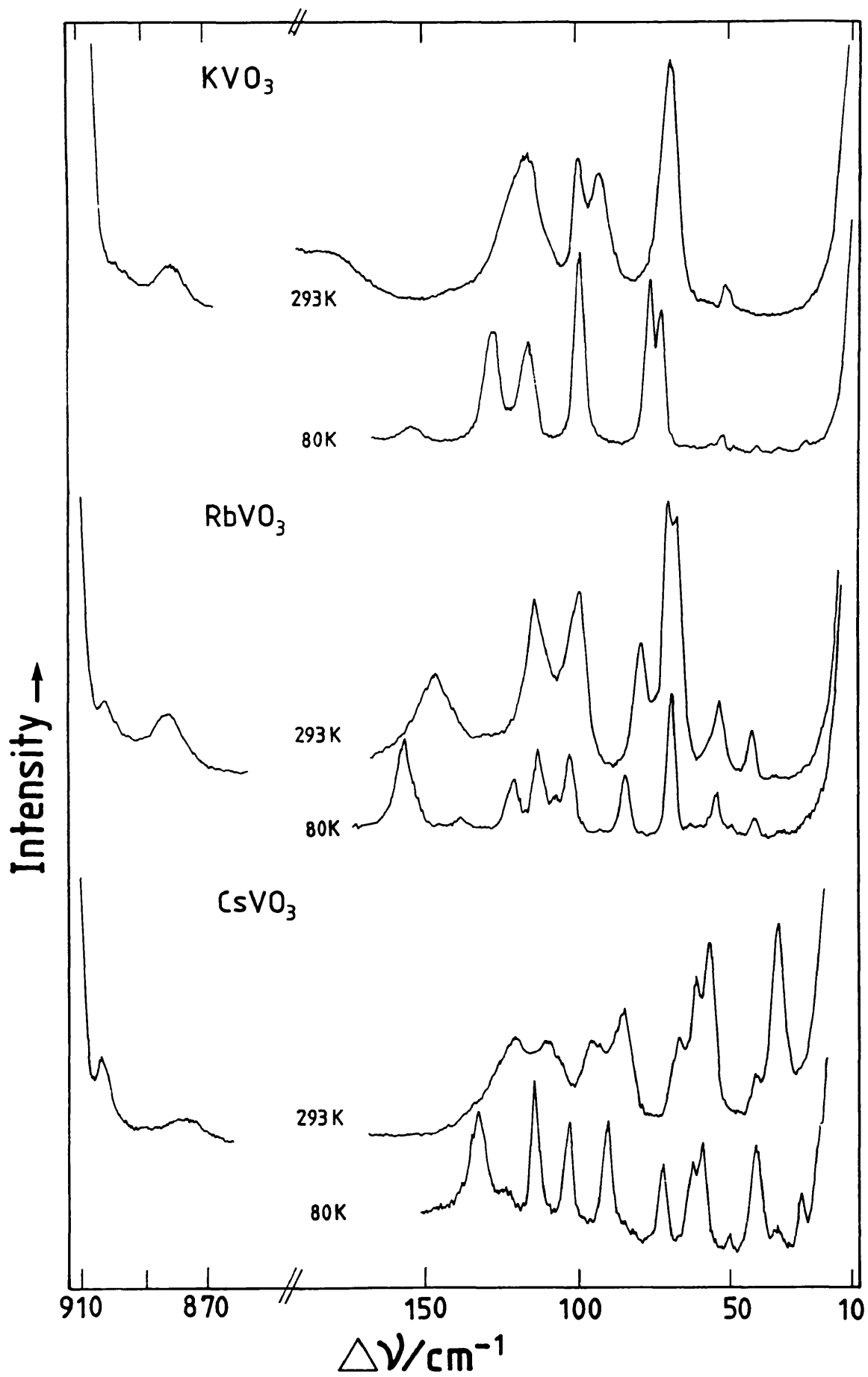


Figure 5:4

293 and 80 K mid-infrared spectra
of MVO_3 , $M = K, Rb, Cs$.

Spectra were recorded as KBr, RbCl
and CsI discs respectively, with a
resolution of *ca.* 2.0 cm^{-1} .

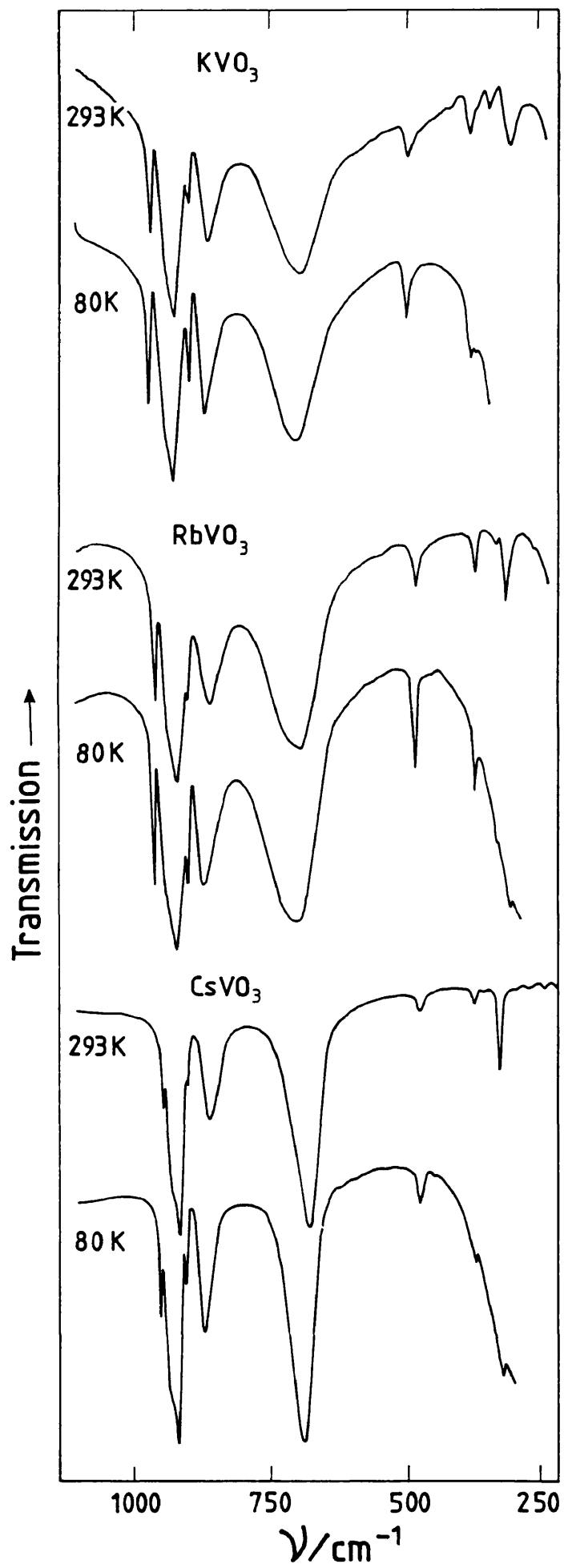
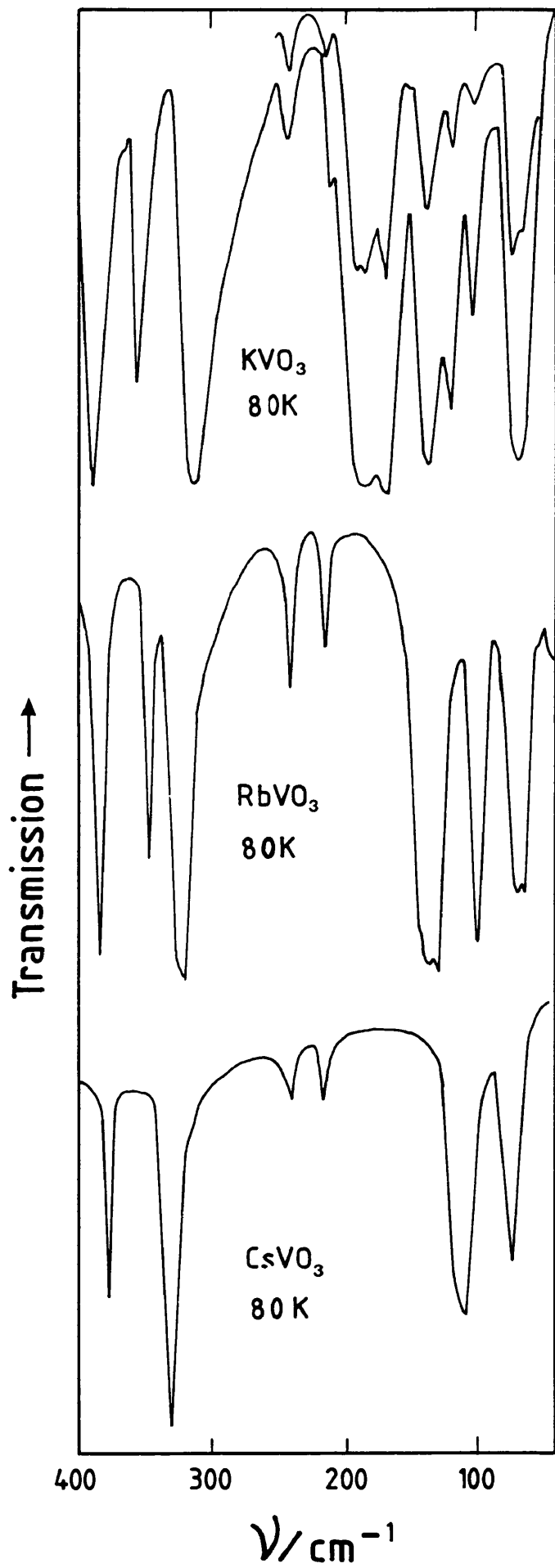


Figure 5:5

80 K far-infrared spectra of MVO_3 ,
M = K, Rb, Cs.

Spectra were recorded down to 40
 cm^{-1} as nujol mulls on polyethylene
discs, resolution *ca.* 1.0 cm^{-1} .



monochromator instruments, respectively. Low temperature work was carried out using simple evacuated glass cryostats with either KBr or polyethylene windows (i.r.), and an Oxford instruments DN704 variable temperature liquid nitrogen cryostat (Raman).

5.3 Vibrational Analysis and Assignment

The orthorhombic alkali-metavanadates all crystallise in the space group $Pbcm \equiv D_{2h}^{11}$ (No.57), with a tetramolecular primitive cell.¹ There are two chains per cell running parallel to c , with a $[V_2O_6]$ repeat, each possessing the symmetry elements $\{E|0\}$, $\{C_2(x)|0\}$, $\{\sigma(xz)|00\frac{1}{2}\}$ and $\{\sigma(xy)|0\frac{1}{2}0\}$. These, together with the infinite group of primitive translations, form a one-dimensional space group, the factor group of which is isomorphous with the point group C_{2v} . The site symmetry of the chains in the unit cell is also C_{2v} and, although there are no such sites in $Pbcm$, a set does exist in $Pmnn \equiv D_{2h}^{13}$ (No.59) which may be used to compute the chain external mode representation. The factor group analysis (f.g.a.) is shown in Table 5:3. Further, a complete decomposition of the 20 internal modes of each individual C_{2v} chain is given in Table 5:4.

The use of the f.g.a. to distinguish between internal and external motions is based on an ionic structural model, $M^+VO_3^-$. This implies that the spectra can be interpreted in terms of two vibrationally coupled vanadate chains, together with cation translations. The spectra do indeed support this approach. There are many i.r./Raman band pairs with quite modest splittings, and there are cation-sensitive modes at frequencies consistent with those for K^+ , Rb^+ and Cs^+ in salts such as the hexahalometallates.⁹

A simple internal coordinate treatment for the V-O bond stretching in the single $[V_2O_6]$ chain repeat is given as part of Table 5:4. The four $\nu(V=O)$ species in C_{2v} ($2A_1 + 2B_1$) yield sets of four i.r. ($2B_{2u} + 2B_{3u}$) modes, whilst vibrations of the V-O-V chain backbone are $A_1 + A_2 + B_1 + B_2$, coupling within the unit cell to yield a complete vector of eight modes in D_{2h} of which four ($A_g + B_{1g} + B_{2g} + B_{3g}$) are allowed in the Raman and three ($B_{1u} + B_{2u} + B_{3u}$) in the infrared. Thus, in all, there should be eight Raman and seven i.r. bands associated with V-O bond stretching. However, coupling between the backbone modes may well

Table 5:3 A. Factor group analysis for KVO_3

D_{2h}	N_T^a	T_A	T	R_z	Γ_{vib}	Activity
A_g	9		3		6	Raman
B_{1g}	10		2	1	7	Raman
B_{2g}	6		2		4	Raman
B_{3g}	5		2		3	Raman
A_u	5		1	1	3	Inactive
B_{1u}	6	1	1		4	Infrared
B_{2u}	10	1	2		7	Infrared
B_{3u}	9	1	2		6	Infrared

B. Coupling between chains

Single chain, $C_{2v}(x)$	$\xrightarrow{x2}$	Unit cell, $^b D_{2h}^{11}$
$6A_1$		$6(A_g + B_{3u})$
$7B_1$		$7(B_{1g} + B_{2u})$
$4B_2$		$4(B_{2g} + B_{1u})$
$3A_2$		$3(B_{3g} + A_u)$

C. Correlation between D_{2h} and C_{2v} for the $[V_2O_2]$ modes

D_{2h} (chain)	C_{2v}^c (chain)	D_{2h}^{11} (unit cell)
$2B_{2u} (\nu_5, \nu_6)$	$2A_1$	$2(A_g + B_{3u})$
$2B_{3u} (\nu_7, \nu_8) + A_g (\nu_1)$	$3B_1$	$3(B_{1g} + B_{2u})$
$2B_{1u} (\nu_3, \nu_4)$	$2B_2$	$2(B_{2g} + B_{1u})$
$B_{3g} (\nu_2)$	A_2	$(B_{3g} + A_u)$

$a N_T$ = total number of unit cell modes; T_A = acoustic branch, T = optic branch; R_z = chain libration, Γ_{vib} = coupled vibrations of two chains.

b This column is equivalent to Γ_{vib} in A.

c Includes x/z axis interchange to align with Table A.

be slight; this will result in near coincidence of i.r./Raman band pairs.

A further understanding of the $[V_2O_2]$ chain backbone, which has C_{2v} line group symmetry, follows from treating it in isolation. By forcing it to be planar with line group symmetry D_{2h} , the modes are more readily visualised. Of the $(3n-4)$ vibrations generated by this repeat, six are in-plane and two out-of-plane. Their approximate forms are shown in Fig. 5:6, and are related to those of the real backbone as shown in Table 5:3 C. The highest in frequency will be ν_7 , B_{3u} which has the form of a longitudinal optic mode and thus must be higher than ν_3 , B_{1u} which is transverse optic-like.

With reference to KVO_3 there are eight Raman and seven i.r. bands down to and including the Raman/i.r. pair close to 500 cm^{-1} . Subsequently, there is a gap of over 100 cm^{-1} before a long series of deformational modes begins. The immediate problem in the assignment is whether or not the 500 cm^{-1} pair are due to a $\nu(V-O-V)$ mode? These bands are unique in this set in being significantly cation-sensitive, suggesting that they are associated with a mode involving the chain exterior. Since they are at about half the $\nu(V=O)$ energy, it is considered that a $\delta(VO_2)$ mode is a more likely assignment.

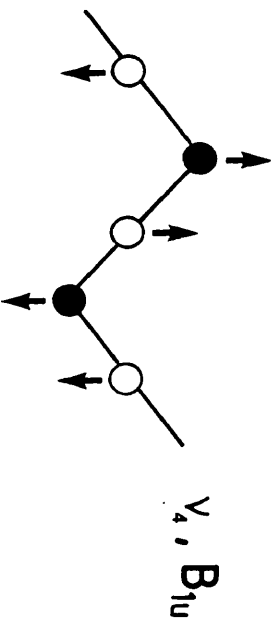
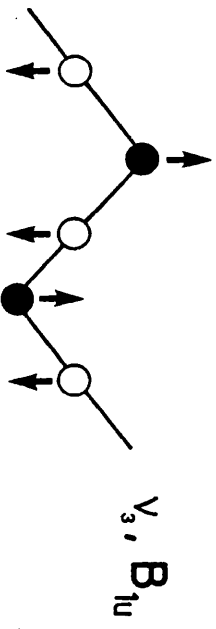
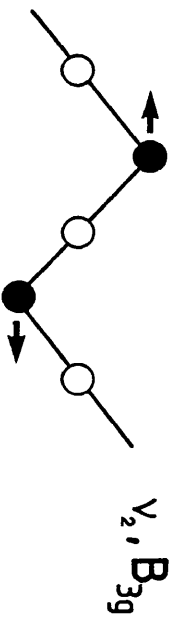
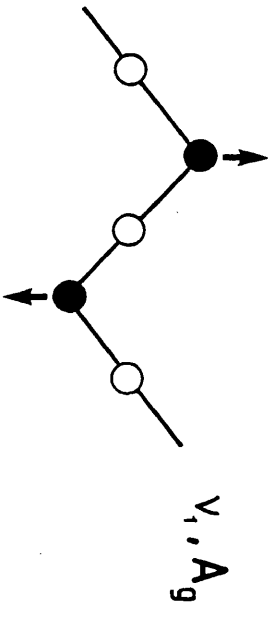
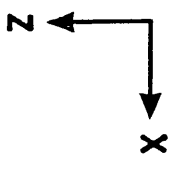
The coupling scheme of Table 5:3 B requires that all i.r.-active chain modes have Raman counterparts. The possibility of i.r.-unique translatory lattice modes exists (Table 5:3 A) and will be discussed below, but will not affect the region above 150 cm^{-1} . In the interval down to 200 cm^{-1} all i.r. bands do indeed have Raman counterparts with the notable exception of the 701.5 cm^{-1} band.

Unique Raman bands may arise in the region below 150 cm^{-1} for two reasons: (i) they are of A_2 symmetry in the isolated chain and do not generate a dipolar factor group component, Table 5:3 B; (ii) accidental weakness of an i.r. component. In the former case Table 5:4 shows that only three such modes are predicted and that two of them are deformations expected below 500 cm^{-1} , and are identified with the bands at 347.9 and 245.6 cm^{-1} .

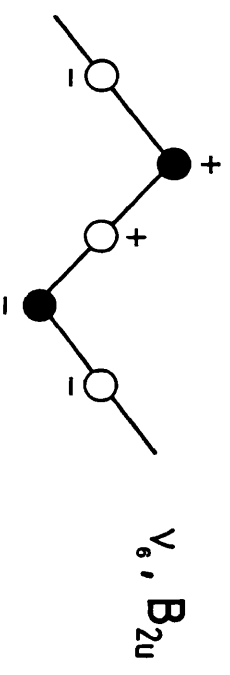
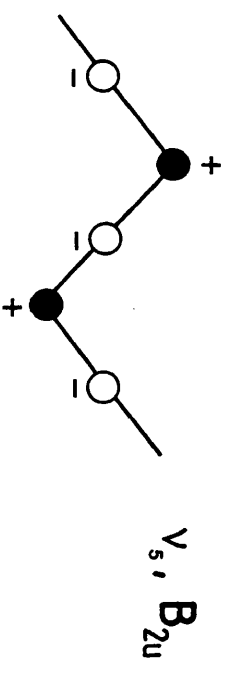
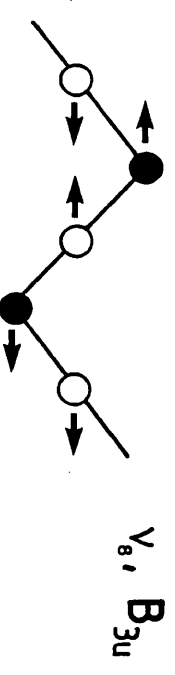
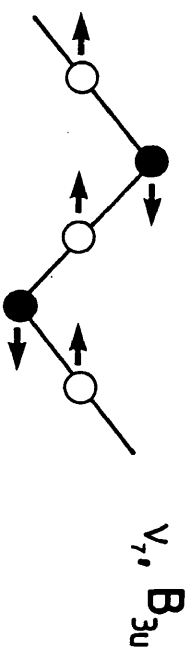
The Raman bands at 649.0 and 532.8 cm^{-1} and the i.r. feature at 701.5 cm^{-1} have no counterparts. The i.r. band should have one but it

Figure 5:6

Approximate forms of the six
in-plane and two out-of-plane modes
of the D_{2h} $[V_2O_2]$ chain backbone.



● = V



● = V

appears to be vanishingly weak; this can be understood if it is a $[V_2O_2]$ backbone mode derived from ν_7 , B_{3u} with little or no coupling to the next chain. Of the two Raman bands one is permitted to be unique to that spectrum but the other must have a vanishingly weak i.r. component. On this basis the assignment of Table 5:5 is reached, placing all $\nu(V-O-V)$ modes above 500 cm^{-1} .

The assignment of the modes below 510 cm^{-1} must now be considered. Of these, fourteen of the fifteen i.r. modes required by the theory have been observed (*i.e.* the factor group requirement of twenty two less the seven $V=0$ and $V-O-V$ stretches). Similarly, the Raman spectrum shows twenty one of the expected twenty two modes for this region.

Ten i.r.-active deformational modes of the individual chains should each have a Raman counterpart, and at least this number of pairs is present, Table 5:5. In addition, there are translatory lattice modes, five being permitted in the infrared. The Raman spectrum is more complex in the region below 150 cm^{-1} since the selection rules allow ten lattice modes, almost all of which have been located.

The interpretation of the spectra of $RbVO_3$ and $CsVO_3$ follows from the above arguments. All three compounds show essentially identical Raman and infrared spectra down to 200 cm^{-1} , taking into account the shifts in frequency concomitant with change of cation. Since, in general, the lower frequency modes are most susceptible to increasing cation size, it is not surprising that the lattice region differs more than any other through the series. The distinction between the lowest frequency chain deformations and highest frequency lattice modes made in Tables 5:6, 5:7 could, therefore, be easily lost. There is also the possibility of accidental degeneracies occurring between modes of different symmetry, a fact that accounts well for the simplification observed in the infrared on passing from KVO_3 to $CsVO_3$. Hence, this region should most benefit from a normal coordinate analysis, since such a treatment necessarily takes into account force constant changes with mass and bond distance/angle variations.

Table 5:5 Assignment for KVO_3

Raman		Assignment	Infrared	
293 K	80 K		80 K	293 K
947.7	950.1	↑	967.0	964.1
938.0	938.7		~942	~940
908.4	908.4	$\nu(V=0)$	922.5	921.9
~897		and	894.3	894.0
880.0	881.7	$\nu(V-O-V)$	865.6	859.3
	<i>a</i>	↓	701.5	695.3
647.0	649.0		<i>b</i>	
529.5	532.8	<i>b</i>		
499.0	500.4	$\delta(VO_2)$	502.0	498.0
381.6	383.4	↑	388.5	384.5
361.5	362.9		354.8	350.0
	347.9	VO_2 ρ_r , ρ_τ , ρ_ω		
	341.8		<i>a</i>	
330.0	329.5		313.5	315.3
245.5	245.6	and chain		
240.5	242.6		241.8	241.7
213.2	212.1	deformations	210.6	213.2
186.0	~196 ^c	↓	188.1	
	<i>a</i>			173.8
	~157	↑	180.9	
	130.9		166.5	159.2
122.9	119.5		134.8	125.4
		Lattice	116.6	112.8
104.6	103.0		100.0	93.3
99.3		modes		
	80.9			
76.9	76.6		67.8	73.9
			63.5	
57.3	56.6	↓		
	44.8			
	28.1			

Table 5:6 Assignment for RbVO_3

Raman		Assignment	Infrared	
293 K	80 K		80 K	293 K
947.1	950.1	↑	961.8	955.8
939.0	940.3		~940	~937
910.9	912.0	$\nu(V=0)$	920.5	918.6
901.4		and	898.0	897.1
881.0	884.7	$\nu(V-O-V)$	871.3	860.8
	<i>a</i>	↓		
651.4	654.7		<i>b</i>	
525.5	529.0		<i>b</i>	
489.3	490.8	$\delta(\text{VO}_2)$	490.1	487.8
378.2	380.7	↑	383.5	379.5
358.9	360.4		$\text{VO}_2 \rho_r, \rho_t, \rho_\omega$	
	342.8		346.1	341.5
	338.4			
331.1	331.0	and chain	321.6	324.4
241.6	243.1		241.5	~242
229.8	231.6	deformations		
217.5	216.1	↓	214.5	~215
	159.9			
145.8			136.0	
	139.4	↑		
	122.8		127.9	~124
115.2		Lattice		
	115.0			
101.1	104.8		97.7	93.0
80.7	86.8	modes		
72.3		↓		
	71.7		67.5	~67
69.4				
55.3	56.8			
44.9	44.5			
	27.2			

a, b See Table 5:7

Table 5:7 Assignment for CsVO₃

Raman		Assignment	Infrared	
293 K	80 K		80 K	293 K
942.0	944.4	↑	948.5	946.5
937.6	938.3		~936	~932
912.4	913.6	$\nu(V=0)$	918.5	917.3
902.9	905.0	and	902.0	900.8
~877		$\nu(V=0-V)$	869.4	861.8
	<i>a</i>	↓	688.0	680.6
653.7	657.2		<i>b</i>	
~518	~522		<i>b</i>	
477.1	476.9	$\delta(VO_2)$	477.5	477.0
375.6	377.0	↑	378.0	377.4
356.0	356.7		$VO_2 \rho_r, \rho_r', \rho_\omega$	
	339.6			
332.4	332.5	and chain	330.9	332.4
242.2	240.9		241.9	~242
233.1	233.4	deformations		
221.2	220.6	↓	217.8	~220
124.3	133.5	↑		
113.4	115.3		~119	
98.8	104.3		110.3	~107
87.8	91.6	Lattice		
69.4	73.2		73.5	~76
63.0	64.1	modes		
59.1	61.4	↓		
43.1	51.5			
37.1	42.6			
	35.6			
	27.8			

a Vanishingly weak component. *b* One of these Raman bands has a vanishingly weak i.r. component. *c* Broad, almost certainly two components.

5.4 Results and Discussion

5.4.1 High Pressure Behaviour of RbVO₃

The mid-infrared spectra of RbVO₃ up to a pressure of 100 kbar are shown in Fig. 5:7. At 53 kbar the mode plots, Figs. 5:8, 5:9, Table 5:8, indicate the onset of a phase transition, a change most clearly seen in the region below 520 cm⁻¹. An area of intergrowth between phases I and II extends for about 12 kbar, thereafter pure RbVO₃ II exists up to the limit of current observations. The mode shifts of all bands above 380 cm⁻¹ are to higher frequencies. In the light of the following discussion of the behaviour within compounds of this structure type, this hardening can be considered as being primarily the effect of a contraction in the cation polyhedra, rather than a significant reduction in the V-O bond distances.

The limited information available from the mid-infrared spectrum alone precludes any detailed description of the nature of this transition. However, the behaviour of the region near *ca.* 500 cm⁻¹ is such as to require further comment. At this frequency bands are believed to be associated with $\delta(\text{VO}_2)$ motions and in the ambient phases of MVO₃ (M = K, Rb, Cs), they are especially cation-sensitive. Any repacking of the lattice would, therefore, affect this region significantly. The plots show that the single band initially at 490 cm⁻¹ is replaced by three in phase II, an increase in complexity which suggests an increase in unit cell size, possibly a cell doubling.

5.4.2 Structural Implications for the I → II Transition

It has been suggested, on the basis of metal-oxygen bond compressibilities in olivines and garnets,¹⁰ that as cation polyhedra are subjected to increasing pressure they become more regular and polyhedral distortions less significant. However, subsequent studies of zircon,¹¹ corundum-type compounds¹² and rutile-type oxides¹³ revealed the opposite trend, with polyhedra becoming more distorted at high pressure. It is clear then, that variation of polyhedral distortion with pressure is not readily predicted. One clear concept to arise from these studies is that of differential polyhedral contraction/expansion,

Figure 5:7

Mid-infrared spectra of RbVO_3 at ambient temperature and various pressures.

Spectra were recorded at a maximum resolution of 5.3 cm^{-1} .

* Denotes an instrumental feature due to a grating change.

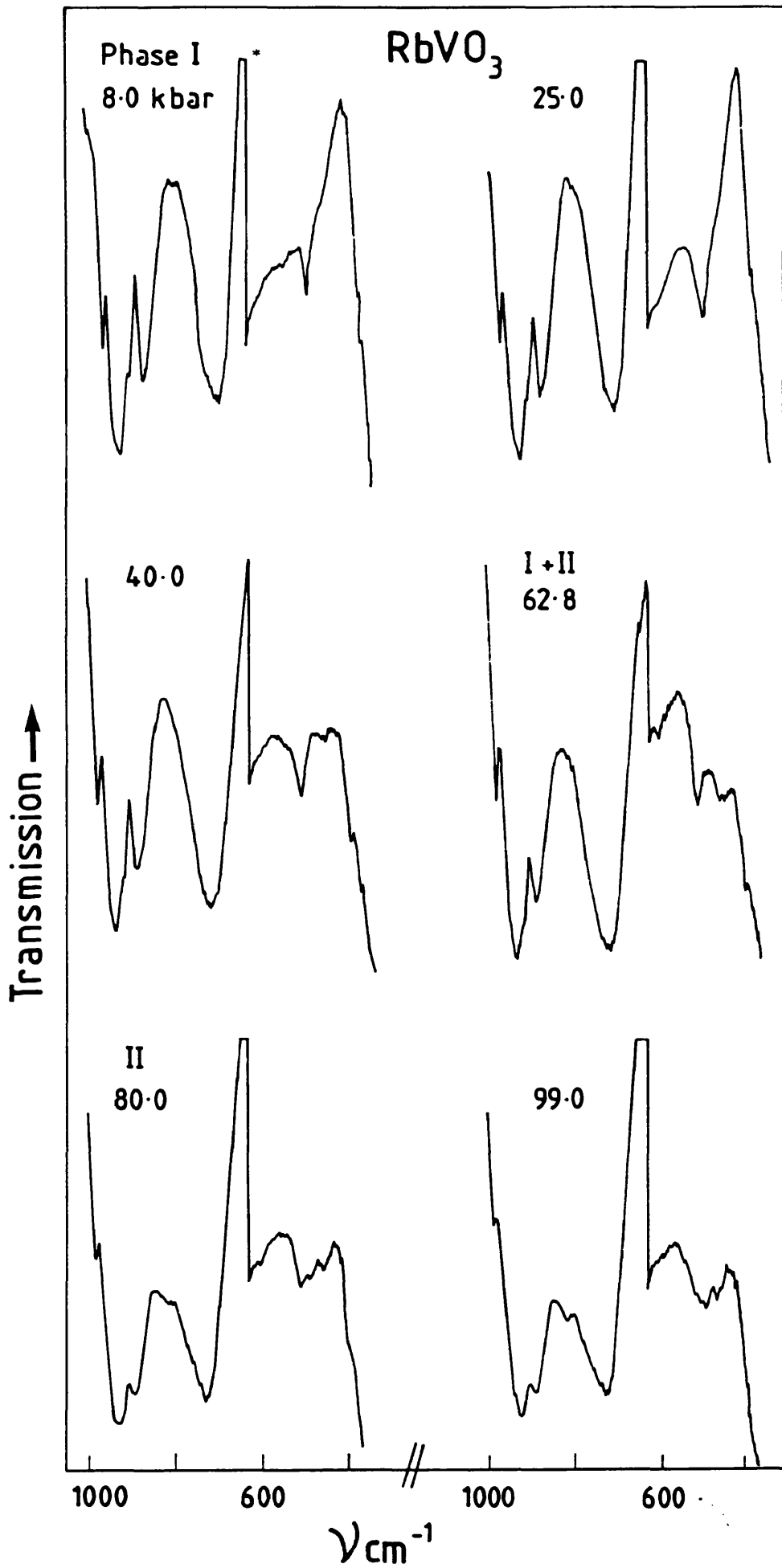


Figure 5:8

Plot of frequency (ν/cm^{-1}) against pressure for the infrared active modes of RbVO_3 in the region 820 - 350 cm^{-1} .

Solid lines were obtained by the method of least squares. Errors were estimated from the instrumental resolution and accuracy of measurement.

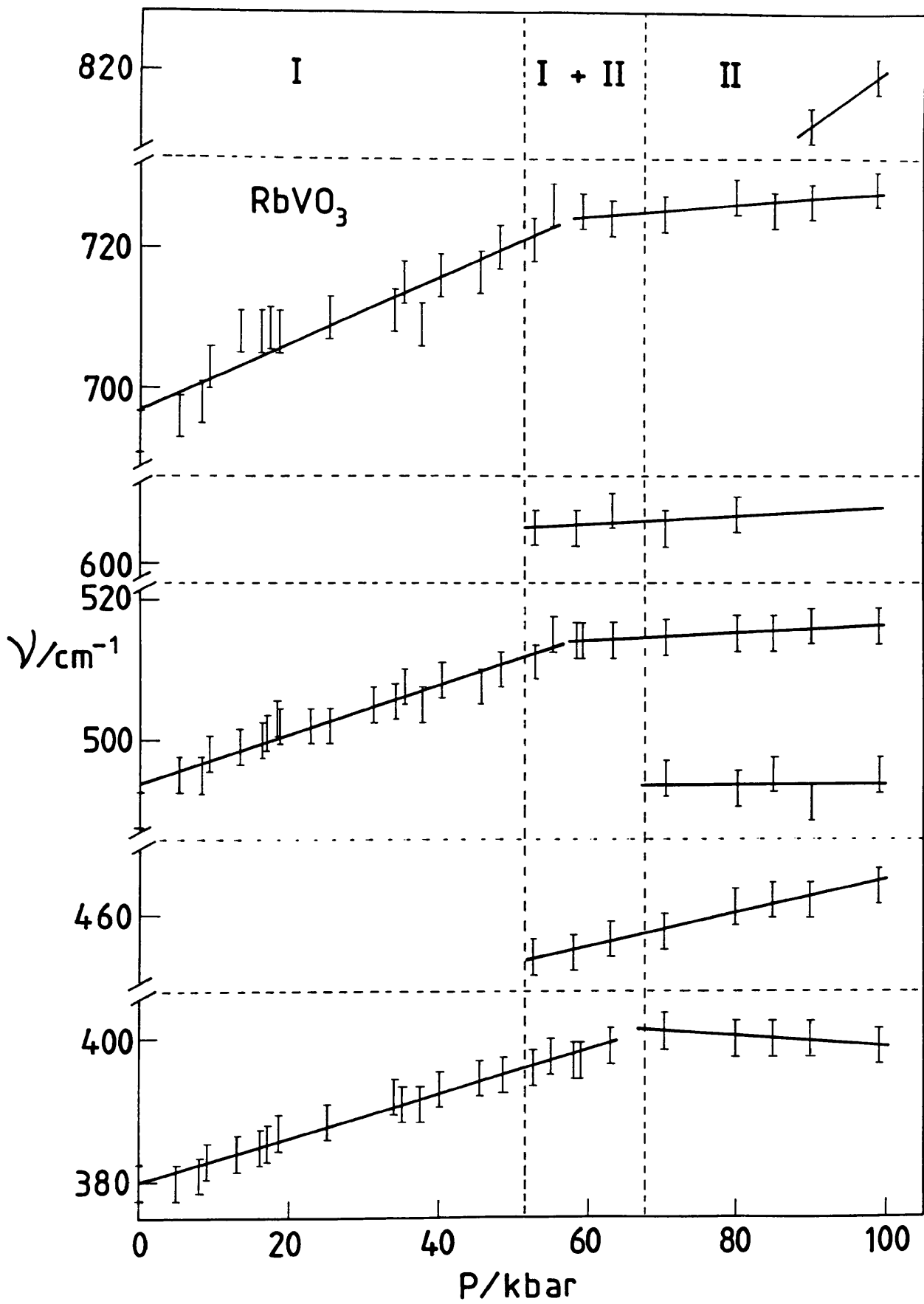


Figure 5:9

Plot of frequency (ν/cm^{-1}) against pressure for the infrared active modes of RbVO_3 above 860 cm^{-1} .

Solid lines were obtained by the method of least squares.

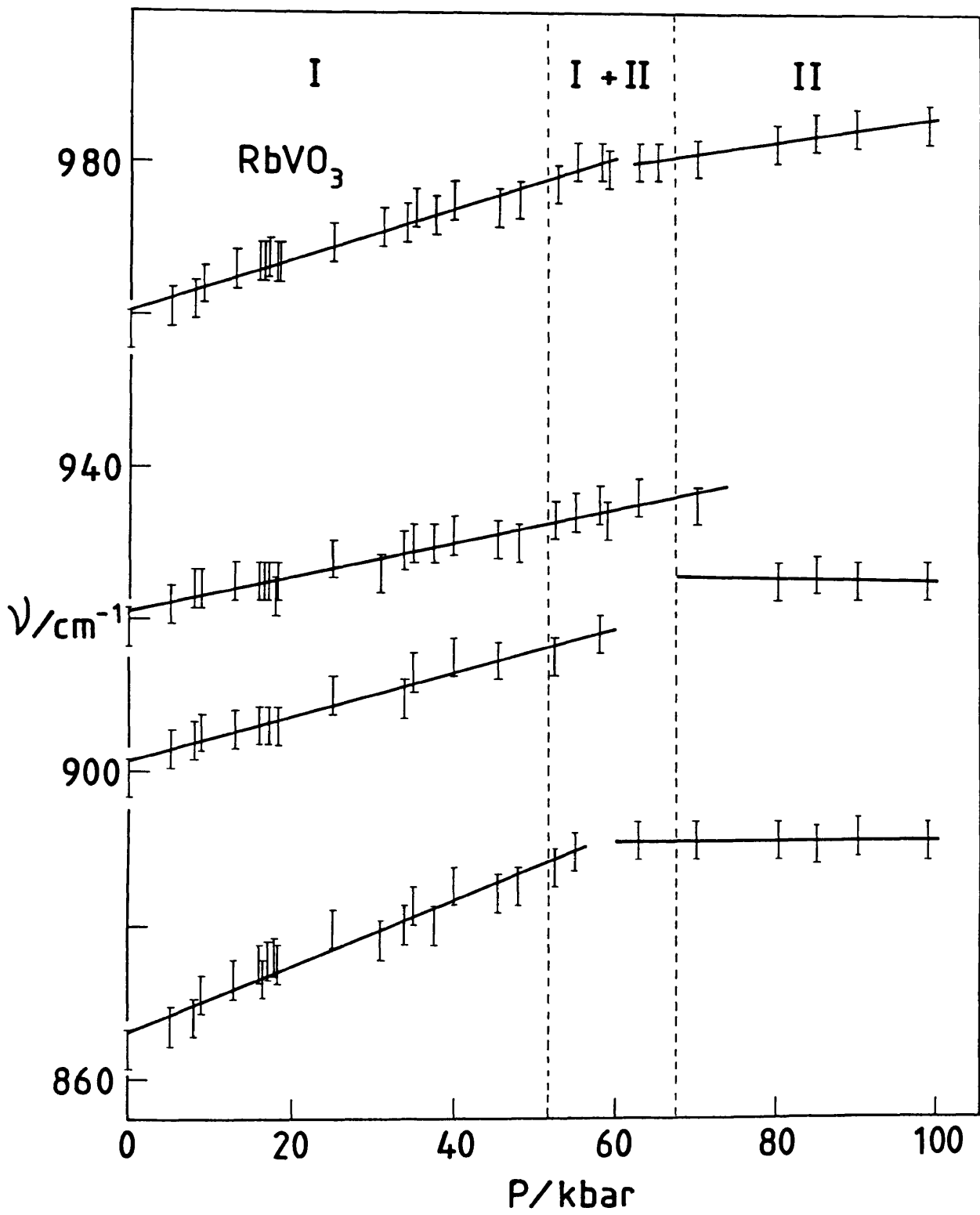


Table 5:8 Infrared frequencies and their pressure dependencies for RbVO_3

	$\nu \text{ cm}^{-1}$	$\frac{d\nu}{dP} \text{ cm}^{-1} \text{ kbar}^{-1}$	$\nu_0 \text{ cm}^{-1}$
Phase I			
(5.0 kbar)	380.0	0.308	380.0
	495.0	0.353	493.8
	696.0	0.464	697.2
	867.0	0.428	866.2
	903.0	0.293	901.3
	922.0	0.22	921.1
	961.0	0.331	960.6
Phase II			
(80.0 kbar)	400.0	-0.0618	402.0
	461.0	0.229	454.0
	493.0	0.0075	493.4
	515.0	0.0534	513.6
	607.0	0.0564	605.2
	727.0	0.0761	723.7
	891.0	0.0029	890.9
	925.0	-0.0181	925.9
	982.5	0.156	978.4

ν_0 = intercept of regression line at 1 bar or transition pressure.

whereby the large cation polyhedra vary significantly with pressure or temperature, but the anion tetrahedra are essentially constant in volume.

As far as pyroxene variants are concerned these important structural trends have been observed almost exclusively in silicate systems. There is, however, no reason not to expect entirely similar behaviour in the pyroxene metavanadates studied here. Indeed, there are several further analogies to be drawn from the structural changes seen in silicate compounds.

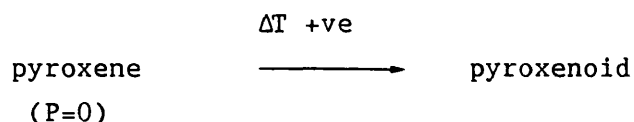
It is well known that in high pressure reconstructive transformations cations commonly increase in coordination, with a corresponding increase in cation-anion distance, and increased packing efficiency of atoms. A clear example of this is the change of many crustal mineral silicates from tetrahedral four-coordinate silicon (^{IV}Si) to octahedral six-coordinate silicon (^{VI}Si). Most of the known $^{IV}\text{Si} \rightarrow ^{VI}\text{Si}$ transitions occur when the mean Si-O bond compresses to *ca.* 1.59 Å.¹⁴ In chain silicates the transformation to orthosilicates with longer $^{IV}\text{Si-O}$ bonds or to ^{VI}Si compounds occurs at *ca.* 150 kbar. The corresponding transitions in the isostructural germanate analogues take place at lower pressures. This is generally accounted for by the larger ionic radius of Ge^{IV} (Si^{IV} 0.26/ Ge^{IV} 0.39 Å)¹⁵ and a consequent shortening of the mean Ge-O distance. Thus, less pressure is required to produce a compression of the Ge-O bond to some critical value at which the transition is effected.

Pentavalent, four-coordinate vanadium has an ionic radius of 0.355 Å, a value similar to that of Ge^{IV} .¹⁵ It is reasonable to assume, therefore, that a transition from four to six-coordinate vanadium will occur at pressures near to, or slightly in excess of those found for germanates (six-coordinate Ge^{IV} and V^V have almost identical ionic radii, 0.53, Ge / 0.54, V Å).¹⁵

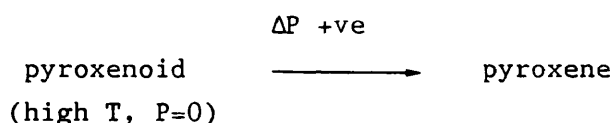
Clearly the nature of the transition observed for RbVO_3 and KVO_3 is not that of a IV \rightarrow VI-coordination increase at vanadium. Inherent in such a change would be a complete modification of the $\nu(\text{V=O})$ region of the spectrum, a feature not apparent in any spectra up to 100 kbar.

A second type of phase change frequently seen in chain

metasilicates is that of the Martensitic transition. This is basically a shear transformation in which large portions of the structure remain unchanged, but layers or slabs of structure are displaced with respect to each other. Thus, in the system $(\text{Mg, Fe, Ca, Mn})\text{SiO}_3$ there exist several structural modifications, the major differences between which relate to the size and number of M^{2+} sites and the number of tetrahedra in the chain repeat. This type of transition, however, is a result of high temperature *i.e.*



and possibly,



Moreover, since the i.r. spectrum under d.a.c. conditions is a bulk property of the system, this type of transition would result in very little observable change, and can, therefore, be excluded in this case.

In the monoclinic metavanadates two types of metal cation sites exist between the chains. Using the standard nomenclature the smaller, approximately octahedral site is labelled M1 and the larger, more irregular site M2.¹⁶ The configuration of the chain may be one of three types, *viz.* S-rotated (LiVO_3), O-rotated (the remaining $C2/c$ structures) and extended or E (all $Pbcm$ structures).^{17,18} In those compounds with E chains both metal sites are equivalent.

From studies of the structural systematics of the $C2/c$ (monoclinic) alkali metavanadates¹⁹ it has been shown that two movements of the rigid $(\text{VO})_\infty$ chains are important when expansion of the M2 site occurs in order to accommodate a larger cation; such a structural distortion can be considered as modelling the effect of pressure insofar as changes in polyhedra coordination and chain movements are concerned. These are rotations of the tetrahedra to adopt a different chain configuration, and a relative displacement in the c -direction of chains in adjacent layers.

In the system $\text{NaVO}_3\text{-KVO}_3$ the structure of the $(\text{Na}_{0.5}\text{K}_{0.5})\text{VO}_3$ member is found to have Na and K ordered into M1 and M2 sites respectively, with the latter retaining eightfold coordination.²⁰ Only in

$(\text{Na}_{0.88}\text{K}_{0.12})\text{VO}_3$ is potassium forced to adopt six-coordination, although it remains exclusively in the more distorted M2 site. Indeed it is in the former compound that the smallest chain displacement (Δ) and lowest monoclinic angle (β) are found, and is hence most similar to the orthorhombic structure in which Δ is zero and $\beta = 90^\circ$. The implications of this behaviour for the I \rightarrow II transition are that even a quite considerable monoclinic distortion of the orthorhombic parent phase will allow at least one half of potassium ions to remain eight-coordinate (strictly so), while it is not unknown for potassium to be six-coordinate if the structure so demands.

In the orthorhombic structure the anion chains are related by a simple lattice translation and are not staggered as in the monoclinic form. As indicated this displacement of the chains has been shown to be the major factor in controlling the cation coordination, so the result of such a change on the phase I orthorhombic metavanadate structure would certainly be to reduce the cation coordination number. Consistent with this is the relative insensitivity of the transition pressure to change of cation (behaviour which contrasts with that of simple salts of these cations), a fact implying that the principle energy terms are those associated with reorientation and realignment of the chains. Thus, the driving force for the transition is almost certainly a reduction of cation coordination number, brought about by chain repacking, from ten/eight in phase I to strictly eight and possibly even six in phase II.

II. A Vibrational Study Of Copper Metagermanate, CuGeO₃

5.5 Introduction

Copper metagermanate is the only ternary compound known to exist in the system Cu-Ge-O.¹ Whilst many germanates are known to be isostructural with, and often behave as high pressure models of their silicate counterparts,² this is unfortunately not the case for CuGeO₃. However, the Ge-O structural unit found in this compound is the basis for a large number of materials, not least of which include many silicates and phosphates, and thus it would seem to provide one of the simplest examples upon which to conduct a vibrational study.

To date little such work has been published; that which has is confined to two incomplete infrared studies.³⁻⁵ Presented here are the complete infrared and Raman spectra at both ambient and low temperature, Fig. 5:10, together with a formal group theoretical treatment.

5.6 Experimental

CuGeO₃ was prepared by mixing 1:1 molar proportions of Aldrich "Gold Label" (>99.99% purity) copper(II) and germanium(IV) oxides, which were then fused at 1000 °C for three hours in a platinum crucible. The product was allowed to cool to room temperature in the furnace, and appeared as a turquoise-blue powder. Subsequent examination under a microscope revealed some unreacted oxides, a further forty hours being necessary to effect a complete reaction.

Vibrational data were collected as described in section 5:2, those in the Raman using *ca.* 250 mW of 514.5 and 488.0 nm Ar⁺ radiation at the sample and a spectral slit width of 0.5 cm⁻¹.

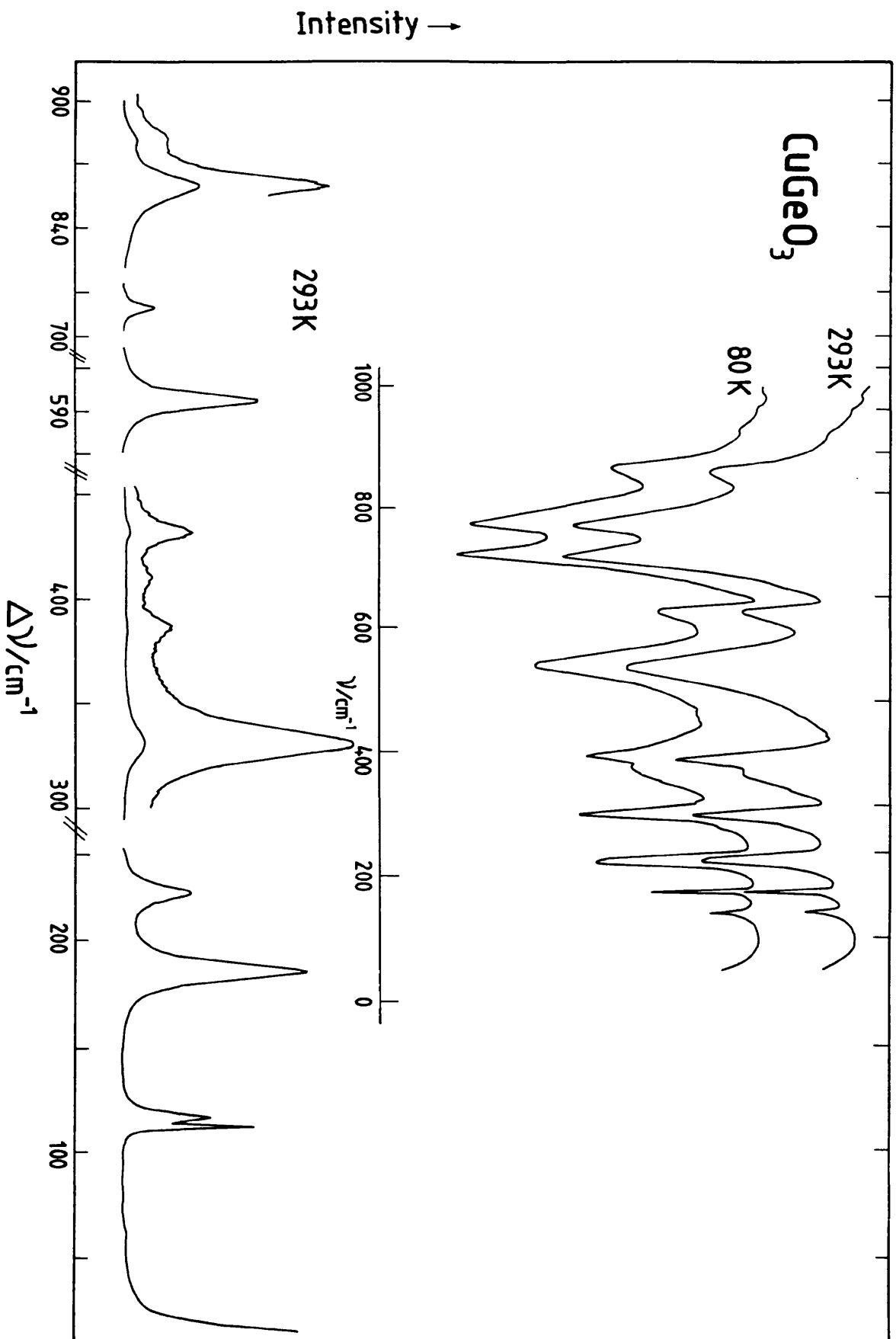
5.7 Structure and Vibrational Analysis

The ambient structure of copper metagermanate has been determined as one of orthorhombic symmetry, space group *Pmma* $\equiv D_{2h}^5$, with site

Figure 5:10

293 and 80 K mid-/far-infrared and Raman spectra of CuGeO_3 .

Raman spectra were recorded at a spectral slit width of 0.5 cm^{-1} and *ca.* 250 mW 514.5 nm Ar^+ radiation at the sample.



occupancy Cu 2d, Ge 2e, O₁ 2f, O₂ 4j in the bimolecular primitive cell.⁶ It is characterised by infinite chains of GeO₄ tetrahedra linked by common oxygen atoms extending along *b*, but is almost unique amongst oxyanions of the *meta* form in that the identity period consists of just a single GeO₃ unit, Fig. 5:11. The copper atoms are coordinated to oxygens in a tetragonally distorted octahedral environment (4O₂ at 1.94, 2O₁ at 2.77 Å), and each "octahedron" shares edges with each of two neighbouring units to form a [CuO₄]_∞ chain paralleling the [GeO₃]_∞ chain. The two are linked through oxygens located at one of the shared corners of the Cu octahedra and an unshared corner of the Ge tetrahedron. This type of copper coordination is also found in the mineral diopside,⁷ CuSiO₃.H₂O, with copper forming four short (1.96 Å) and two long bonds (2.61 and 2.75 Å) to the silicate framework. The latter, however, consists of [Si₆O₁₈]¹²⁻ rings and bears no structural similarities to the Ge-O chain.

It is apparent from this description of CuGeO₃ that the formal ionic picture, in which (GeO₃²⁻)_n chains are linked by Cu²⁺ ions (*c.f.* the metavanadates), is unlikely to accurately represent the actual structure. The covalency of the Cu^{II}-O bonds is quite high, suggesting that a more realistic model is that of an atomic lattice consisting of Ge-O-Ge and Ge-O-Cu bonds. The f.g.a. of the Cu²⁺(GeO₃)²⁻ model requires three translatory and one rotatory mode in the Raman spectrum, Table 5:9 A; the Cu²⁺ does not contribute to these and they may be expected at very low frequencies. This is not the case, as the four lowest bands of the (complete) Raman spectrum run from 112 to 225 cm⁻¹, Table 5:10. Moreover, there is a lack of i.r./Raman pairs of bands, such as is expected for the coupling of two sets of equivalent oscillators, Table 5:9 C. Accordingly, the atomic lattice model is indicated.

A detailed understanding of all the normal modes of vibration can be achieved by solving the vibrational secular equation using the method of normal coordinate analysis. This has been partially done for an isolated infinite chain of Ge-O tetrahedra, ignoring any Cu-O interactions, and the eight non-zero vibrational frequencies calculated.⁸ These values agree well for the four stretching vibrations belonging to symmetry types 2A₁, B₁ and B₂, Table 5:9 C. However, the calculated frequencies of the deformation vibrations are low, a fact largely associated with the limited applicability of the isolated-anion model in describing completely the true forms of the vibrations, plus

Figure 5:11

The crystal structure of CuGeO_3 .

Covalent radii used:

Cu (1.22)

Ge (1.17)

O (0.98)

The atoms are shown as spheres of relative sizes:

Cu (0.6)

Ge (0.2)

O (0.4)

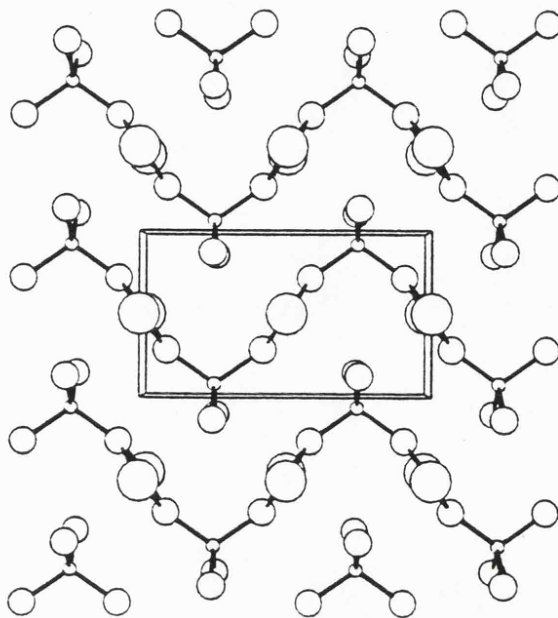
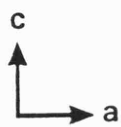
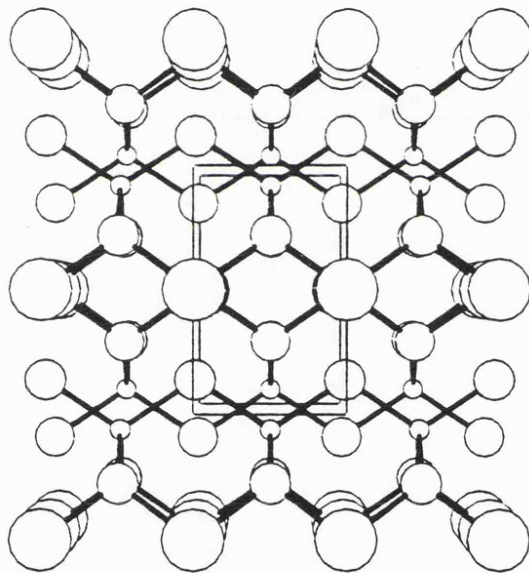
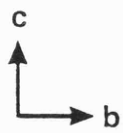
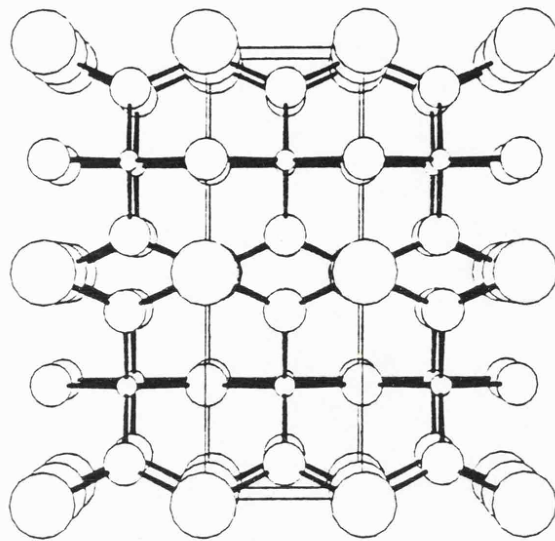
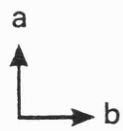


Table 5:9 A. Factor group analysis for CuGeO_3

D_{2h}	N_T^a	T_A	T	R_y	Γ_{vib}	Activity
A_g	4		1		3	Raman
B_{1g}	1				1	Raman
B_{2g}	4		1	1	2	Raman
B_{3g}	3		1		2	Raman
A_u	2		1		1	Inactive
B_{1u}	6	1	2		3	Infrared
B_{2u}	4	1	1		2	Infrared
B_{3u}	6	1	2	1	2	Infrared

B. Coupling between chains

Single chain, $C_{2v}(z)$	$\xrightarrow{x2}$	Unit cell, D_{2h}^5
$3A_1$		$3(A_g + B_{1u})$
A_2		$B_{1g} + A_u$
$2B_1$		$2(B_{2g} + B_{3u})$
$2B_2$		$2(B_{3g} + B_{2u})$

C. Mode analysis for a $(\text{GeO}_3^{2-})_n$ chain in CuGeO_3

$C_{2v}(z)$	N_T	$\nu(\text{Ge}=\text{O})_t$	$\nu(\text{Ge}-\text{O})_b$	$\text{Ge}(\text{O})_2$			
				δ	ρ	ω	τ
A_1	3	1	1^c	1			
A_2	1						1
B_1	2	1			1		
B_2	2		1^c			1	

a,b See Table 5:3

c In a hypothetical $(\text{GeO})_n$ planar chain this A_1 mode is transverse optic and the B_2 mode longitudinal optic in type.

Table 5:10 Assignment for CuGeO_3

Raman		Assignment	Infrared	
293 K	80 K		80 K	293 K
877.0	879.6	$\nu_{\text{as}}(\text{Ge-O-Ge})$	864.4	859.0
855.2	855.9	$\nu(\text{Ge=O})$	{ 772.5	770.0
708.7	711.4			722.5
590.8	591.5	$\nu_{\text{s}}(\text{Ge-O-Ge})$	624.8	625.0
			537.9	532.6
432.1	430.0			
411.1				
386.8			380.7	379.5
331.3	330.0		~364	~354
			291.5	287.5
222.1	225.6		216.0	217.3
184.8	185.9			
			168.3	166.1
			133.8	132.5
115.8	114.7			
111.0	112.3			

the lack of force constant refinement needed to obtain the best fit of calculated and observed frequencies.

The Ge-O-Ge stretching modes are constrained to be in the yz plane of the zig-zag chain, and for a single chain are in A_1 and B_2 of C_{2v} . Since the former has the nature of a transverse and the latter a longitudinal optic mode, it follows that $A_1 < B_2$ in energy. This agrees with the n.c.a.. In the two-chain unit cell these modes couple, yielding A_g/B_{1u} and B_{3g}/B_{2u} pairs, *i.e.* two infrared and two Raman bands are to be expected. In considering the stretching modes of the Ge-O-Cu bonds it is important to note that Cu^{2+} does not contribute to the g -representation. Hence, the symmetry species will be those indicated in Table 5:9 C for $\nu(\text{Ge=O})$, *viz.* A_g/B_{1u} and B_{2g}/B_{3u} pairs. Taking these two sets of predictions together, they must cover the four highest bands in both Raman and infrared spectra, Fig. 5:10. Further, the highest bands of all at 877.0 (Raman) and 859.0 cm^{-1} (i.r.) are attributed to the l.o.-like ν_2 , $\nu_{as}(\text{Ge-O-Ge})$ mode. A more detailed understanding of these and the lower frequency modes must await normal coordinate analysis of the whole unit cell.

5.8 Summary

The mid-/far-infrared and Raman spectra of a series of orthorhombic metavanadate pyroxenes MVO_3 , $M = K, Rb, Cs$, and the structurally related $CuGeO_3$ have been studied and assignments proposed on the basis of a detailed factor group analysis. In the mid-infrared high pressure data up to 100 kbar reveals transitions at 56 and 53 kbar for KVO_3 and $RbVO_3$ respectively. The nature of the transition is discussed in terms of the structural characteristics and behaviour of the silicate and monoclinic metavanadate pyroxenes.

5.9 References

5.9.1 Alkali Metavanadates

1. F. C. Hawthorne and C. Calvo, *J. Solid St. Chem.* 22, 157, (1977).

2. R. D. Shannon and C. Calvo, *Can. J. Chem.* **51**, 265, (1973).
3. K. Ramani, A. M. Shaikh, B. S. Reddy and M. A. Viswamitra, *Ferroelectrics* **9**, 49, (1975).
4. I. L. Botto, E. J. Baran and P. J. Aymonino, *Monat. Chem.* **107**, 1127, (1976).
5. S. Ondera and Y. Ikegami, *Inorg. Chem.* **18**, 466, (1979).
6. S. Ondera and Y. Ikegami, *Inorg. Chem.* **19**, 615, (1980).
7. *Inorg. Synth.* **15**, 104, (1974).
8. D. M. Adams and S. K. Sharma, *J. Phys. E* **10**, 838, (1977).
9. D. M. Adams and S. J. Payne, *J. Chem. Soc. Dalton*, 407, (1974).
10. R. M. Hazen and L. W. Finger, *Am. Mineral.* **63**, 297, (1978).
11. R. M. Hazen and L. W. Finger, *Am. Mineral.* **64**, 196, (1979).
12. L. W. Finger and R. M. Hazen, *J. Appl. Phys.* **51**, 5362, (1980).
13. R. M. Hazen and L. W. Finger, *J. Phys. Chem. Solids* **42**, 143, (1981).
14. R. M. Hazen and L. W. Finger, *Science* **201**, 1122, (1978).
15. R. D. Shannon, *Acta Cryst.* **A32**, 751, (1976).
16. C. W. Burnham, J. R. Clark, J. J. Papike and C. T. Prewitt, *Z. Krist.* **125**, 109, (1967).
17. J. B. Thompson, *Amer. Mineral.* **55**, 292, (1970).
18. J. J. Papike, C. T. Prewitt, S. Sueno and M. Cameron, *Z. Krist.* **138**, 254, (1973).
19. H. N. Ng, C. Calvo and K. L. Idler, *J. Solid St. Chem.* **27**, 357, (1979).

20. K. L. Idler, C. Calvo and H. N. Ng, *J. Solid St. Chem.* **25**, 285, (1978).

5.9.2 Copper Metagermanate

1. W. Weppner, C. Li-Chuan and A. Rabenau, *J. Solid St. Chem.* **31**, 257, (1980).
2. A. E. Ringwood and M. Seabrook, *J. Geophys. Res.* **68**, 4601, (1963).
3. A. N. Lasarev and T. F. Tenisheva, *Opt. i Spekt. SSSR* **10**, 79, (1961).
4. J. P. Labbé, *Mikrochim. Acta*, 298, (1964).
5. J. P. Labbé, *Ann. Chim.* **10**, 317, (1965).
6. H. Völlenkne, A. Wittmann and H. Nowotny, *Monat. Chem.* **98**, 1352, (1967).
7. H. G. Heide and K. Boll-Dornberger, *Acta Cryst.* **8**, 425, (1955).
8. A. N. Lasarev, "Vibrational Spectra and Structure of Silicates", Consultants Bureau, New York, 1972.

CHAPTER 6

A STUDY OF THE PHASE BEHAVIOUR OF $K[M(CN)_2]$, $M = Ag, Au$, AT HIGH
PRESSURE INVESTIGATED BY RAMAN SCATTERING

CHAPTER 6

A STUDY OF THE PHASE BEHAVIOUR OF $K[M(CN)_2]$, $M = Ag, Au$, AT HIGH PRESSURE INVESTIGATED BY RAMAN SCATTERING

6.1 Introduction

The element Au in oxidation state +1 is known to form a large number of compounds in linear coordination, of which $K[Au(CN)_2]$ is typical. All members of the Group 1B triad form a complex cyanide anion of the form $[M(CN)_2]^-$, $M = Cu, Ag, Au$, which are among the most stable and best characterised two-coordinate complexes known. However, whilst the structures of Au and Ag potassium salts are closely related in that they contain discrete linear complex ions,^{1,2} the analogous copper compound has an entirely different structure in which there exist helical polymeric chains of composition $[Cu(CN)_2]^-_\infty$.³

Of these three materials only $K[Ag(CN)_2]$ has been studied previously at pressure using vibrational spectroscopy (Raman scattering).⁴ Two high pressure polymorphs were discovered in the range below 18 kbar, the transitions occurring at *ca.* 2 and 10 kbar, however, no structural data are available for either of phases I or II. $K[Au(CN)_2]$ has been the subject of a study into the effect of pressure on the Mössbauer hyperfine interactions (isomer shift and quadrupole splitting) at 4.2 K up to 43 kbar.^{5,6} This probe into the electronic structure of the $[Au(CN)_2]^-$ complex gave an indication of the changes in the nature of the Au-ligand bond in terms of increased π bonding and orbital utilisation.

The results presented here give evidence for two new phases of $K[Au(CN)_2]$ in the pressure range up to 25 kbar, plus independent confirmation of the behaviour reported for the silver complex. In addition, $K[Ag(CN)_2]$ is shown to undergo at least two further transitions at higher, yet still moderate, pressures.

6.2 Experimental

The commercially available potassium dicyanometallates(I) were recrystallised from aqueous solution before use. Ambient and low temperature Raman and mid-/far-infrared spectra were recorded using the instrumentation detailed in Chapter 5. High pressure Raman data for $K[Au(CN)_2]$ were collected from samples loaded in a Mark III Dyno cell with standard Mo and inconel gaskets (0.2/0.15) using *ca.* 250 mW 514.5 nm Ar^+ radiation at the sample and a spectral slit width of 1.0 cm^{-1} (phase I) or 0.5 cm^{-1} (phases II and III). The reversible nature of each transition was checked using both ascending and descending pressure. Initial loadings using 4:1 MeOH/EtOH resulted in the deposition of metallic gold, when subjected to pressure and laser irradiation, due to the half-reaction $Au^{1+} + e^- \rightarrow Au^0$, Fig. 6:1. This is considered to be a result of the formation of a redox process with the gasket metal(s). Up to 25 kbar use of the sample alone was found to be satisfactory, with no discernable loss of hydrostaticity.

6.3 $K[Au(CN)_2]$ - Structure and Vibrational Analysis

The ambient form of $K[Au(CN)_2]$ crystallises in the rhombohedral space group $R\bar{3} \equiv C_{3i}^2$ (No. 148), with $a = 9.74 \text{ \AA}$, $\alpha = 43.9^\circ$ and a trimolecular primitive cell ($[Au(CN)_2]^-$ on $3d$, K^+ on $1a$ and $2c$).¹ The structure is similar to that of $K[Ag(CN)_2]$ and consists of layers of potassium ions alternating with layers of linear $[Au(CN)_2]^-$ complex ions, each pair of layers being shifted one third the length of the long diagonal of the cell base, Fig. 6:2. The bonding within layers is weak and all complex ions are orientated at an angle of *ca.* 20° to the c axis.

Previous vibrational studies of solid $K[Au(CN)_2]$ have been concerned primarily with the internal mode assignments of fundamental and overtone/combination bands of the $[Au(CN)_2]^-$ ion under $D_{\infty h}$ symmetry.⁷ However, according to the crystal structure these complex ions do not adopt strict linear centrosymmetric geometry, the angle Au-C-N being reported as $172.8 \pm 7.5^\circ$. The quite considerable margin of error in this value can be attributed to the large temperature factors of C and N, nevertheless, any detailed interpretation of the vibrational spectra requires such a deviation from linearity to be taken into

Figure 6:1

Photomicrograph showing deposition of metallic gold on the diamond surface, after being subjected to both pressure and laser irradiation.

Figure 6:2

Crystal structure of $\text{K}[\text{Au}(\text{CN})_2]$.

Covalent radii used:

K (1.33)

Au (1.5)

C (0.68)

N (0.68)

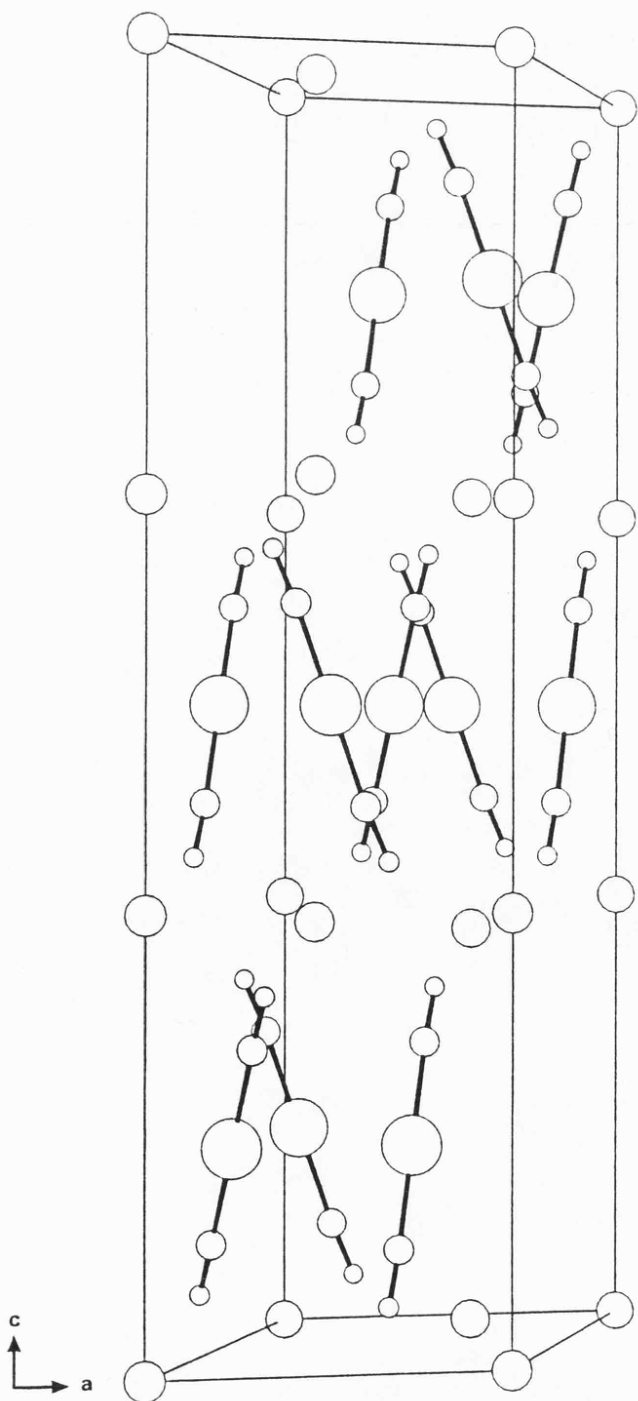
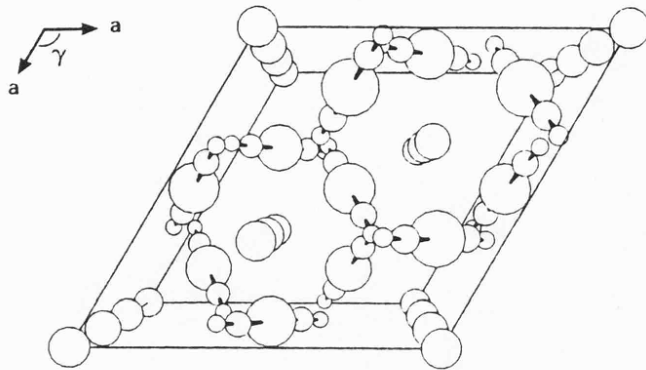
The atoms are shown as spheres of relative sizes:

K (0.4)

Au (0.6)

C (0.3)

N (0.2)



consideration. To this purpose Table 6:1 shows the changes in the f.g.a. and correlation schemes on adopting a bent C_{2h} molecular point group. Thus, it is now important to consider rotations of the complex ion about the molecular axis. This manifests itself in the B_g component of the A_g/B_g pair obtained on lifting the degeneracy of the $D_{\infty h}$ Π_g species, *i.e.* the out-of-plane component of the Π_g $\delta(\text{Au-CN})$ vibration under $D_{\infty h}$ has become a rotatory mode (R_x or R_y) under C_{2h} . As a result the external mode representation for the unit cell gains a Raman-active A_g/E_g pair at the expense of that of the internal vibrations. It is clear that this approach accounts well for the ambient Raman spectrum, whilst the previous assignments in the infrared remain unaffected.

On this basis Table 6:2 shows an assignment for the present data. The Raman-active internal modes ν_1 , ν_2 and ν_5 all appear above 300 cm^{-1} as A_g/E_g pairs, the apparently anomalous third component of $\nu_5(\text{C-N})$ seen at 80K (2167.5 cm^{-1}) being attributed to a combination band; ν_1 + external mode in type, Fig. 6:3. Since the separation of these two features is but 1.8 cm^{-1} , the lattice mode must be acoustic translatory in origin. ν_2 , $\nu_5(\text{Au-C})$ appears as an extremely weak and broad pair of bands at *ca.* 450 cm^{-1} . The low intensity of this mode is entirely analogous to that in $\text{K}[\text{Ag}(\text{CN})_2]$. Conversely, the factor group components of ν_5 are a fairly strong and closely spaced doublet (314.5 and 309.0 cm^{-1}), which further separate at 80K (317.6 and 312.1 cm^{-1}).

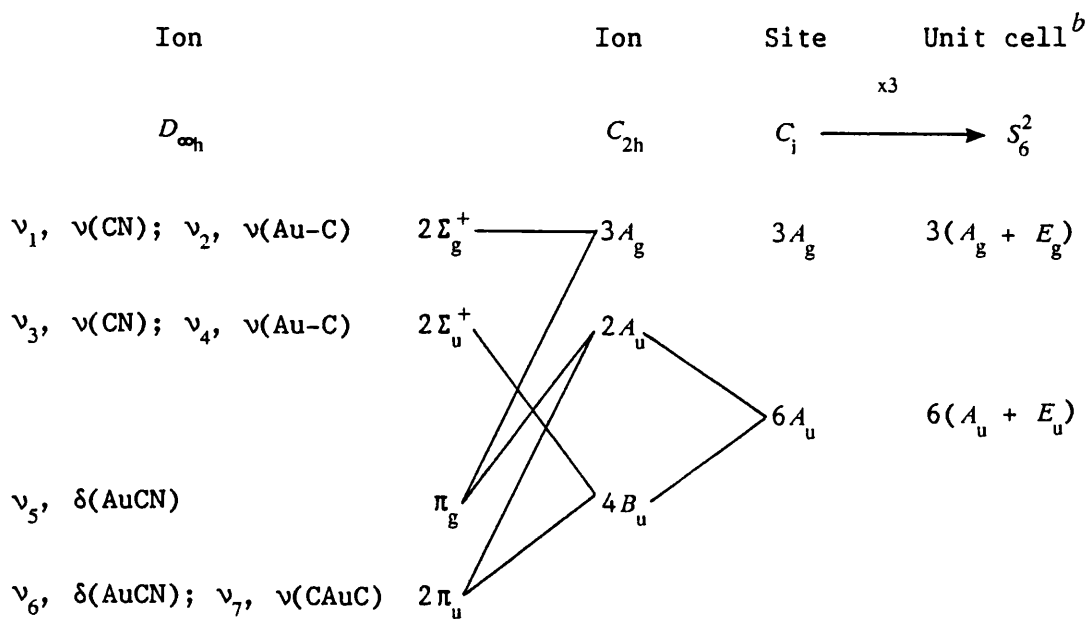
All features below 160 cm^{-1} are those of translations and librations. Their exact nature it is not possible to ascertain without single crystal data, however, the pair at *ca.* 30 cm^{-1} , some 20 cm^{-1} below the next external mode feature, are likely to be those due to R_z , since the very nature of this mode, a virtually unhindered rotation about the molecular axis, requires it to be at very low frequency.

The infrared spectrum of $\text{K}[\text{Au}(\text{CN})_2]$ is notable for its dearth of features below 200 cm^{-1} ; only three bands are observed, Fig. 6:3. ν_3 and ν_4 should both appear as A_u/E_u doublets, and whilst the former shows some sign of splitting at low temperature the latter remains unresolved. Of the remaining internal fundamentals, ν_6 and ν_7 both derive from a doubly degenerate π_u species under $D_{\infty h}$, hence each generates two A_u/E_u pairs on coupling in the unit cell. Previous reports have failed to observe ν_6 (this work is no exception), which appears to be vanishingly weak, but on the basis of a combination frequency have assigned to it a

Table 6:1 A. Factor group analysis for $K[Au(CN)_2]$

S_6^2	N_T^a	T_A	T	R	Γ_{vib}	Activity
A_g	7		1	3	3	Raman
E_g	7		1	3	3	Raman
A_u	11	1	4		6	I.r.
E_u	11	1	4		6	I.r.

B. Correlation scheme.



a

- N_T = total number of modes.
- T_A = acoustic translatory,
- T = optic translatory,
- R = libratory,
- Γ_{vib} = internal vibrational modes.

b

This column sums to Γ_{vib} in A.

Figure 6:3

293 and 80 K Raman capillary, and
80 K mid-/far-infrared spectra of
 $\text{K}[\text{Au}(\text{CN})_2]$.

Raman spectra were obtained using
ca. 300 mW of 514.5 nm Ar^+
radiation at the sample with a
spectral slit width of 0.5 cm^{-1} .

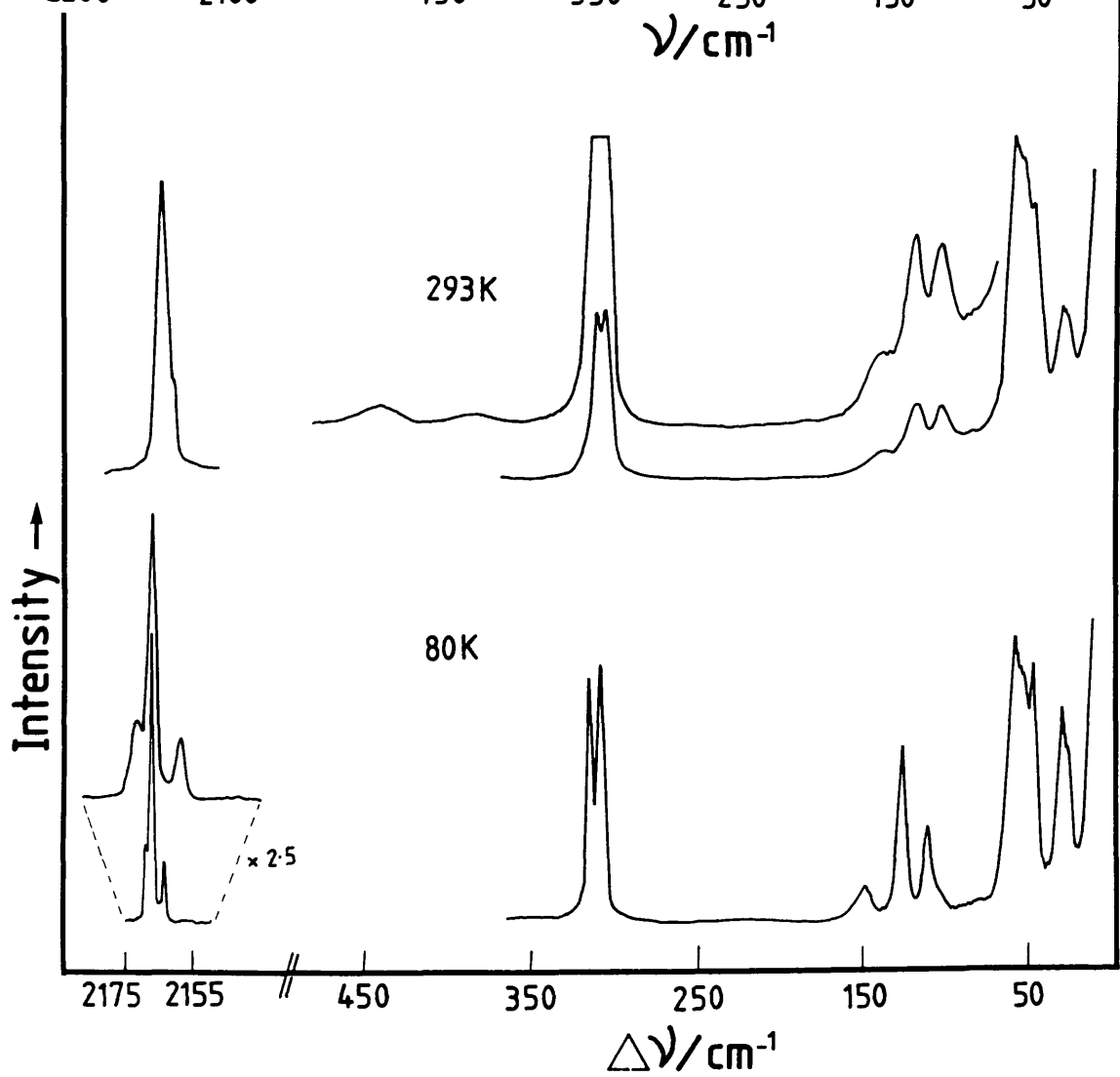
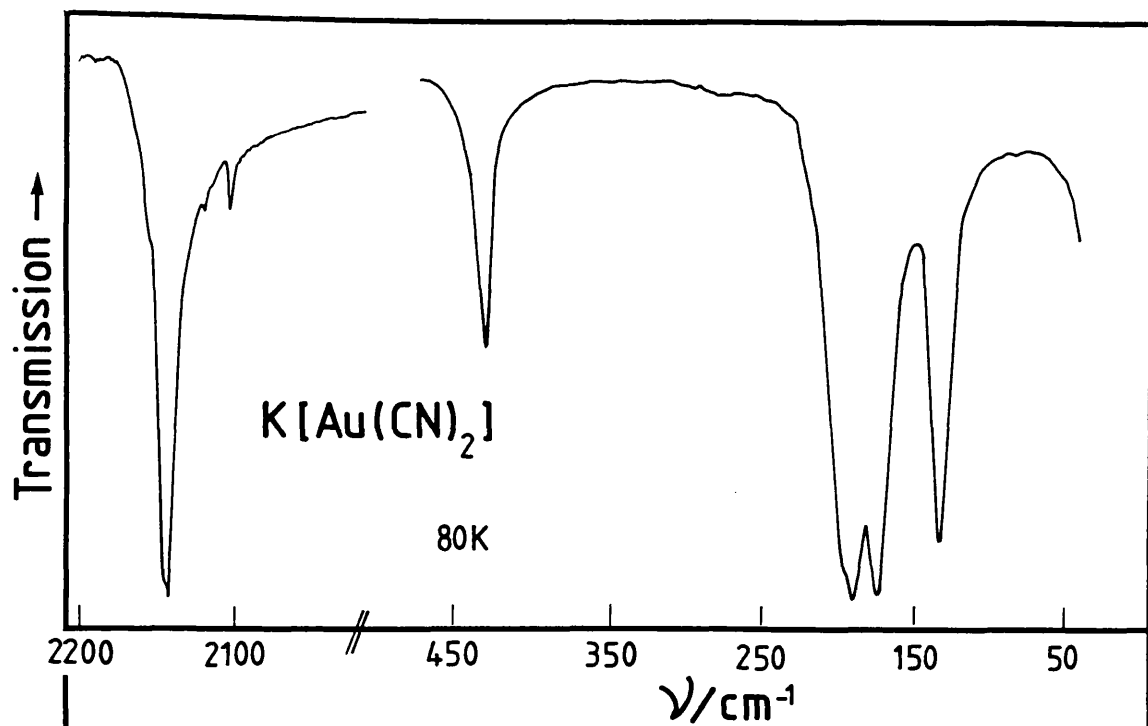


Table 6:2 Assignment for $K[Au(CN)_2]$

Raman		Assignment	Infrared	
293 K	80 K		80 K	293 K
	2167.5	$\nu_1 + T_A$		
2162.2	2165.8	ν_1		
~2159.0	2162.2			
		ν_3	2142.7	2139.6
		isotopic	{ 2119.5	2116.0
		species		{ 2103.6
		ν_4	429.3	425.3
~450.0		ν_2		
		ν_6		~368.0 ^a
314.5	317.6	ν_5		
309.0	312.1			
		ν_7	{ 191.0	
			{ 175.0	
~141.0	149.0	\updownarrow ν_L	ν_T 133.1	
119.8	126.5		<i>b</i>	
104.0	110.1			
58.6	58.4			
~53.0	~53.0			
47.4	47.8			
28.8	29.5			
~25.0	~26.0		R_z	

^a Deduced from a combination frequency.⁷

^b The seven remaining ir-active translations are all vanishingly weak.

value of $ca. 368 \pm 10 \text{ cm}^{-1}$.⁷ ν_7 , $\delta(\text{CAuC})$, is attributed to the strong band pair at 175 and 191 cm^{-1} (80K); further complexity is to be expected at still lower temperatures. An earlier report of 125 cm^{-1} for this mode seems somewhat too low a value,⁸ especially since the corresponding vibration in $\text{K}[\text{Ag}(\text{CN})_2]$ is at 142 (R) and 147 (ir.) cm^{-1} ,⁹ and there is a clear tendency for lower frequency modes in the Ag salt to be 30 cm^{-1} or more to lower values than the Au equivalent.

The remaining, lowest frequency feature at 133 cm^{-1} is of translatory origin, and is the only infrared-active external vibration detected, despite the factor group requirement of eight such modes. The missing translations should be expected at values that are not coincident with those in the Raman, since the centre of symmetry indicates mutual exclusion. One interesting point is that similar lattice modes in $\text{Tl}[\text{Au}(\text{CN})_2]$ ¹⁰ and $\text{K}[\text{Ag}(\text{CN})_2]$ are generally weak and in the latter case only half the required total are observed. This absence is not readily explained; it remains to assume that they are only accidentally of such low intensity.

6.4 High Pressure Results

6.4.1 $\text{K}[\text{Au}(\text{CN})_2]$ (I)

In the ambient phase spectra of $\text{K}[\text{Au}(\text{CN})_2]$ it is unfortunate that only features due to ν_1 , ν_5 and three external modes can be followed up to the I/II transition. Of the remaining bands, ν_2 is too weak and the entire lattice spectrum below 100 cm^{-1} appears as two broad unresolved multiplets which further deteriorate with pressure. All observed modes harden within phase I, particularly those between 100 and 150 cm^{-1} , Figs. 6:6, 6:7, Table 6:3.

6.4.2 $\text{K}[\text{Au}(\text{CN})_2]$ (II)

At a pressure of $ca. 6.6$ kbar marked changes in the Raman spectrum, especially apparent, at least initially, in the lattice mode region, indicate the transition to phase II, Fig. 6:5. Below 55 cm^{-1} several intense bands spring from the previous area of weak and broad scatter,

Figure 6:4

Raman spectra of the internal and external modes of $\text{K[Au(CN)}_2\text{]}$ at ambient temperature and various pressures.

Spectra were obtained using *ca.* 250 mW 514.5 nm Ar^+ radiation at the sample and a spectral slit width of 1.0 cm^{-1} (phase I) or 0.5 cm^{-1} (phases II and III).

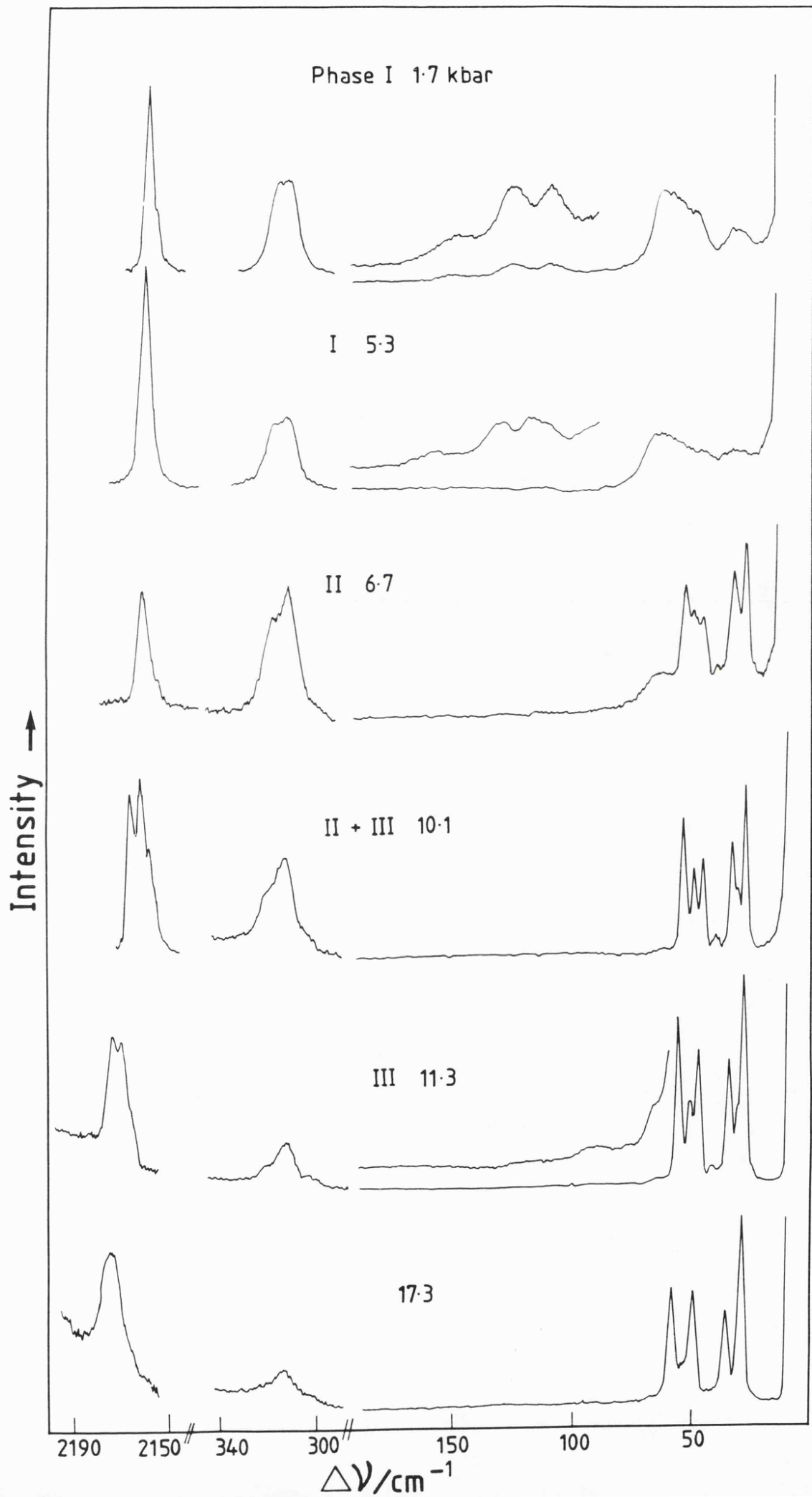


Figure 6:5

Plot of frequency ($\Delta\nu/\text{cm}^{-1}$) against pressure for the Raman-active modes of $\text{K}[\text{Au}(\text{CN})_2]$ in phases II and III below 65 cm^{-1} .

Solid lines were obtained by the method of least squares. Errors were estimated from the instrumental resolution and accuracy of measurement.

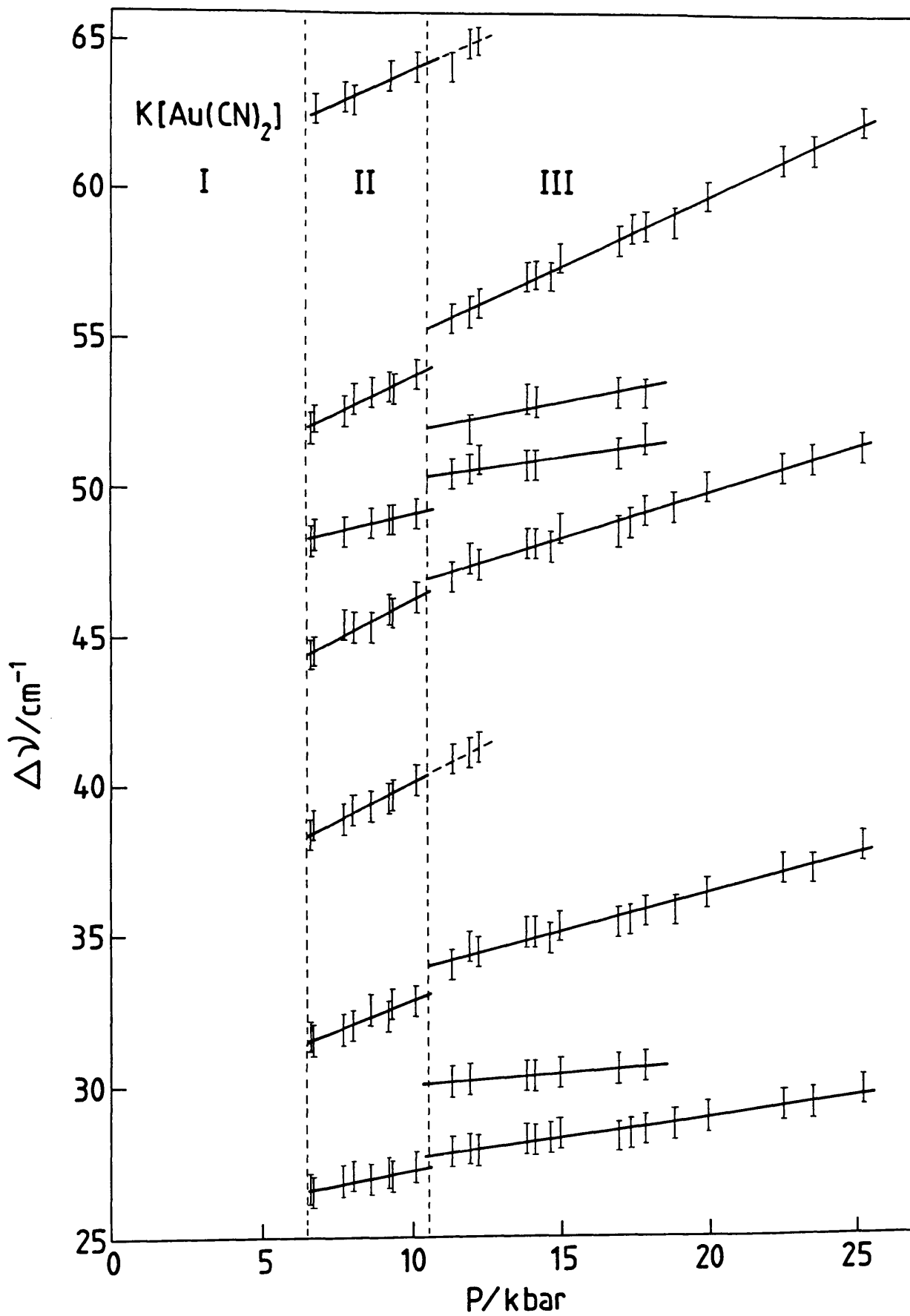


Figure 6:6

Plot of frequency ($\Delta\nu/\text{cm}^{-1}$) against pressure for the Raman-active modes of $\text{K}[\text{Au}(\text{CN})_2]$ between 100 and 160 cm^{-1} .

Solid lines were obtained by the method of least squares.

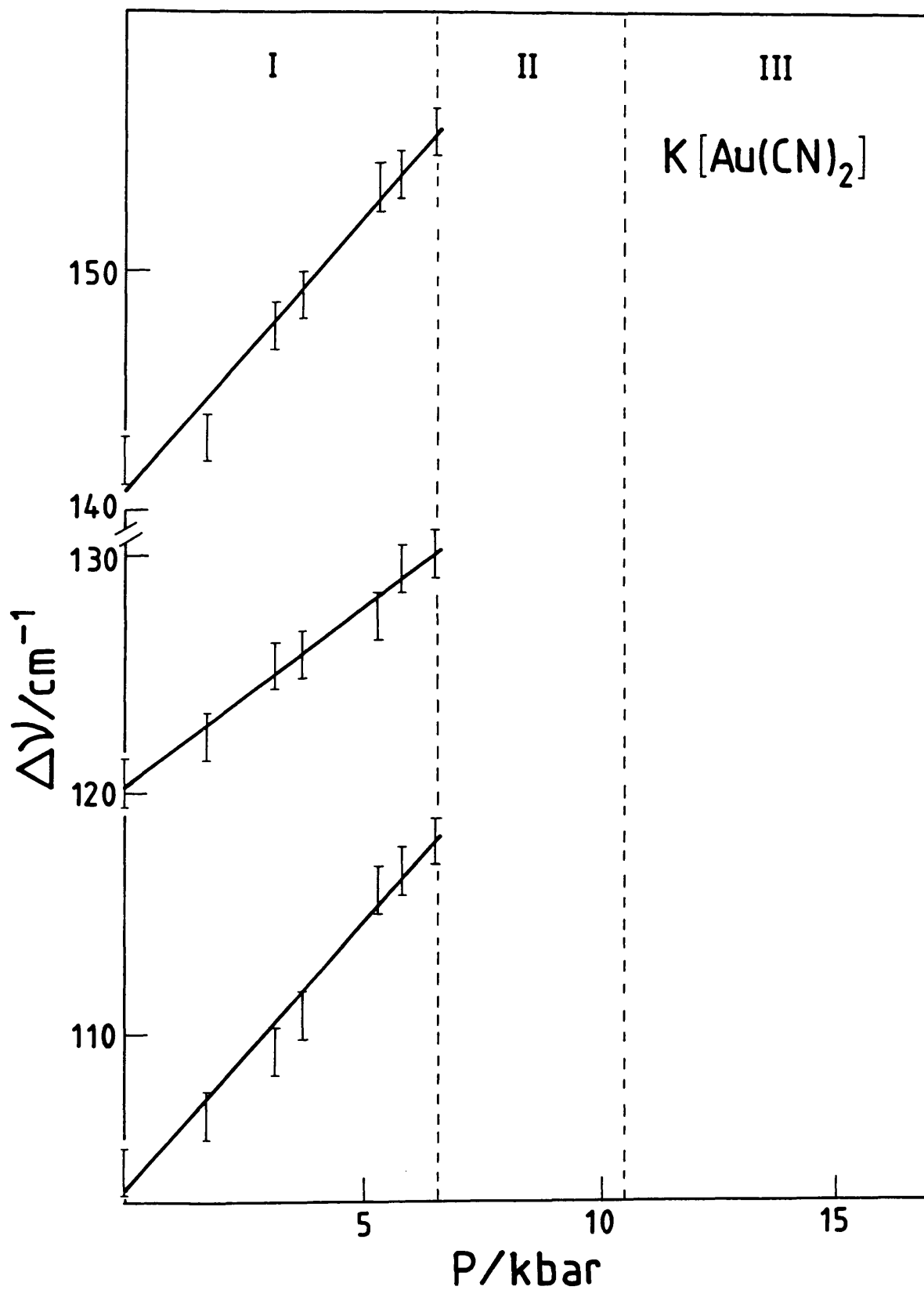


Figure 6:7

Plot of frequency ($\Delta\nu/\text{cm}^{-1}$) against pressure for the Raman-active modes of $\text{K}[\text{Au}(\text{CN})_2]$ above 300 cm^{-1} .

Solid lines were obtained by the method of least squares.

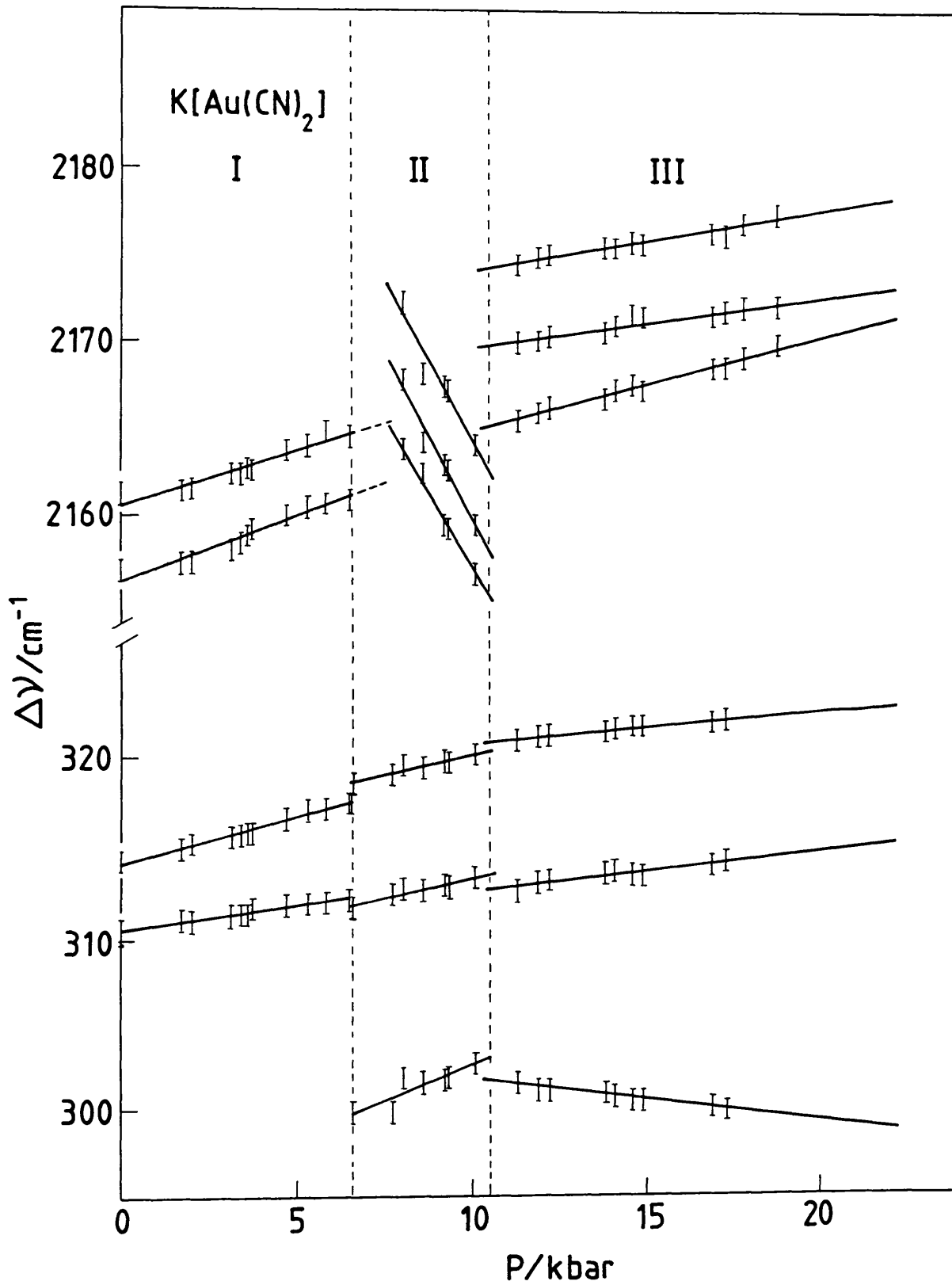


Table 6:3 Raman shifts and their pressure dependencies for $K[Au(CN)_2]$

	$\Delta\nu \text{ cm}^{-1}$	$\frac{d\Delta\nu}{dP} \text{ cm}^{-1} \text{ kbar}^{-1}$	$\Delta\nu_0 \text{ cm}^{-1}$
Phase I			
(1.7 kbar)	106.6	2.26	103.4
	122.4	1.5	120.3
	143.0	2.29	140.7
	310.8	0.27	310.2
	314.8	0.533	313.9
	2157.2	0.745	2156.2
	2161.4	0.619	2160.6
Phase II			
(8.0 kbar)	27.0	0.184	26.6
	32.0	0.39	31.5
	39.2	0.504	38.4
	45.3	0.505	44.5
	48.6	0.238	48.3
	52.9	0.475	52.1
	63.0	0.439	62.6
	301.8	0.817	299.7
	312.5	0.435	311.6
	319.6	0.462	318.6
	2163.4	-3.43	2168.6
	2167.8	-3.85	2172.7
	2172.3	-3.7	2176.8
Phase III			
(16.9 kbar)	28.3	0.135	27.7
	30.5	0.0675	30.1
	35.4	0.255	34.0
	48.5	0.299	47.0
	51.1	0.139	50.4
	53.1	0.187	52.0
	58.2	0.464	55.3
	300.1	-0.233	301.5
	313.8	0.224	312.5
	322.0	0.183	321.0
	2168.4	0.533	2165.1
	2171.4	0.284	2169.8
	2176.2	0.329	2174.3

$\Delta\nu_0$ = intercept at 1 bar (phase I) or transition pressure; 6.6 kbar (phase II), 10.5 kbar (phase III).

however, those phase I external mode features above 100 cm^{-1} have no observable counterparts in phase II.

Throughout the four kbar stability range of $\text{K}[\text{Au}(\text{CN})_2](\text{II})$ all modes, other than ν_1 , shift to higher frequencies. The components of this latter feature are remarkable in their rapid and almost parallel softening, at some $3.5\text{--}3.9\text{ cm}^{-1}\text{ kbar}^{-1}$. The highest member of the phase II triplet is seen initially at a value almost 8 cm^{-1} above that of the higher component in phase I, Fig. 6:7.

6.4.3 $\text{K}[\text{Au}(\text{CN})_2](\text{III})$

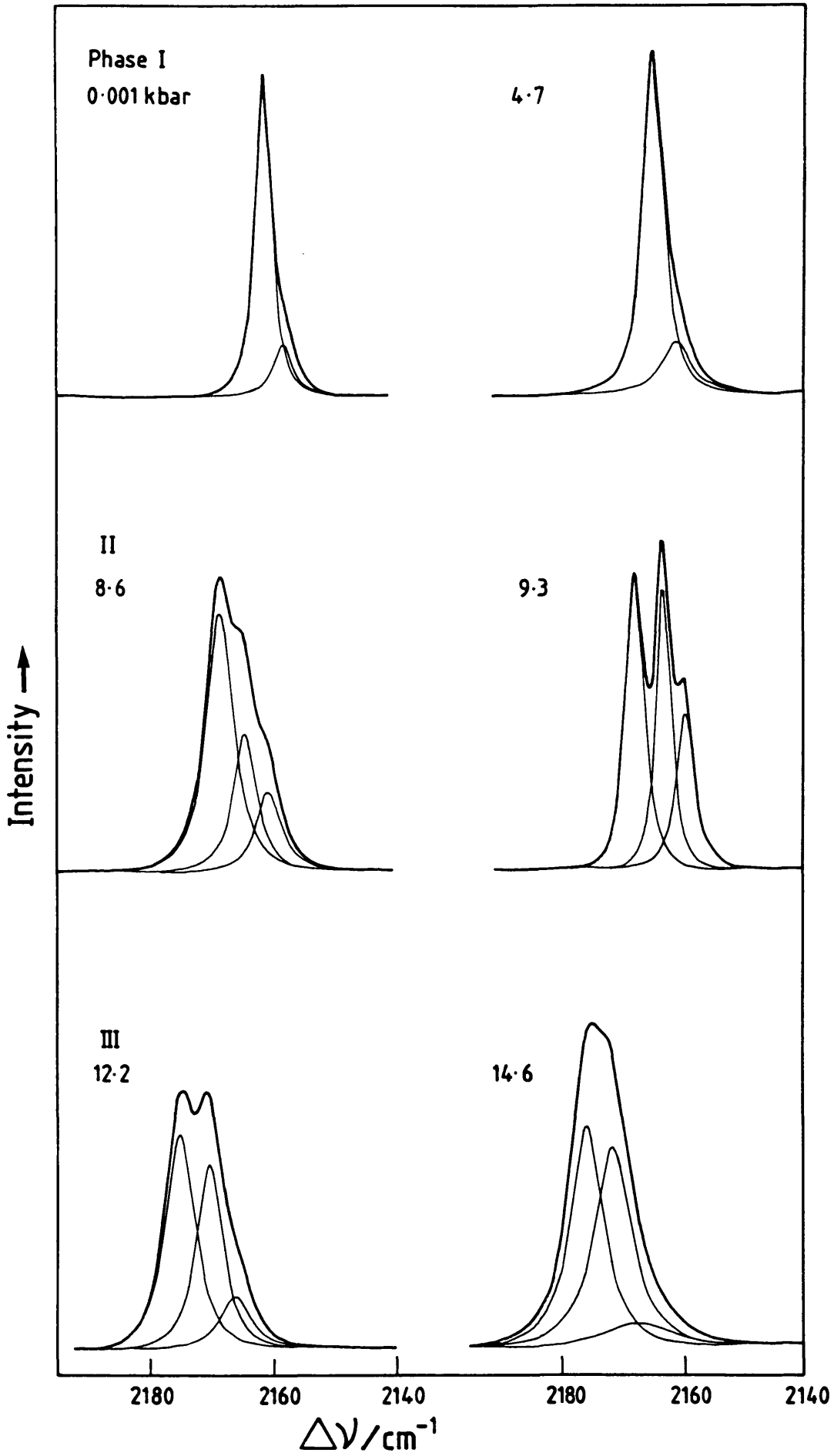
A more subtle change in the Raman spectrum occurs at *ca.* 10.5 kbar, although the transition is readily indicated by the mode plots in the cyanide stretching region. The components of this mode again jump nearly 7 cm^{-1} in frequency to values only slightly higher than at the I \rightarrow II transformation. They are, however, seen to harden with pressure. Both ν_1 and ν_5 remain as triplets, whilst below 65 cm^{-1} two bands seem to be simultaneously lost and gained, which with differential shifting gives the appearance of a pair of doublets by 17 kbar, Fig. 6:4.

6.4.4 Structural and Electronic Changes

The I \rightarrow II transition is almost certainly first order in nature. Optical observations in an ungasketted cell, in which the sample is subject to a considerable pressure gradient, reveal a strong Becke line between phases I and II. This is consistent with a not insignificant volume change, since as the daughter phase is the denser the refractive index will necessarily increase. This being so, little can be said about the new space group other than that it must allow for the lifting of the E_g degeneracy. Such is discerned most clearly in the behaviour of ν_1 , Fig. 6:8, and ν_3 , which present as triplets. An increase in multiplicity of this kind could equally be caused by a cell content increase, however, a cell doubling can be ruled out in this case since either four or six bands would be generated for each fundamental, assuming the retention of individual, linear complex ions. Moreover, any accidental degeneracy would be indicated by a greater intensity of one or more components; none is observed. The increased complexity in the lattice

Figure 6:8

Deconvoluted Raman spectra showing the development of ν_1 , $\nu(\text{C-N})_s$, in each of the three phases of $\text{K}[\text{Au}(\text{CN})_2]$.



spectrum also follows from this argument, although it is clear that the four new bands expected (one for each original A_g/E_g pair) are not all accounted for in present spectra.

The more subtle change accompanying the transition to phase III is, on the other hand, indicative of a second order type. No Becke line marks the phase boundary, although an increased red shift in the absorption maxima does give some indication of the presence of $K[Au(CN)_2](III)$. Despite the apparently contradictory evidence of the mode plots, it is considered that no new features exist in the spectra of this phase. The resolution of the weak bands at *ca.* 29 and 52 cm^{-1} is merely an effect of the increased separation between the more intense band pairs seen to lower and higher frequency (27/34 and 47/56 cm^{-1}) in each case.

A general outline of the possible structural changes occurring at each transformation is as follows:

(i) The ambient phase has a fairly open structure. Better utilisation of space is achieved by the tilting (*ca.* 20°) of complex ions within layers relative to *c*, this in turn allows for octahedral KN_6 coordination (6 K-N at 2.79 Å). At the phase change there is certainly a compression and repacking of these layers to a situation in which the complex ions lie more nearly or strictly in the *ab* plane.

(ii) The second order nature of the II → III change suggests that atom displacements should be less dramatic than in (i), with perhaps a slight reorientation within layers to give eight-fold coordination at K.

It is known, from ^{197}Au Mössbauer studies of Au(I) compounds, that at ambient pressure delocalisation of the 5*d* electrons to the ligands may be considered negligible.^{5,6} Further, population distributions show that no back donation occurs via the 5*d* orbitals of π symmetry. Since the π orbitals exhibit considerably less overlap at atmospheric pressure than the σ orbitals, they are expected to be more pressure sensitive. This is actually the case, as the effect of pressure is to strongly increase π bonding by delocalisation of 5*d* electrons into the empty antibonding π^* orbitals on the CN^- ligands. π backbonding of this kind decreases the metal orbital energy but increases the ligand π^* level, resulting in greater net separation.¹¹ The transition involved in this metal-to-ligand charge transfer process thus shows a red shift with pressure. A result of this shift, in what is commonly a low energy

transition, is that the sample may become absorbing in the visible, as is the case with $K[Au(CN)_2]$.

The initial absorption of light carries the system into the higher vibrational energy levels of an electronically excited state. Radiative deactivation of this excited species may occur by the process of fluorescence, which by its very nature occurs at lower energy. Since the laser irradiation used in Raman spectroscopy is an ideal source for inducing fluorescence (a case in point is that of the R_1 and R_2 lines of ruby used to monitor pressure), and that compared with Raman scattering it is of much greater intensity, the presence of fluorescence features can entirely swamp those due to first order scattering. This occurs significantly in the $K[Au(CN)_2]$ system at pressures above *ca.* 20 kbar and, therefore, precludes further Raman study.

6.5 $K[Ag(CN)_2]$ - Preliminary High Pressure Results

The crystal structure of $K[Ag(CN)_2]$ is very similar to that of the Au analogue in that it consists of alternating layers of potassium and complex ions.² Each pair of layers is shifted one half the length of the long diagonal of the cell base, a sequence which results in an hexagonal cell with space group symmetry $P\bar{3}1c \equiv D_{3d}^2$, No. 163. Potassium is six coordinate to nitrogen in a distorted octahedral environment and the almost linear $[Ag(CN)_2]^-$ ions are orientated at an angle of *ca.* 27° to the *c* axis.

Raman and infrared data for this compound are essentially complete,^{9,12,13} although no single crystal work has been published. The high pressure Raman data indicate two transitions up to 18 kbar, at *ca.* 2 and 10 kbar.

The most intense feature in the Raman spectrum is ν_1 , the symmetric cyanide stretch. Preliminary results in which the behaviour of this mode has been followed to 25 kbar show two further transitions to phases IV and V at *ca.* 15 and 21 kbar respectively. All these phases can be distinguished using microscopic observation in an ungasketted cell. The pressure dependencies in phases I, II and III closely follow the trends reported previously.

Since the ambient structures of these two complex cyanides are very similar, it is quite probable that the high pressure structural sequences observed here will give rise to one or more isotypic phases. The large number of transformations observed for these compounds at relatively low pressures, particularly in the case of the silver salt, is indicative of the initial open packing in this structure type. Since $K[Ag(CN)_2](I)$ is considerably less dense (2.36 g cm^{-3}) than $K[Au(CN)_2](I)$ (3.45 g cm^{-3}) it may well adopt the latter's rhombohedral structure at some stage; the spectra of phase III most closely resemble the required format.

6.6 Summary

The high pressure polymorphism of $K[Au(CN)_2]$ has been studied by Raman scattering at ambient temperature up to 25 kbar, revealing two phase transitions at 6.6 and 10.5 kbar. Little structural information can be gleaned for either of the new phases, since the $I \rightarrow II$ transformation is clearly first order in type. The reported increase in $Au \pi - CN \pi^*$ interaction is shown in a qualitative manner to manifest itself as a red shift in the absorption and fluorescence maxima. Preliminary work on the structurally similar $K[Ag(CN)_2]$ indicates four transitions below 25 kbar at *ca.* 1.5, 8.9, 15.0 and 21.0 kbar, confirming the mode behaviour reported earlier for phases I and II.

6.7 References

1. A. Rosenzweig and D. T. Cromer, *Acta Cryst.* **12**, 709, (1959).
2. J. L. Hoard, *Z. Krist.* **84**, 231, (1933).
3. D. T. Cromer, *J. Phys. Chem.* **61**, 1388, (1957).
4. P. T. T. Wong, *J. Chem Phys.* **70**, 456, (1979).
5. D. Günzburger and D. E. Ellis, *Phys. Rev. B* **22**, 4203, (1980).
6. H. Prosser, G. Wortmann, K. Syassen and W. B. Holzapfel, *Z. Phys. B* **24**, 7, (1976).

7. L. H. Jones, *J. Chem. Phys.* **27**, 468, (1957).
8. B. M. Chadwick and S. G. Frankiss, unpublished work.
9. T. M. Löhr and T. V. Long, *J. Chem. Phys.* **53**, 4182, (1970).
10. H. Stammreich, B. M. Chadwick and S. G. Frankiss, *J. Mol. Struct.* **1**, 191, (1968).
11. H. G. Drickamer and C. W. Frank, "Electronic Transitions and the High Pressure Chemistry and Physics of Solids", Chapman Hall, London, 1973.
12. L. H. Jones, *J. Chem. Phys.* **26**, 1578, (1957).
13. G. L. Bottger, *Spectrochim. Acta* **24**, 1821, (1968).